Final Report, Part I

Experimental Measurement of the Flow field of Heavy Trucks

DE-AC26-98EE50512

Fuel Saving by Means of Flaps Attached to the Base of a Trailer: Field Test Results

Fred Browand, Charles Radovich
Aerospace and Mechanical Engineering Department
University of Southern California
Los Angeles, CA 90089-1191
and **Mathieu Boivin**
Norcan Aluminum Inc
Terrebonne, Canada J6Y 1N9

SUMMARY

Flat flaps that enclose the trailer base on the sides and top are known to reduce truck drag and reduce fuel consumption. Such flapped-truck geometries have been studied in laboratory wind tunnels and in field tests. A recent review of wind tunnel data for a variety of truck geometries and flow Reynolds numbers show roughly similar values of peak drag reduction, but differ in the determination of the optimum flap angle. Optimum angles lie in the range 12 degrees—20 degrees, and may be sensitive to Reynolds number and truck geometry. The present field test is undertaken to provide additional estimates of the magnitude of the savings to be expected on a typical truck for five flap angles 10, 13, 16, 19, and 22 degrees.

The flaps are constructed from a fiberglass-epoxy-matrix material and are one-quarter of the base width in length (about 61 cm, or 2 feet). They are attached along the rear door hinge lines on either side of the trailer, so that no gap appears at the joint between the flap and the side of the trailer. The flap angle is adjusted by means of two aluminum supports.

The present test is performed on the NASA Crows Landing Flight Facility at the northern end of the San Joaquin valley in California. The main runway is approximately 2400 meters in length, and is aligned approximately in a north-south direction. The test procedure is to make a series of runs starting at either end of the runway. All runs are initiated under computer control to accelerate the truck to a target speed of 60 mph (96.6 km/hr), to proceed at the target speed for a fixed distance, and to decelerate at the far end of the runway. During a run, the broadcast fuel rate, the engine rpm, forward speed, elapsed time—as well as several other parameters (10 in all)—are digitized at a rate of 100 digitizations per second. Various flapped-conditions are interspersed with the "no flaps" control, and are sequenced in a different order on different days. Approximately 310 runs are accumulated over the 5-day test period, May 17-21, 2004.

The runway slopes rather uniformly upward from north-to-south. Over the distance of 2424 meters between our two "start" markers at either end of the runway, the net change in elevation is a little over ten meters. Test results clearly show the greater fuel consumption required to lift the truck against gravity in the southbound direction. For this reason, it is important that the tests be averaged over a round trip circuit—that is, a run in *both* directions over the identical portion of the roadway.

Northbound-southbound averages require an overlap segment of the runway (near the middle of the runway) where the truck—starting from either end—has achieved its target speed. For the target truck speed of 60 mph, this overlap region is approximately 700 meters in length. Typically a run and the return run are accomplished within a time interval of 6 minutes.

Analysis of the data show fuel consumption savings at all flap angle settings tested, when compared to the "no flaps" condition. The most beneficial flap angle appears to be 13 degrees, for which the fuel consumption is 0.3778 ±0.0025 liters/km compared to the "no flaps" control of 0.3941 ± 0.0034 liters/km. The error bounds expressed above mark the 99% confidence interval in the mean values given. That is, additional estimates of the mean fuel consumption would be expected to lie within the bounds given, approximately 99% of the time. The fuel consumption saving is—to reasonable accuracy—about 1.63 liters/100 kilometers. These savings represent the increment associated only with the change in drag due to the presence or absence of flaps. The result will hold for any truck of similar size and shape and engine performance regardless of the loading of the truck or the rolling resistance.

The economy achieved by use of base flaps can be compared to the economy resulting from driving two trucks in a tandem configuration. In December 2003, such fuel consumption tests were performed at the same Crows Landing test-site. In the tests, two identical trucks are operated at headways in the range 3–10 meters. The trucks are steered by hand, but longitudinal control is provided by a closed-loop control system. Laser ranging measures truck-to-truck distance, and the control system maintains a truck separation to within about ±3 centimeters.

From these tests it is concluded that both trucks save fuel by close-following, that the fuel saving increases with decreasing spacing, and that the trail truck saves more fuel. An average value of fuel saving for each of the two trucks at spacings of 6-10 meters can be taken to be 3.0 liters/100 km.

Fuel Saving by Means of Flaps Attached to the Base of a Trailer: Field Test Results

1. OBJECTIVES

1.1 TESTING ADD-ONS FOR DRAG REDUCTION

Wind tunnel tests of truck models dating back at least twenty years show decreased drag when plates are attached to the base of the truck (trailer), and are either angled with respect to the stream or inset from the sides of the trailer. The plates are installed along the trailer sides and top—and sometimes along the bottom. The plates are often referred to as rear-deflectors, boat-tail plates or angled boat-tail plates. Several examples are shown in figure 1—(a) shows inset boat-tail plates, and (b) shows angled plates, or simply flaps as we will call them. Obviously a combination of the two is possible. The plates can also be curved rather than flat. In all these cases, the flow is turned by the presence of the flaps (plates), and it is not hard to imagine that the wake behind the truck becomes smaller, resulting in less drag. But turning the flow inward along the edges increases the speed and decreases the pressure locally. Since a drag decrease must be associated with an increase in the averaged pressure over the base, the flaps must act to shield the major portion of the base from the lower pressures along the edges. (See for example, Lanser et al. 1991, who measured base pressures for the inset boat-tail plates of figure 1(a). Pressures measured outside the inset are lower, but pressures inside are greater, than equivalent pressures measured in the absence of the plates.)

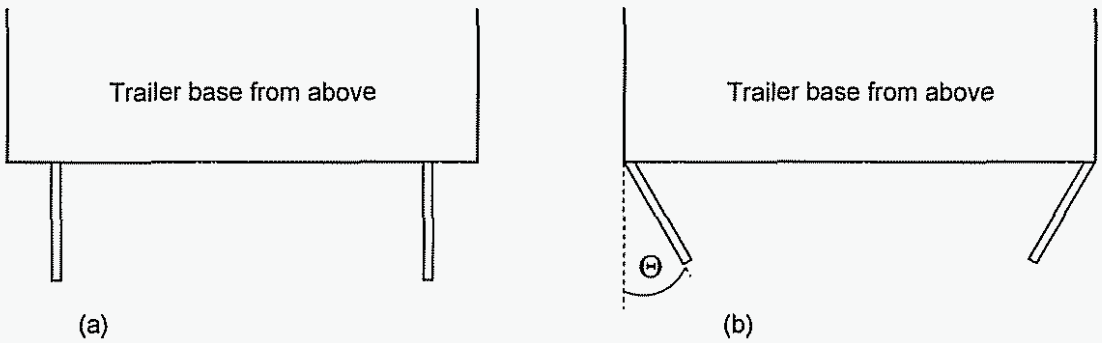

Figure 1. Several examples of rear-deflectors seen from a top view: (a) boat-tail plates, top and bottom plates not shown; (b) angled plates, or flaps, top and bottom flaps not shown.

More recent wind tunnel studies on a one-eighth-scale model at full-scale Reynolds numbers in the NASA Ames 12-foot pressure tunnel have demonstrated that the flaps in figure 1(b)—including flaps along the roof line and along the bottom—result in greater drag savings that do the corresponding boat-tail plates of figure 1(a), at all angles of yaw (see Storms et al. 2004). This has also been verified in wind tunnel studies at lower Reynolds numbers by Visser & Koon 2004.

In an earlier experiment—at one-tenth-scale, one-third full-scale Reynolds number—Cooper has shown that flat flaps perform slightly better than curved flaps, and that there is no benefit in having flaps longer than about 25% of the truck width (Cooper 1985, Cooper 2003). Cooper also demonstrates that there is an optimum flap angle beyond which the drag savings begins to diminish. He determines the optimum flap angle to be about 15 degrees.

A recent review of wind tunnel data from several sources for a variety of truck geometries and flow Reynolds numbers show roughly similar values of peak drag reduction, but differ in the determination of the optimum flap angle (Hsu et al. 2004). Optimum angles lie in the range 12 degrees—20

degrees, and may be sensitive to Reynolds number and truck geometry. The present field test is undertaken to provide additional estimates of the magnitude of the savings to be expected on a typical truck for five flap angles 10, 13, 16, 19, and 22 degrees.

In our case, the flaps are flat plates set flush with the sides and top of the trailer, and are inclined away from the stream direction by the flap angle, Θ, as in figure 1(b).

1.2 UTILIZING THE BROADCAST FUEL RATE

The instantaneous volume fuel rate available on the J1939 data bus is a convenient means for measuring fuel consumption. The instantaneous fuel rate is updated ten times per second at a resolution of ±0.05 liters/hr. For a truck traveling at 100 km/hr (62.1 mph), this resolution corresponds to a digitizing accuracy of ±0.05 liters/100km.

Use of the fuel rate signal is not presently a standard procedure in fuel consumption tests, although we believe it to be accurate and reliable under the proper circumstances. This is particularly true if it is the difference in fuel consumption from some control configuration that is desired rather than the absolute value. While the absolute fuel consumption rate may be accurate within several per cent, the *difference* in fuel consumption over a day, or several days occupied by the testing, can be expected to be much more accurate. The present procedure is reminiscent of the method championed in the 1970's and 1980's by Buckley and others (see, for example, Buckley 1985, and Saunders et al. 1985). These early tests required the installation in the cab of fuel-metering equipment that was read and recorded by hand. The great advantage today is that the fuel rate record—and other desired engine parameters—are easily acquired and stored in a laptop for later processing.

Because of our interest in promoting the method, both the test site and the test procedure are described in some detail in Sections 2 through 6. Results are described in Section 7, and if it is only the "bottom line" financial reward available from reduced drag that is of interest, turn immediately to Section 7.3.

2. THE SITE AT CROWS LANDING

The present tests are performed at the NASA Crows Landing Flight Facility at the northern end of the San Joaquin valley. The main runway is approximately 2400 meters in length, and is oriented roughly north-south, as shown in figure 2(a). The elevation of the runway—determined from our recent survey—is shown in exaggerated vertical scale in figure 2(b).

As can be seen, there is an elevation change along the runway. The runway slopes rather uniformly upward from north-to-south. Over the distance of 2424 meters between our two "start" markers at either end of the runway, the net change in elevation is a little over ten meters. Because the runway is relatively flat, the elevation gain is difficult to see visually. However the test results clearly show the greater fuel consumption required to lift the truck against gravity in the southbound direction. For this reason, it is important that the tests be averaged over a round trip circuit—that is, a run in *both* directions over the identical portion of the runway.

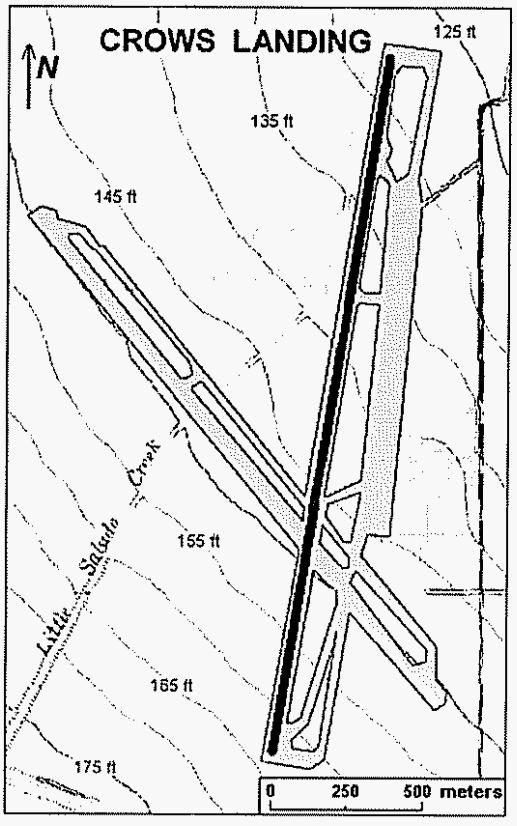

Figure 2(a). Plan view of the NASA Crows Landing Flight Facility. Red bar marks measurement interval on runway.

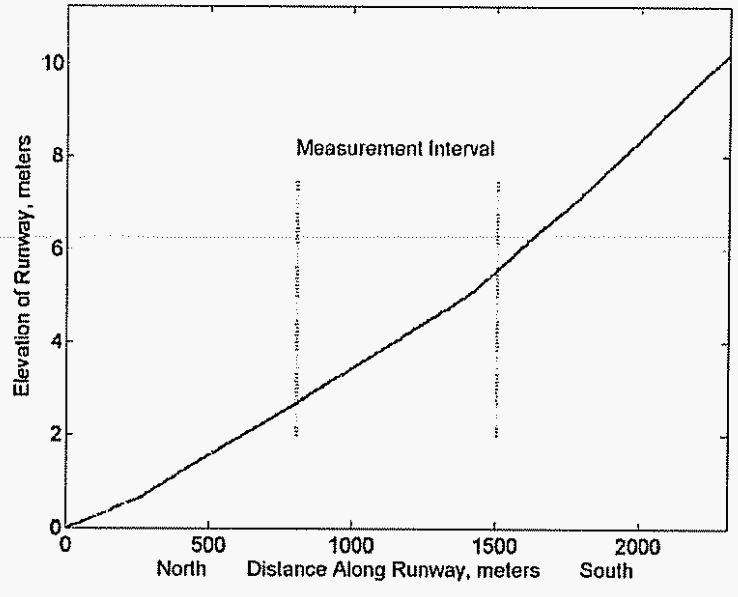

Figure 2(b). Runway elevation from North to South. Marked central section indicates the region of data acquisition.

The condition of the concrete runway surface is generally good. This surface is clean, and substantially free from cracks and potholes although there are—as with any concrete surface—slight elevation mismatches at the concrete block joints. Figure 3 is a photograph looking southward from the mid-point along the runway. The truck runs in the second lane to the right of the solid white line.

Figure 3. View of Crows Landing looking southbound from mid-point on runway.

3. TRUCK AND TRAILER

A single Freightliner 2001 Century Class truck is used for the tests. The truck is powered by Cummins N14 Celect engine developing a maximum of 350 HP. The truck has an automatic transmission, Allison HD 4060 (six forward gears), and a rear axle ratio of 4.63. In operation, the truck executes multiple runs up and down the runway. A run consists of an acceleration phase to a predetermined speed, a uniform speed phase, and a deceleration phase. First, an achievable speed trajectory is established for the truck on the runway. This desired speed trajectory is then programmed into an on-board computer that controls the truck, and insures that all runs are executed in identical fashion.

The additional computer control makes use of the standard outputs available on the J1939 bus, and can be illustrated by reference to figure 4. In normal operation, the driver initiates motion by depressing the (electronic) throttle. The engine control module (ECM) interprets the throttle command as a driver demand for speed or torque, depending upon the engine load.

Under enhanced computer control, the vehicle dynamics are modeled separately (items below the J1939 bus in figure 4), and the torque required to achieve the programmed speed trajectory is generated. This desired torque is put onto the J1939 bus at location TSC1. The signal at TSC1 overrides the signal coming from the throttle, and the engine attempts to establish the desired torque.

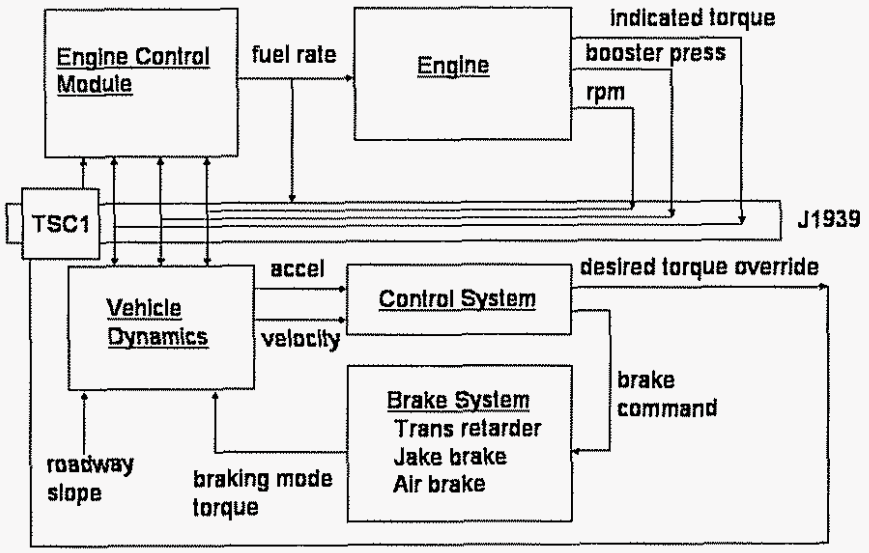

Figure 4. Schematic circuitry for automated driving.

The trailer is a relatively new Wabash trailer supplied by Norcan Aluminum, Incorporated. The movable fifth wheel of the tractor is placed so the gap between cab and trailer is as small as possible without physical contact during normal driving. At the center-plane, the distance from the rear of the cab to the front of the trailer is 0.99 meters (39 inches). The distance from the downstream end of the cab extender to the front plane of the trailer is 0.48 meters (19 inches). A side view of the tractor-trailer gap is shown in figure 5. Note that there is a mismatch in height between tractor and trailer.

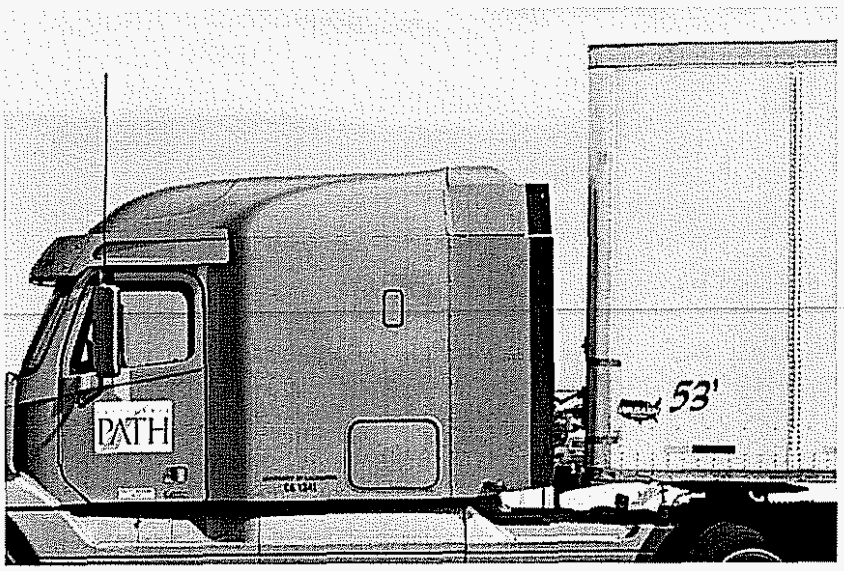

Figure 5. Position of trailer during tests.

Rolling resistance is sensitive to tire inflation pressure. As a rule-of-thumb, a 10% increase (decrease) in tire pressure can decrease (increase) the rolling resistance by about 1%. For these tests, tractor and trailer tire inflation is checked each morning to lie within 110-115 psig. Tread depth is approximately 8 mm on the trailer and 6-8 mm on the tractor.

The tests are conducted with a driver and one passenger. No auxiliary equipment is operated during the time data is recorded. The early morning testing does not require the use of air-conditioning in the cab. At the commencement of each run the air compressor and the engine fan are disabled on the J1939 bus by the computer program. Compressor and fan are allowed to operate during the turning periods at each end of the runway. No excessive engine temperatures were noted.

One can distinguish between the absolute accuracy of a measurement, and the *relative* accuracy between several measurements recorded over a short time interval under largely similar conditions. The inaccuracy of the broadcast fuel rate signal is judged by Cummins to be within ±3%. A major source of this inaccuracy is a result of higher than expected fuel temperature that can arise when fuel re-circulated from the injectors heats the fuel remaining in the tank. Unwanted fuel tank heating can be minimized by maintaining nearly full tanks. Fuel use during the week of testing varied between 22 and 28 gallons per day, and fuel tanks were topped each day after testing. Under these identical daily conditions, the *relative* day-to-day (or run-to-run) inaccuracy of the broadcast fuel rate signal can be expected to be considerably smaller, as the data analysis will show.

Tractor and trailer are weighed at standard weighing stations. There is one within twenty miles of Crows Landing. The weights are included here for reference purposes, and because weight is needed to make drag savings predictions from the fuel consumption data (see section 7.2). The tractor is weighed fully fueled, no driver. Weights are as follows:

Tractor: 83,614 N (18,790 pounds) Trailer: 64,436 N (14,480 pounds)

The uncertainty in these weights is probably about one percent.

4. THE BASE FLAPS

Base flaps are attached to the sides and top of the rear of the trailer. The flaps are constructed from a fiberglass-epoxy-resin material and are one-quarter of the base width in length (about 61 cm, or 2 feet). Figure 6 presents several of the flaps used for the test. The side-flaps swing on piano hinges that are bolted directly to the rear side-edges of the trailer to produce a sealed joint. This installation detail is dictated by the need to quickly remove the flaps for the "no-flaps" control runs.

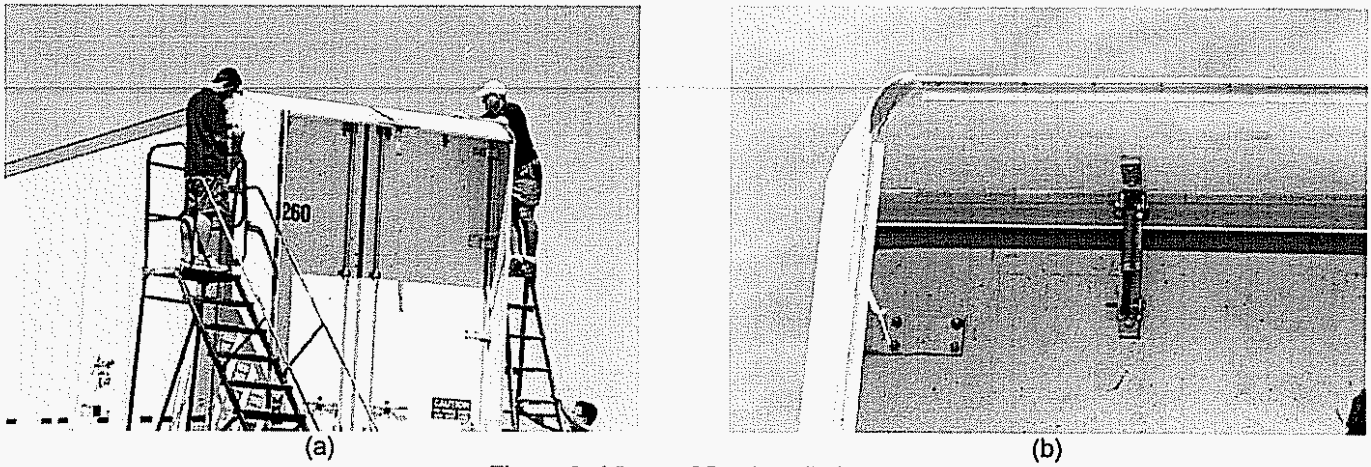

(a) (b)

Figure 6. Views of flap installation.

The flap angle is adjusted by means of two aluminum supports. Holes are pre-drilled to allow the five flap angles to be set quickly. In commercial application, the flaps are attached along the rear door hinge lines, so that no gap appears at the joint between the flap and the side of the trailer. Also in commercial application, the flaps are constrained only by a short length of cable attached to the rear door. Higher pressures on the trailer base and on the inside of the flap, compared to the stream side of the flap, are sufficient to keep the flap extended at highway speeds.

The flap at the top of the rear door is split so the doors can be opened. The two flap-halves are mounted by means of hinges and are kept in place by means of adjustable turnbuckles, figure 6(b). The split in the top flap is sealed with duct tape, as are the corners (figure 6a).

The "no-flaps" control is obtained by completely removing flaps from the sides, and taping the top flaps against the rear door, as in figure 7(b).

(a) (b)

Figure 7. (a) Flaps extended in working position; (b) the "no-flaps" control.

5. LOCAL WEATHER CONDITIONS

5.1 WEATHER TYPICAL OF NEARBY PATTERSON

Daily weather conditions are recorded at a number of sites in the San Joaquin valley by the State of California and the University of California at Davis Agricultural Program (see) http://www.ipm.ucdavis.edu/calludt.cgi/WXDESCRIPTION?MAP=stanislaus.html&STN=PATTERSON.A
Such a weather station exists at a turf farm a few miles south of Patterson and north of Crows Landing. The minimum and maximum temperatures and the daily averaged wind speed are shown in figure 8 for the calendar year 2003 at this site. Temperatures are measured 1.5 meters above the ground, and daily averaged wind speed is determined at a height of two meters above the ground. The information is neither sufficiently detailed nor close enough to the Crows Landing runway to give useful information for our specific tests, but it does give a larger view of weather conditions over the entire year. This yearly record is quite typical of the period 2001-2004.

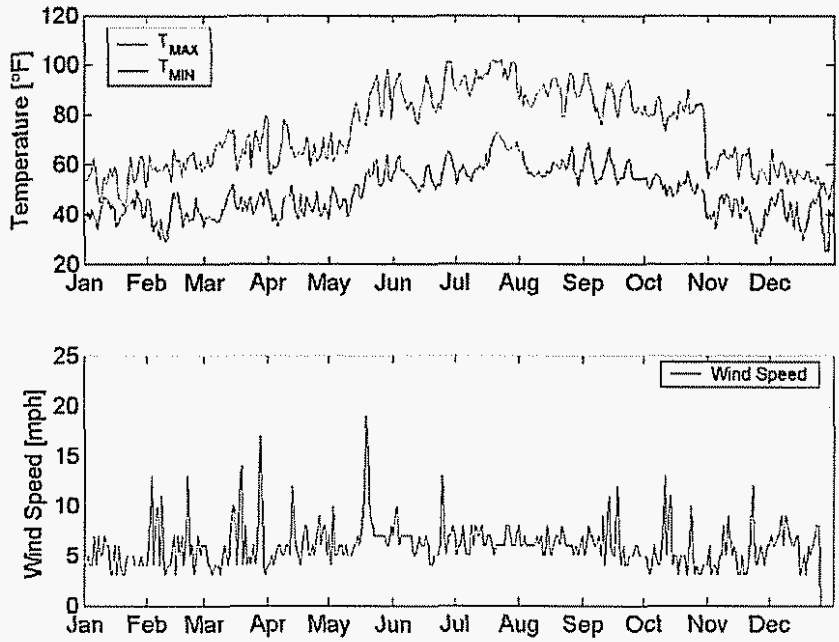

Figure 8. Temperature and wind speed near Patterson for the calendar year 2003.

Typically there is a 20°F spread in daily temperature, but temperature difference can grow to 30°F during the summer. Winds are generally light, with brief periods of heavier winds. The months from March through September have longer periods of light winds. There is also a considerable diurnal variation in wind speed, which is not shown by these daily averages.

5.2 WIND AND TEMPERATURE AT CROWS LANDING

During the tests, temperature, humidity, wind speed and direction, and barometric pressure are continuously recorded at the central position along the runway. The anemometer and the temperature and humidity units are solar powered—the barometer is battery and solar powered. The anemometer and wind vane are placed on a staff 3 meters above the runway surface, and approximately 30 meters to the side of the truck line of travel. All instruments telemeter data to a central battery powered control unit (Oregon Scientific, model WMR 968). The data is digitized into a laptop computer by means of software provided by Ambient (http://www.WeatherConnect.com). Our weather information is updated every minute.

Testing on the five days, May 17-21, typically commences at about 6:00AM and ends about 10:30AM. During this time, the temperature rises by about 20°F, from an early morning low in the high 40's. On all five days, the average temperature is very close to standard conditions, T = 288 K (59°F). Pressure variations during the week are small—and lay within 758 ±2.5 mm mercury, or 29.81±0.1 inches; standard pressure is 762 mm or 29.96 inches.

The vector wind speeds during the time of testing are shown in figure 9. Wind speed is resolved into a component in the direction of the runway (tangential), and a component at right angles to the runway (normal). The data is organized into 19 data sets—each set corresponds to a contiguous series of runs (eight runs in both directions along the track) at a specific flap angle. A set takes about 40 minutes to complete (as will be explained more completely in the next section). Wind speeds shown in figure 9 are averaged over each 40-minute testing time. Mean values are plotted as the vector arrows. The root-mean-square fluctuation values for each component during this period are plotted as the ellipses surrounding each wind vector. All wind speed values in figure 9 are expressed

as a fraction of the truck forward speed, U_T = 26.8 m/s (60 mph). Wind speed is taken positive when blowing in a northerly direction (that is, blowing *from* the south).

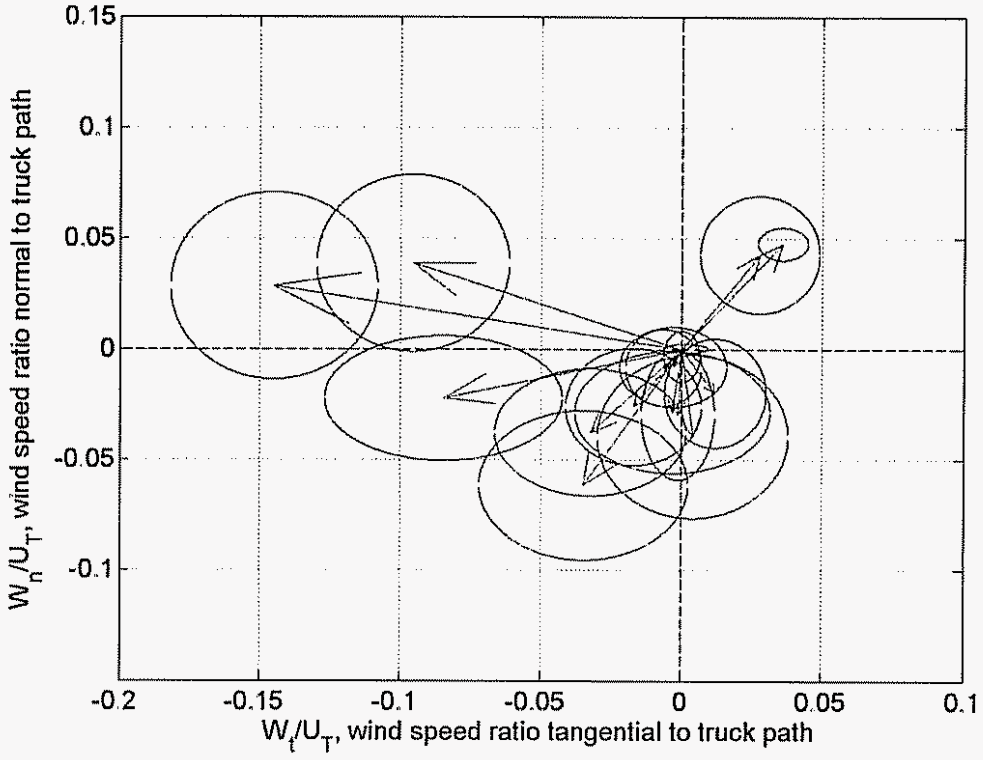

Figure 9. Wind ellipses measured at center of runway during testing, May 17-21.

Wind speeds, expressed as a fraction of the truck forward speed, are usually small. The exceptions are the three data sets having large, negative tangential wind components.

6. TEST PROTOCOL & DATA ACQUISITION

6.1 THE RUN SEQUENCE

A typical run sequence starts at a fixed point at one end of the runway. Computer control is initiated, data acquisition begins, and the truck accelerates. When the programmed acceleration ramp terminates, the truck continues along the runway at the preset cruise speed of 26.8 meters/second (60.0 mph). Distance along the track is determined by integration of the forward speed. At a pre-determined distance, the braking sequence is initiated, and the truck slows to a stop at the far end of the runway. Data acquisition stops, and the run file is logged in the computer. The truck is turned, and made ready for the return from a second fixed point on the track. Typically a run and the return run are accomplished within about 6 minutes. A total of 16 runs, or 8 run-pairs are accumulated for each flap angle setting (about 45 minutes of test time), and constitute one data set. When a data set is completed the truck is returned to the garage area, and a new flap angle is positioned. Setting a new flap angle usually takes 20-30 minutes. Four flap angles—corresponding to four data sets—are accumulated each day during the 6:00-10:30 AM period when wind and temperature are most favorable. The total data base over five testing days, May 17-21, consists of 304 runs (152 run-

pairs)—or 19 data sets—at the flap angles 10, 13, 16, 19 and 22 degrees, as well as the no-flaps condition that serves as the control.

A total of ten variables are recorded for each data set. The variables include time, integrated distance, engine torque, engine rpm, vehicle speed and instantaneous fuel consumption (broadcast fuel rate). All of these signals are commonly available on the J1939 bus.

6.2 DIGITIZED SIGNALS & SMOOTHING

Examples of typical raw data signals for a pair of runs on May 17, 2004, are shown in figure 10. The three plots are engine speed, forward speed and fuel rate, respectively, as a function of distance along the runway. Red is the southbound run (run 18) and blue is the northbound run (run 17), corresponding to a flap angle setting of 13 degrees. In the top plot, the gear changes can be seen, as well as the region of uniform engine speed attained in the central section of the runway. The northbound run begins at the south end of the runway (blue), and the gear changes reflect this starting position.

The overlap region where a constant speed is attained can clearly be seen in the central section of the runway—extending between about 750 and 1650 meters. The actual window used for data averaging is from 862 to 1562 meters. Within this window, the broadcast fuel rate is reasonably constant, but not free from fluctuation, as illustrated in the lowest of the three plots.

Three more plots are shown at increased magnification for this central portion of the runway. Figure 11 is vehicle speed, figure 12 is fuel rate, and figure 13 is the fuel rate divided by vehicle speed, giving fuel consumption directly in liters/kilometer.

The solid curve in figure 11 is a smoothing, cubic-spline. One can see the termination of the accelerated portion of each run, and the constant speed portion of the run. The average speed in the constant speed portion is pre-determined within the computer algorithm, and becomes 26.81 ±0.01 m/s—held within this tolerance throughout the week.

In figure 12, the effect of truck acceleration on fuel rate can be seen to diminish and to disappear in the overlap (constant speed) region—862 to 1562 meters. However, the higher frequency *fluctuations* in fuel rate are still present, and contribute to the run-to-run *variability* of the estimated fuel consumption.

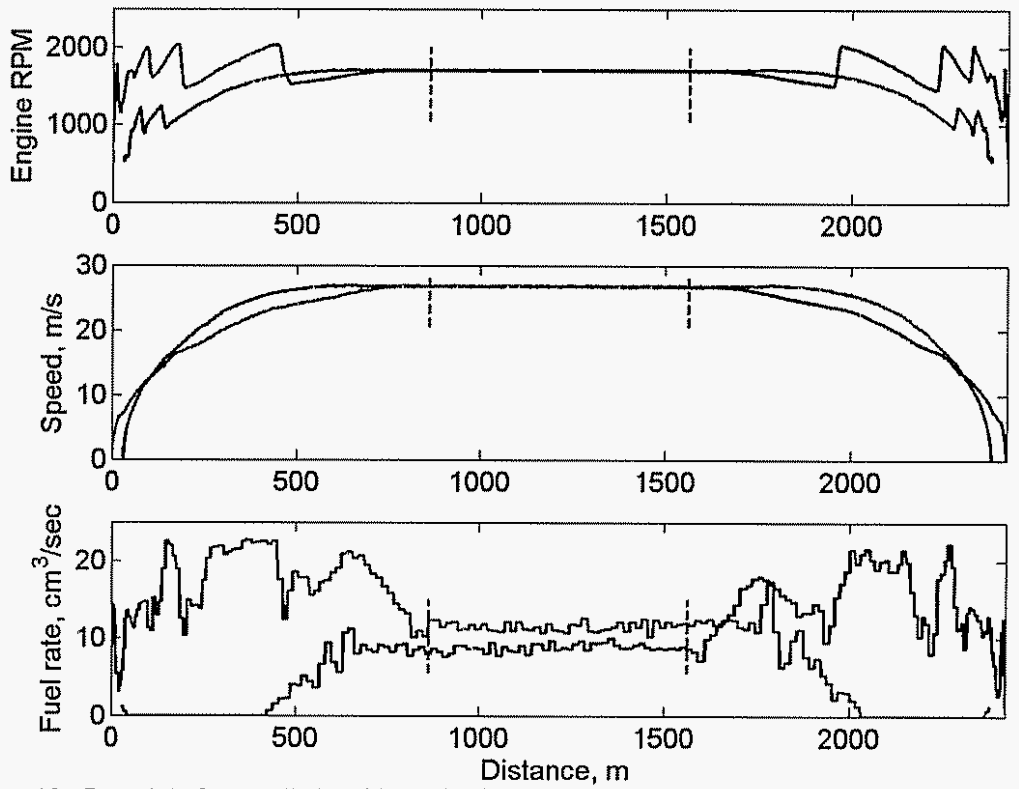

Figure 10 Raw data for run 17 (northbound in blue) and run 18 (southbound in red), May 17, 2004. Dotted vertical bars show averaging interval on runway. Flap angle = 13 degrees.

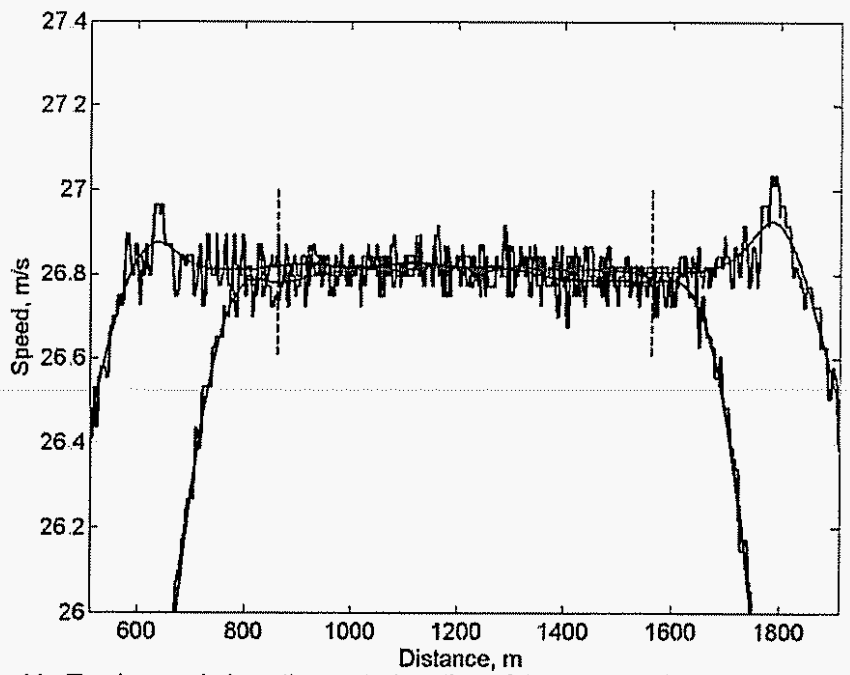

Figure 11. Truck speed along the central portion of the runway, the raw signal, and the cubic-spline fit to data, runs 17 & 18. Dotted vertical bars show averaging interval on runway.

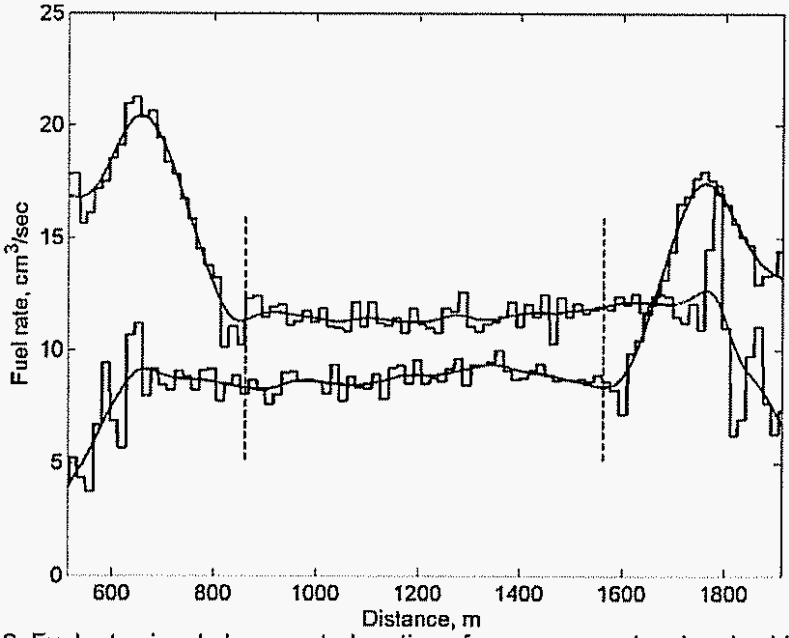

Figure 12. Fuel rate signal along central portion of runway, raw signal and cubic-spline fit to data, runs 17 & 18. Dotted vertical bars show averaging interval on runway.

Figure 13 shows the smoothed fuel consumption signal, but now only over the window actually used for averaging. The cubic-spline smoothing used in figure 13 (and in figure 12) is useful in estimating the termination points of the acceleration period (in both directions), and in providing a measure of the quality of the signal in the constant speed, overlap window.

The cubic-spline smoothing does not remove the run-to-run variability caused by fuel rate fluctuations, as might at first be presumed. It can easily be demonstrated that computing fuel consumption from the unsmoothed signal or from the smoothed result—over the identical distance window—gives identical results to better than one part in two thousand. The reason is that the value of the smoothed curve must still reflect the shape of the unfiltered signal. The fuel rate fluctuations are diminished by widening the averaging window—in our case the window can be 700 meters in length, but no longer.

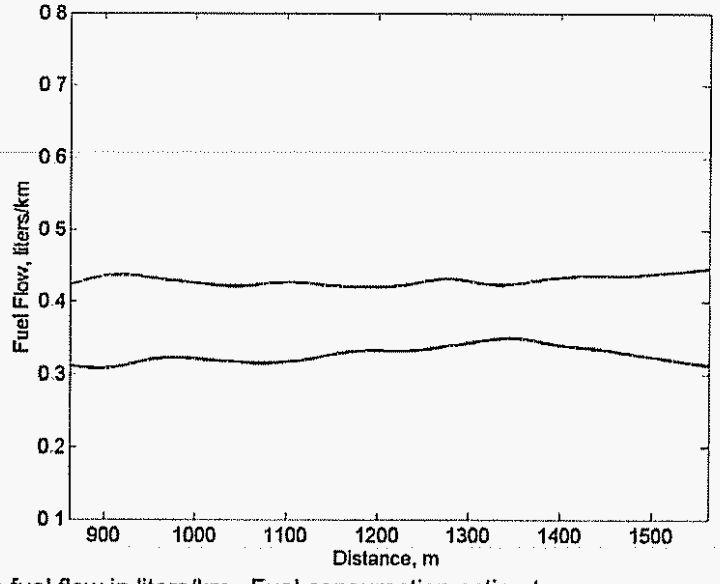

Figure 13. Cubic-spline fit to fuel flow in liters/km. Fuel consumption estimates are averages of this signal over the distance window shown above (runs 17 & 18). Average over window, 0.4295 (southbound), 0.3278 (northbound).

The difference between the northbound and southbound values of fuel consumption in figure 13 is a result of the difference in runway elevation change and of the effect of wind.

6.3 NORTH-SOUTH RUN-PAIRS MINIMIZE THE EFFECT OF RUNWAY SLOPE AND OF WIND

The *difference* between northbound and southbound runs—averaged for each of the 19 data sets—is shown in figure 14 plotted versus the component of wind speed parallel (tangential) to the runway. The dotted bars represent the standard deviations for the eight trials comprising each data set. The zero wind point is indicated by the heavy cross. Negative values of wind represent wind blowing toward the south. Each symbol corresponds to a particular value of flap angle.

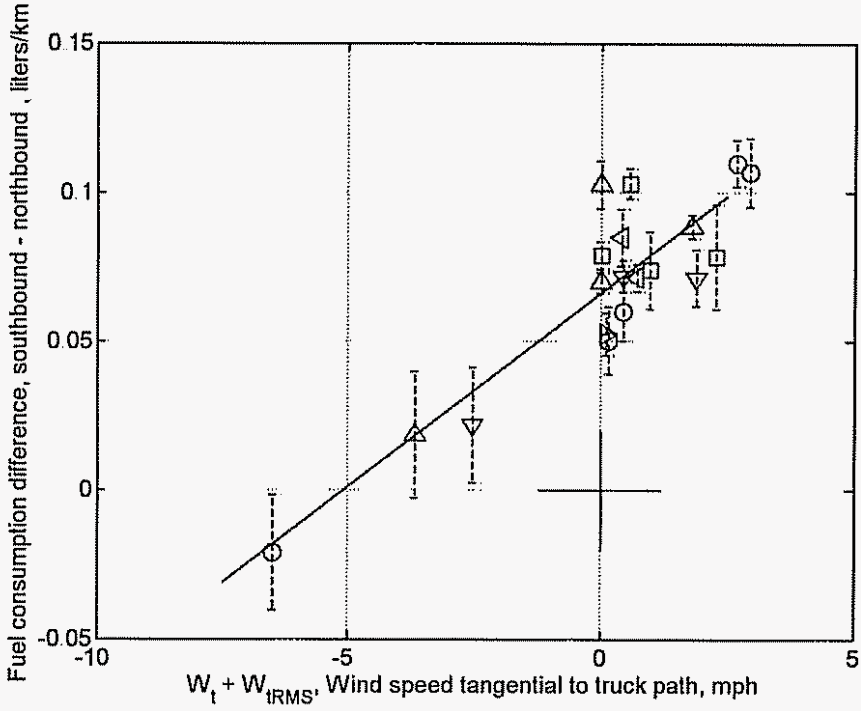

Figure 14. Difference in fuel consumption traveling north and south versus wind.

The data lay more-or-less along a straight line from lower left to upper right. A least-squares line has been drawn to aid the eye. The effect of the slope of the runway is the offset at zero wind speed. It is about 0.07 liters/km and represents the additional fuel expenditure (or saving) required to travel uphill (downhill) along the runway. Within the measurement interval on the runway (figure 2b), the slope is nearly constant and of value 0.384 meters per 100 meters upwards to the south.

The differences in north-south travel also depend substantially on the wind speed—that is depicted by the variation with increasing wind speed. The effects of runway slope and of variation of wind speed are about the same order of magnitude for the winds encountered here.

The effect of runway slope can be entirely eliminated by averaging a southbound-northbound run-pair, for then there is no net elevation gain or loss. Southbound-northbound run-pairs are averaged for each of the 19 data sets, and the results are plotted in figure 15 against the most appropriate wind variable, which—for the run-pairs—is the rms tangential wind component. The dotted bars are the measured standard deviations for the fuel consumption for each data set. Again, the different symbols correspond to the different flap angles tested.

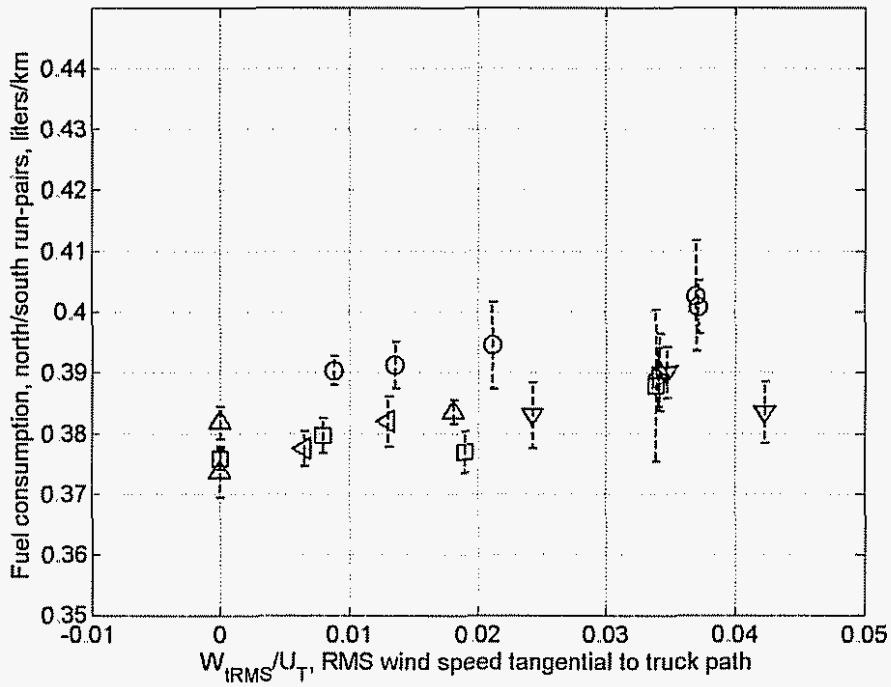

Figure 15. Fuel consumption of north-south run-pairs as a function of the normalized RMS tangential wind speed.

The fuel consumption for north-south run-pairs still depends upon wind speed, but to a much lesser extent. The standard deviations of the data sets (dotted lines) tend to increase with increasing wind also. The five control runs without flaps are the circles. These runs have the highest fuel consumption values indicating highest drag, but they also seem to exhibit the greatest variation with wind. Fuel consumption for some of the other flap angles seems less dependent upon wind.

To see why wind effects might be minimized by averaging southbound-northbound run-pairs, we refer to a simple theoretical model describing the aerodynamic forces seen by the truck.

In the presence of a wind, W, the aerodynamic forces in the horizontal plane consist of a drag and a side force measured in wind axes, as in figure 16. Here U_T is the truck speed as seen by the

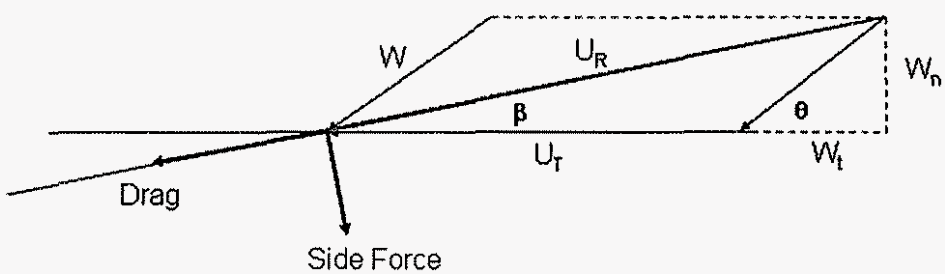

Figure 16. Force vector geometry in the presence of wind.

truck, W_t and W_n are the tangential and normal components of the wind vector, respectively, and U_R is the resultant wind vector. The expression for the instantaneous aerodynamic force in the direction opposite to truck travel (axial force in body axes) is:

$$\text{Axial Aerodynamic Force} = \text{AAF} = (\text{Drag}) * \cos(\beta) - (\text{Side Force}) * \sin(\beta) \qquad (1)$$

If the wind is a small fraction of the truck speed—as it is in almost all cases tested—the force can be shown to be approximated by a power series:

$$W_n/U_T \ , \ W_t/U_T << 1$$

$$\text{AAF} = C_{Do} S \frac{\rho}{2} U_T^2 \left[1 + 2W_t/U_T + \left(\frac{W_t}{U_T} \right)^2 \right] + \left(C_{Do} + \frac{\partial^2 C_D}{\partial \beta^2} - 2 \frac{\partial C_{SF}}{\partial \beta} \right) S \frac{\rho}{2} U_T^2 \left[\frac{1}{2} \left(\frac{W_n}{U_T} \right)^2 \right] + \text{O}(W/U_T)^3 \ldots \qquad (2)$$

The first three terms in the power series expansion depend only upon the drag coefficient evaluated at zero yaw, C_{Do}, and upon the *tangential* component of the wind—that is the component of the wind in the direction of travel. The next term depends quadratically upon the small, normal wind component, W_n/ U_T, and in a more complicated way upon the drag and side force variation with yaw angle, β. The remaining terms are of still higher order in small quantities.

Referring again to the wind ellipses in figure 9, the quantities, W_t/U_T and W_n/U_T are always less than 0.1 (there is one exception), insuring that the quadratic terms in the preceding expression are at least an order of magnitude smaller in comparison to the first two terms. Retaining only these two terms, and now adding the rolling resistance, (Mg)r, and the climbing force, (Mg)sin(ϕ), the power expended can be expressed as:

$$\text{Power expended} = \text{P} = U_T \left\{ C_{Do} S \frac{\rho}{2} U_T^2 [1 + 2W_t/U_T + \ldots] + (Mg)r + (Mg)\sin(\varphi) \right\} \qquad (3)$$

Here Mg is truck weight, r is the rolling resistance coefficient, and tan(ϕ) is the runway slope. Fuel consumption is proportional to power expended, and therefore:

$$\text{Fuel Consumption} = \text{FC} \approx U_T \left\{ C_{Do} S \frac{\rho}{2} U_T^2 [1 + 2W_t/U_T + \ldots] + (Mg)r + (Mg)\sin(\varphi) \right\} \qquad (4)$$

The terms (Mg) sin(ϕ) and W_t/U_T change sign when the direction of travel is reversed. Adding a southbound and a northbound run exactly cancels the climbing term, and would cancel the wind effect *if the wind were steady*. Since the wind is never steady, there will be some residual effect of wind upon fuel consumption for the run-pairs. The relevant term is underlined in equation (5) below.

$$\text{FC for run - pair} = \left(\frac{\text{FC}_S + \text{FC}_N}{2} \right) \approx U_T \left\{ C_{Do} S \frac{\rho}{2} U_T^2 \left[1 + \underline{\left(W_t/U_T \right)_S - \left(W_t/U_T \right)_N} \right] + (Mg)r \right\} \qquad (5)$$

Averaging over the eight run-pairs in a data set makes the wind term even smaller. The result is the wind effect observed in figure 15. There is probably no way to avoid this uncontrolled, but small, contamination from wind.

7. RESULTS

7.1 ESTIMATING AVERAGE FUEL CONSUMPTION SAVINGS

Fuel consumption as a function of flap angle for all the data recorded is plotted in figure 16. The nineteen data sets are plotted as average values for the eight run-pairs comprising the set; the ± one standard deviation for each set is denoted by the dotted bars. Note that the no-flaps control is plotted at the 25-degree flap angle for convenience of scale.

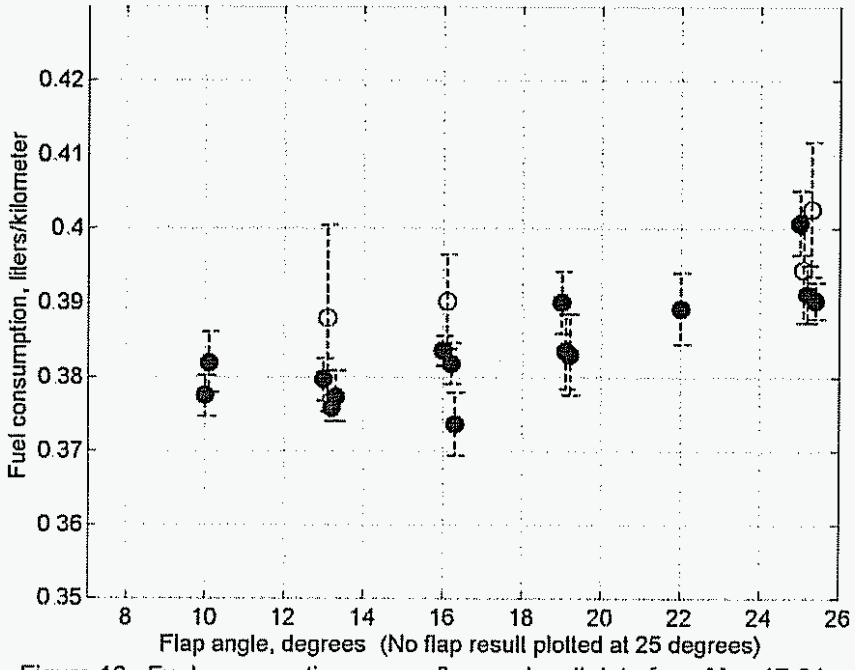

Figure 16. Fuel consumption versus flap angle, all data from May 17-21.

It is clear from this data presentation that the addition of base flaps produces lower aerodynamic drag and leads to fuel consumption savings, and that the flap angles 10° – 16° are the most effective. Most of the individual data sets are consistent, and have standard deviations of the order of 1% or less. The four data sets indicated by the open circles have standard deviations greater than 1.5%. In several of these cases, the mean values are also higher. Winds affect a portion of the data more than other portions. The task is to make the best possible estimate of performance from these data.

Several possibilities are explored.

(i) Simply average all the data available, regardless of wind condition or the size of the standard deviation of the data set. In this case, the data sets for each flap angle are combined. A single average value, and a single standard deviation, is output for each flap angle.

(ii) Regard wind as a potentially important variable, and reject data sets recorded at the larger values of wind speed. Choosing a cut-off wind-speed is a subjective decision. Referring to figure 15 and to the previous analysis, choosing the cut-off at $W_{tRMS}/U_T = 0.035$ would reject only three data sets. The result is not likely to be very different from keeping all data. The next reasonable cut-off is chosen, $W_{tRMS}/U_T = 0.025$. This value rejects seven of the nineteen data sets. For each flap angle, combine all the data sets with $W_{tRMS}/U_T \leq 0.025$. A single

average value and a single standard deviation is output for each flap angle under these conditions.

(iii) In this choice, regard the standard deviations of the individual data sets as the measure of most importance. Large deviations within a data set may come from wind or from other undetermined causes. Whatever the reasons, reject the data sets that have standard deviations greater than 1.5%. For each flap angle, combine all the data sets with standard deviations ≤1.5%. A single, average-value, and a single standard deviation is output for each flap angle under these conditions. Four of the nineteen data sets are ignored. This is the choice we prefer.

The results from making each of these three choices is shown in figure 17, which is the main result of the paper.

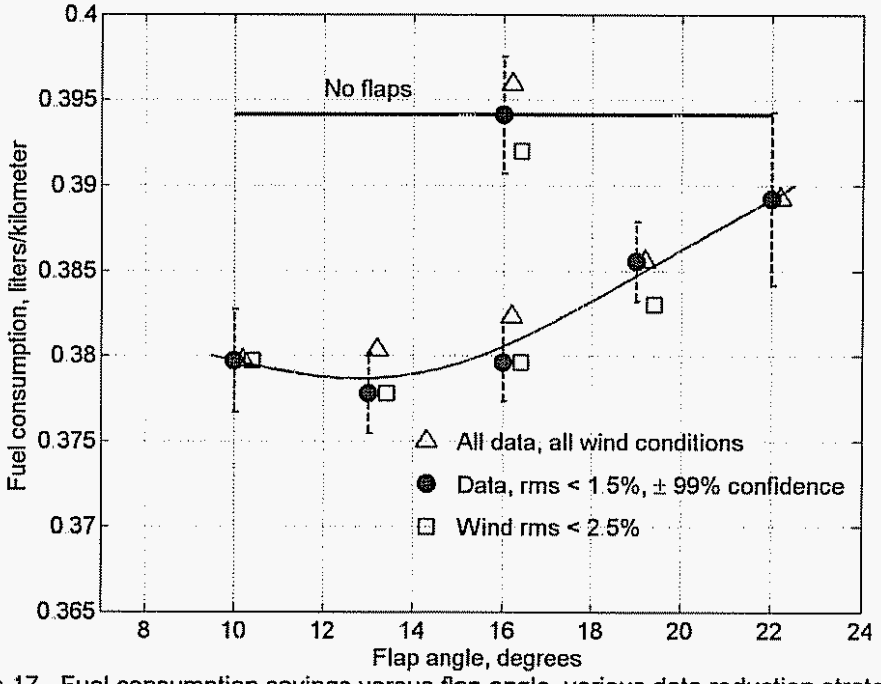

Figure 17. Fuel consumption savings versus flap angle, various data reduction strategies.

Plotted as the solid symbols are the averaged results—excluding the four data sets showing the least internal consistency (data set rms > 1.5%). In addition, the dashed bars give the estimated 99% confidence interval for each flap angle. The confidence interval is determined from the standard deviation estimate at each flap angle. A 99% confidence interval suggests that if the tests are repeated under the same conditions, the averaged values will lie within the bounds of the confidence bars 99% of the time. While our repeated sampling over the week-long period does not alter the variability inherent in the data, repeated sampling does provide a much more accurate estimate of the mean (averaged) values.

Also shown are the two other data reduction choices—triangles indicate the result when all the data is utilized, and squares indicate the result when only runs at low wind intensity are kept. These three results are not substantially different—they all lie within the 99% confidence bounds. Expressed as a fraction of the fuel consumption without flaps, the averaged values are accurate to about ±0.6%. This is the demonstrated accuracy of the *relative* measurement of fuel consumption savings.

A final comment about variations in temperature during the tests is in order. The portion of the fuel consumption required to overcome aerodynamic drag is directly proportional to air density (as in equation (4) or (5)), and will thus depend upon air temperature and atmospheric pressure at the times of the individual tests. As mentioned earlier, the departures from sea level standard pressure are small. However, temperature varies by as much as ±10°F over the testing period each day. Undoubtedly, some of the variation shown in figures 16 & 17 is a result of the effect of temperature variation upon density variation. We have evaluated the average density for each data set, relative to the density at standard conditions, ρ_{STD}=1.226 Kg/m^3 at p_{STD}=1.0135 10^5 Pa and T_{STD} = 288 K. The values are never greater than 1.02 and never smaller than 0.98. Furthermore, the testing of different flap angles takes place at different times during the morning, and the density averages *for each flap angle* lay much closer to unity—almost always within the bounds $0.99 \le \rho_{AVERAGE}/\rho_{STD} \le 1.01$. The effect of density variation is difficult to separate from the effect of wind because there is a strong correlation between warming in the morning and the onset of wind. Taken together, the two are probably responsible for most of the residual ±0.6% variation remaining in the figure 17 plot.

7.2 COMPARISONS WITH WIND TUNNEL EXPERIMENTS

The field test results can be compared with previous wind tunnel measurements. Here we will look only at the *difference* in drag associated with the use of flaps or no flaps. In the wind tunnel, changes in drag—or drag coefficient—are measured rather than changes in fuel consumption. To compare with the wind tunnel tests, the fuel consumption changes measured during this field test must be converted to drag coefficient changes. The relationship between fuel consumption and power expended can be expressed as

$$\mathrm{FC} = \left(\frac{\mathrm{sfc}}{\rho_f}\right)\mathrm{P_{FW}} \quad , \quad \mathrm{P}_W = \eta_d \mathrm{P}_{FW} \quad \rightarrow \quad \mathrm{FC} = \left(\frac{\mathrm{sfc}}{\rho_f}\right)\left(\frac{1}{\eta_d}\right)\mathrm{P}_W \tag{6}$$

In the first expression, (sfc/ρ_f) is the volume of fuel consumed per unit of power delivered at the engine flywheel, (P_{FW}). The factor (η_d)≤1 is a drive-train efficiency, and relates power at the rear wheels, P_W, to the power delivered at the flywheel. Take the last expression, and rewrite it as an expression for the *difference* in fuel consumption with and without flaps. Since this *difference* in fuel consumption depends only upon drag differences, the expression is relatively simple.

$$\Delta\mathrm{FC} = \mathrm{FC}_{NF} - \mathrm{FC}_F = \left[\left(C_{Do}\frac{\rho_{AV}}{\rho_{STD}}\right)_{NF} - \left(C_{DoF}\frac{\rho_{AV}}{\rho_{STD}}\right)_F\right]\left(\frac{\mathrm{sfc}}{\rho_f}\right)\left(\frac{1}{\eta_d}\right)\left(\frac{\rho_{STD}}{2}U_T^2 S\right)U_T \tag{7}$$

The subscripts NF and F refer to no-flaps and flaps, respectively. The quantity (ρ_{AV}/ρ_{STD}) refers to the ratio of air density averaged over all run-pairs at a given flap angle compared to air density at standard conditions; U_T and S are respectively the truck speed and truck cross-sectional area. Finally, set (ρ_{AV}/ρ_{STD})=1 as a good approximation, and solve for ΔC_D,

$$\Delta C_D = \left[C_{DoNF} - C_{DoF}\right] = 2\left(\frac{1}{\rho_{STD}U_T^2 S}\right)\left(\frac{\rho_f}{\mathrm{sfc}}\right)\eta_d\left[\frac{\mathrm{FC}_{NF} - \mathrm{FC}_F}{U_T}\right] \tag{8}$$

The last quantity in square brackets is the difference in fuel consumption given in figure 17, for any flap angle, in units of liters/km. The other unknown on the right-hand-side, (sfc/ρ_f), can be obtained by using the engine torque combined with the engine rpm, and the broadcast fuel rate outputs on the

J1939 bus. For all practical purposes, (sfc/ρ_f) is a constant determined to be 0.596×10^{-4} liters/N-km. The drive-train efficiency must still be approximated. After discussion with Cummins personnel, a value of $\eta_d = 0.92$ is chosen, reflecting the improved efficiency from the use of synthetic lubricants.

The values of ΔC_D estimated from the field test for the five flap angles tested are shown in figure 18. As a measure of the reliability of the data, the same 99% confidence intervals are also shown (properly scaled for ΔC_D). The experimental results from four wind tunnel tests are also shown as the dashed or solid lines. These lines represent cubic-spline fits to the wind tunnel data. The dashed-red and solid-red lines (Re = 2.3 and 3.6×10^5, respectively) are USC results using a simplified wind tunnel model resembling a trailer but having an aerodynamic nose and no wheels (Hsu et al. 2004). Flaps of length L = 0.25W extend from the sides and the top and bottom of the base. The two solid-blue curves are two results from Cooper (Cooper 1985, Cooper 2003) for the change in drag averaged over a range of yaw angles (wind-averaged drag coefficient) for a straight-sided truck having a rounded front, wheels and undercarriage at Re = 1.5×10^6, and for a tractor-trailer having some rounding at the trailer roof (but a mismatch between the cab and trailer) at the same Reynolds number. Base flaps of length L = 0.19W are fitted to the top and sides. The upper blue curve is for the straight-sided truck model and the lower blue curve is for the tractor-trailer model.

The dotted blue curve is from a recent wind tunnel test in the 12-foot pressurized wind tunnel at NASA Ames at full scale Reynolds numbers of about Re = 5×10^6. The truck model is a generic tractor-trailer having axels and wheels, but no detailed undercarriage modeling (Storms et al. 2004). Flaps of length L = 0.25W are fitted to the sides and to the top and bottom of the base.

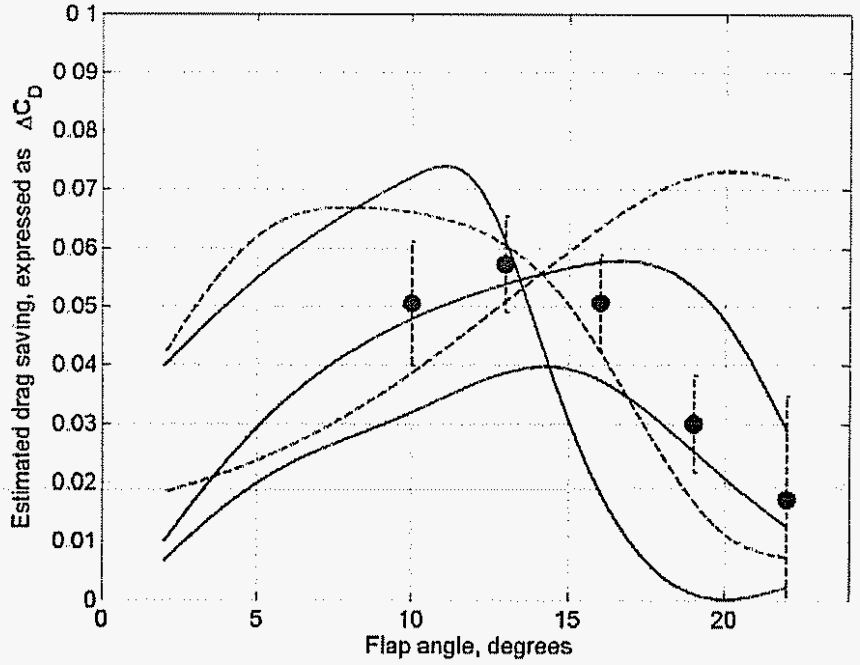

Figure 18. Comparison between ΔC_D derived from the field test (shown as red symbols), and four wind tunnel experiments. In order of increasing Reynolds number, the experiments are: - - - USC, Re = 2.3×10^5; —— USC, Re = 3.6×10^5; —— Cooper (1985), Re = 1.5×10^6; – – NASA Ames test, Re = 5×10^6.

All of the wind tunnel models are different from one another and differ from the actual truck used in the field test. In spite of these differences, there is general agreement that the *magnitude* of the drag change associated with the use of base flaps is in the range $\Delta C_D \approx 0.04 - 0.07$. The general agreement would suggest the drag reduction achieved by base flaps is robust, and that it is relatively

insensitive to the details of the truck geometry. However, the base flap angle for which maximum drag saving occurs varies from about 8°-10° at the lower Reynolds numbers to about 20° for the NASA Ames test at full scale Reynolds number. We expected the field test data to have maximum drag reduction for base flap angles in the range 16°-20°, but this is not the case. The optimum base flap angle for the field tests is more like 13°.

7.3 IMPLICATIONS FOR FLEET OPERATIONS

There is minimum fuel consumption at a flap angle of about 13 degrees, but the minimum is broad—the fuel consumed at 10 degrees and 16 degrees is only marginally greater. It would be advantageous from an operations standpoint to have such a broad minimum.

The saving in fuel consumption arising from the use of base flaps at a 13° flap angle is 1.63 liters/100 km, or in gallons and miles, 0.693 gal/100 miles. A dollar values can be placed on the accumulated saving by assuming a price for fuel. Figure 19 shows the results for a fuel price of $2.20/gal for distances of 50,000 and 100,000 highway miles traveled.

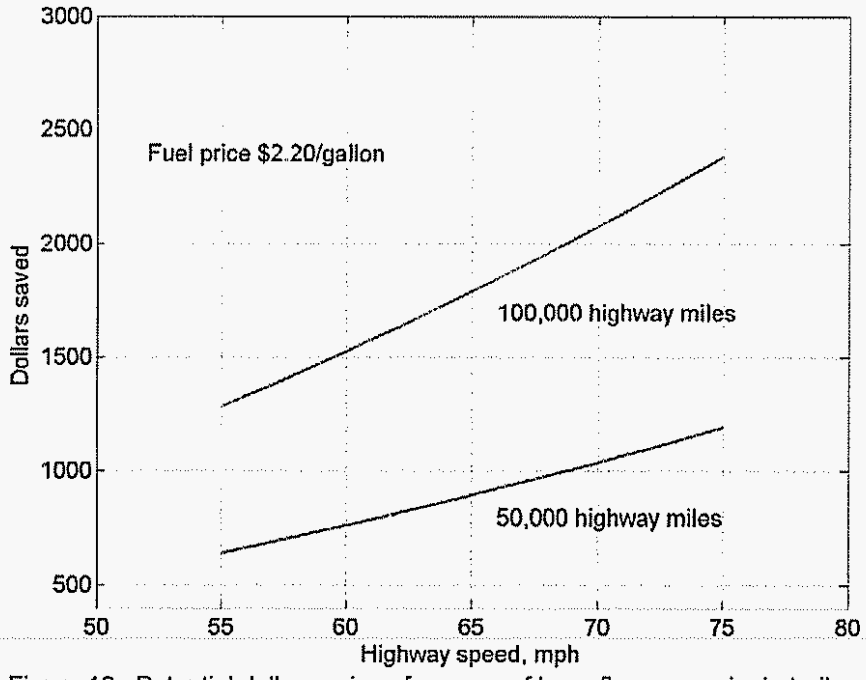

Figure 19. Potential dollar-savings from use of base flaps on a single trailer.

These savings represent the increment associated only with the change in drag due to the presence or absence of flaps. The result will hold for any truck of similar size and shape and engine performance regardless of the loading of the truck or the rolling resistance.

The horizontal axis in figure 19 is highway speed. Although the tests presented here are performed at 60 mph, the results are easily extrapolated to other speeds because the fuel needed to travel a given distance is quadratic in speed. (This fact can be seen from equation (7) by remembering that fuel consumption per unit distance is $\Delta FC/U_T$, leaving U_T^2 remaining on the right hand side.) Dollar savings from the use of flaps is greater at higher speeds, because aerodynamic drag is a larger fraction of the total resistance. However, total fuel consumption will increase with increasing speed.

7.4 ECONOMY RESULTING FROM THE CLOSE-FOLLOWING OF TWO TRUCKS

The previous economy achieved by use of base flaps can be compared to the economy resulting from driving two trucks in a tandem configuration. In December 2003, such fuel consumption tests were performed at the same Crows Landing test-site under the sponsorship of the California PATH Program. In the tests, two identical trucks are operated at headways in the range 3–10 meters. The trucks are steered by hand, but longitudinal control is provided by a closed-loop control system. Laser ranging measures truck-to-truck distance, and the control system maintains a truck separation to within about ±3 centimeters.

Figure 20 shows several views of the two trucks in tandem at short headway. The trucks are identical to all outward appearance, with the exception of the lidar reflector clamped to the base of the lead truck.

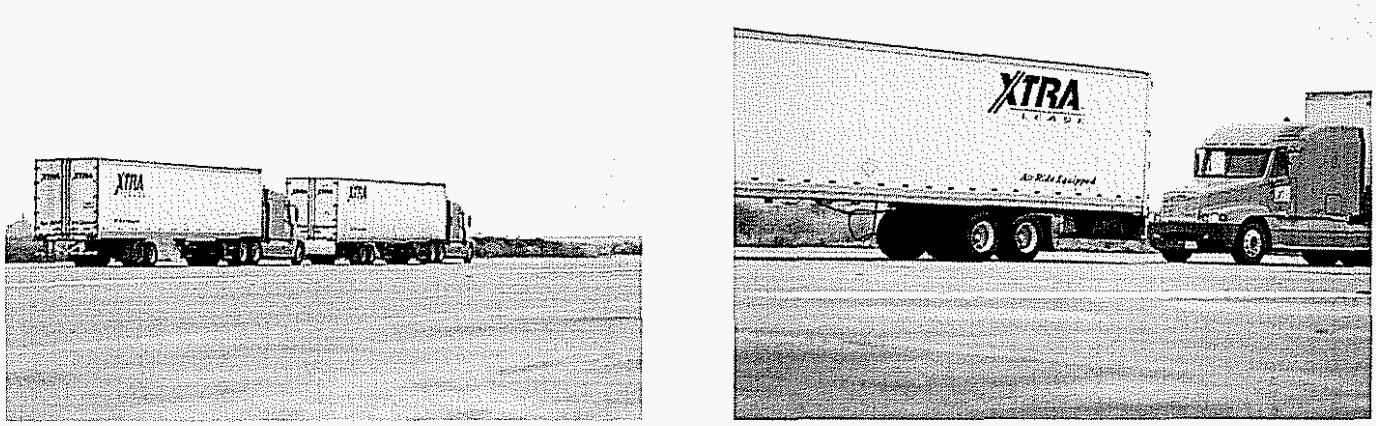

Figure 20. Close-following trucks at Crows Landing in December, 2003 (see Browand, McArthur & Radovich, 2004).

The data for this field test has been plotted in figure 21 as fuel saving in liters/100 km separately for the lead and the trail truck as a function of truck separation. In this case fuel saving is the averaged *difference* in fuel consumption for either truck in isolation minus the fuel consumption for the same truck in close-following.

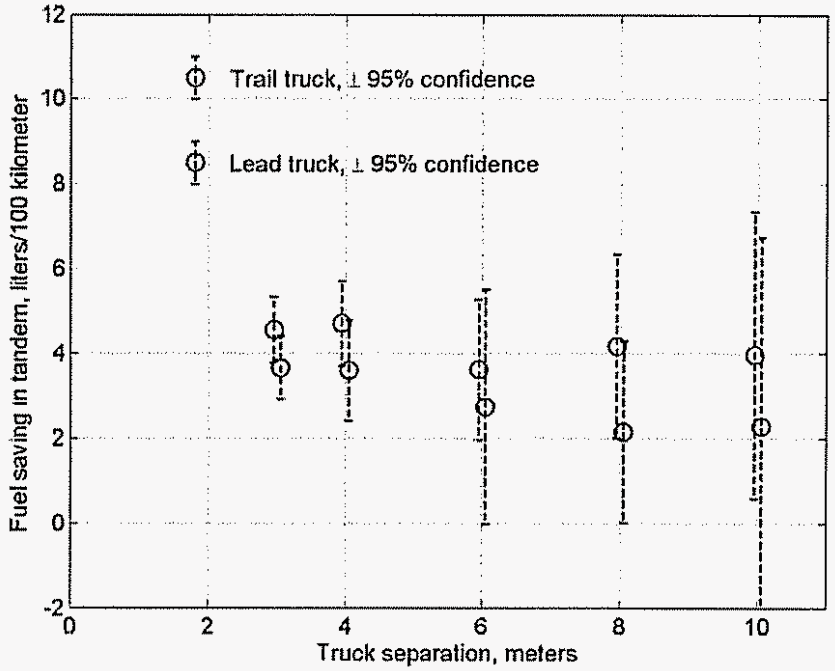

Figure 21. Fuel saving for each truck in tandem geometry versus truck separation (Browand, McArthur & Radovich 2004).

It can be observed that both trucks save fuel by close-following, that the fuel saving increases with decreasing spacing, and that the trail truck saves more fuel. The bars on the data plot represent the 95% confidence limits for the mean values at each value of spacing. The data is not as reliable for these tests for two reasons. First, the tests were conducted over a shorter time period, and therefore represent fewer trials. Second, the overlap interval along the center portion of the runway is shorter, so that the average value for each trial is not as reliable. A more complete description of the tests can be found in Browand, McArthur & Radovich, 2004.

If an average value of fuel saving for the two trucks at spacings of 6-10 meters is taken to be 3.0 liters/100 km, a dollar-saving plot similar to figure 19 can be prepared as shown in figure 22.

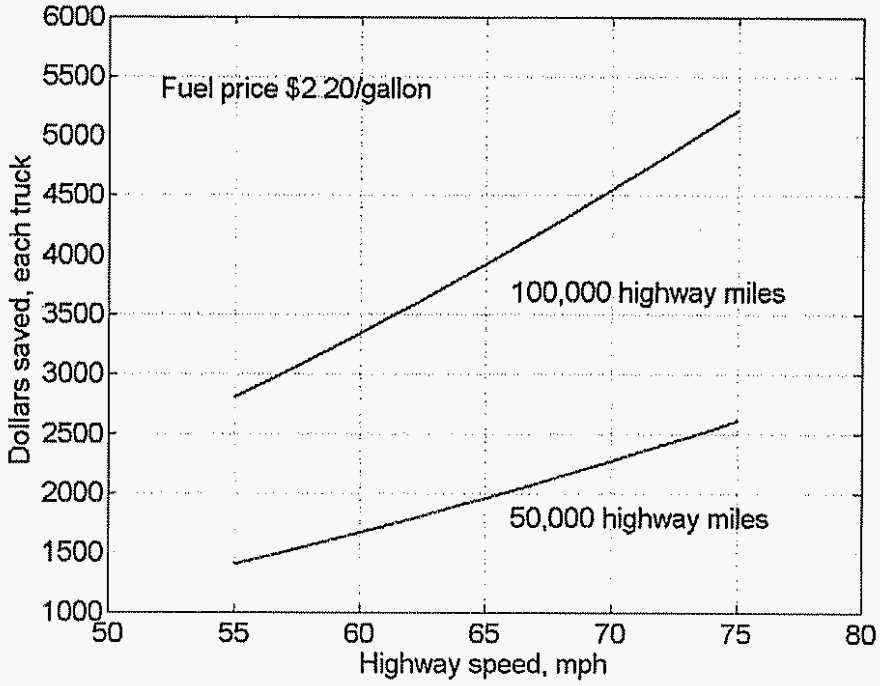

Figure 20. Potential dollar-savings for tandem travel at 6-10 meter spacing.

The savings achieved for tandem travel are considerably greater than those associated with the use of base flaps. Of course the trucks would require automatic throttle and braking to operate under computer control, and this would require additional investment. However, it might be easier (and less expensive) to operate in the separation range 6-10 meters than at closer spacings.

8. CONCLUDING REMARKS

To place these fuel saving results in a larger context, the U.S. Department of Transportation notes that in the year 2000[1], combination trucks (tractors with trailers) accumulated a total of 135,000 million miles (217,000 million kilometers) on the highways of this country. Assuming that half of these miles are run at highway speed of the order of 60 mph (≈100 km/hr), and that half the trailers hauled might be equipped with base flaps—saving 0.693 gal/100miles (1.63 liters/100km)—projects a potential yearly saving of the order of 250 million gallons (950 million liters) at an equivalent yearly dollar saving of about $0.5 billion at today's fuel price. The figure of 250 million gallons, or 6 million barrels, represents—approximately—the total U.S. oil production for about 1 day. An equivalent number—350 million gallons saved—can be obtained by assuming each of 1 million trailers to be equipped with base flaps (this is roughly half the number of tractors registered in the year 2000), and travel 50,000 miles each year at highway speed.

These numbers, while impressive, are only a small fraction of the total fuel consumption by heavy trucks on the highways of the nation each year. Taking the figure of 135 billion miles per year, and assuming a fuel economy of 5.3 miles per gallon (2.25 km/liter), gives a total of 600 million barrels consumed per year—a number that represents the total U.S. oil production for about 100 days[2].

[1] U.S. Department of Transportation, Federal Highway Administration, Highway Statistics (Washington, DC: Annual issues), and Internet site www.fhwa.dot.gov/ohim/ohimstat.htm (see summary tables, U.S. vehicle miles, table I-32)
[2] Transportation Energy Data Book:Edition 23, Oak Ridge National Laboratory, www-cta.ornl.gov/data

Diesel fuel is about 87% carbon by weight, and most of this carbon is converted to carbon dioxide by combustion—resulting in 10-12 Kg of CO_2 for each gallon of diesel fuel burned. Heavy trucks on the highway are therefore responsible for some 250 million metric tons of CO_2 release each year. Use of base flaps installed on half the truck fleet, so that each tractor hauls a trailer equipped with base flaps half the time as above, would decrease this number by about 2.5 million metric tons per year.

9. ACKNOWLEDGEMENTS

We gratefully acknowledge the financial support and guidance of DOE, Heavy Vehicle Systems Technology, Office of FreedomCAR and Vehicle Technology, under the supervision of Dr. Sidney Diamond, and Dr. Jules Routbort. We appreciate the assistance of California PATH in providing support for the field test—in particular the help of Scott Johnston who performed the driving duties and organized the effort on behalf of PATH. We also thank Ben Zwissler of Cummins Engine for numerous helpful discussions.

10. REFERENCES

Browand, F., McArthur, J. & Radovich, C., 2004, "Fuel Saving Achieved in the Field Test of Two Tandem Trucks," California PATH Research Report UCB-ITS-PRR-2004-20, June, 2004.

Buckley, F., 1985, "An Improved Over-the-Road Test Method for Determining the Fuel Saving Benefit of a Truck Aerodynamic Drag Reducing Device," SAE paper No. 850285, Detroit, Michigan, Feb 25-Mar 5, 1985.

Cooper, K., 1985, "The Effect of Front-Edge Rounding and Rear-Edge Shaping on the Aerodynamic Drag of Bluff Vehicles in Ground Proximity," SAE paper No. 850288, Detroit, Michigan, Feb 25-Mar 1, 1985.

Cooper, K., 2003, "Truck Aerodynamics Reborn – Lessons from the Past," SAE paper No. 2003-01-3376, reprinted from SP-1814, Fort Worth, Texas, Nov 10-12, 2003.

Hsu, T-Y., Hammache, M. & Browand, F., 2004, "Base Flaps and Oscillatory Perturbations to Decrease Base Drag," Proceedings of the UEF Conference on **The Aerodynamics of Heavy Vehicles:Trucks, Buses and Trains**, Lecture Notes in Applied and Computational Mechanics Springer-Verlag, Heidelberg, September, 2004.

Lanser, W., Ross, J. & Kaufman, A., 1991, "Aerodynamic Performance of a Drag Reduction Device on a Full-Scale Tractor/Trailer," SAE paper No. 912125, Long Beach, California, Sept 23-26, 1991.

Saunders, J., Watkins, S., Hoffmann, P. & Buckley, F. Jr., 1985 "Comparison of On-Road and Wind-Tunnel Tests for Tractor-Trailer Aerodynamic Devices, and Fuel Savings Predictions," SAE paper No. 850286, Detroit, Michigan, Feb 25-Mar 1, 1985.

Storms, B., Satran, D., Heineck, J. & Walker, S., 2004, "A Study of Reynolds Number Effects and Drag-Reduction Concepts on a Generic Tractor-Trailer," AIAA paper No. 2004-2251, Portland Oregon, Jun 27-Jul 1, 2004.

Visser, K. & Koon, J., 2004, "Drag Reduction of a Tractor-Trailer Using Planar, Non-Ventilated Cavities," Proceedings of the UEF Conference on **The Aerodynamics of Heavy Vehicles:Trucks, Buses and Trains**, Lecture Notes in Applied and Computational Mechanics Springer-Verlag, Heidelberg, September, 2004.

Final Report, Part II

Experimental Measurement of the Flow field of Heavy Trucks

DE-AC26-98EE50512

Splash and Spray

Fred Browand, Adam Fincham, Tai Merzel,
Dennis Plocher and Charles Radovich

University of Southern California

Aug 22, 2005

Table of Contents

INTRODUCTION

A key factor in driving safety is driver visibility. Tires driving through standing water create splash and spray which can decrease visibility for other drivers. Studying the formation of splash and spray will help in the understanding of how to maintain visibility.

Splash is water that is pushed out from the tire patch towards the sidewall of the tire. Spray is defined as the water forced into the tread pattern within the tire patch (contact patch) between the tire and the road. It is spray that we will be interested in here.

When tires produce spray, the water droplets form as a result of the break-up of jets and sheets of fluid. The physics of the jet and sheet break-up can be thought of in terms of several simpler problems studied in the literature.

Jet break-up

Consider the problem of a solitary jet first studied by Rayleigh in about 1883, and sketched below in Figure 1. As the solitary jet column of diameter D travels, oscillations form from random disturbances and grow because the jet is unstable. The unstable waves travel with a wave speed equal to the jet speed U, and have a non-dimensional wave length λ/D, where the wave length is $\pi < \lambda/D < \infty$.

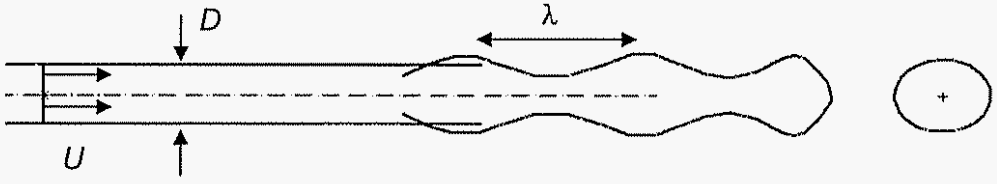

Figure 1. Solitary jet forming droplets.

Droplets are formed when the disturbances grow to sufficient magnitude to "pinch off". The most unstable wave produces droplets of size:

$$D_{droplet} = 1.89 \cdot D \qquad (1)$$

The instability of the jet is driven by surface tension, as can be seen by referring to Figure 2. At wave crests, where the jet bulges, the local radius of curvature of the jet is less and the fluid pressure within the jet is lower. At wave troughs, the radius of curvature is smaller and the fluid pressure is larger. The pressure difference within the jet moves fluid from the trough to the crest causing wave growth.

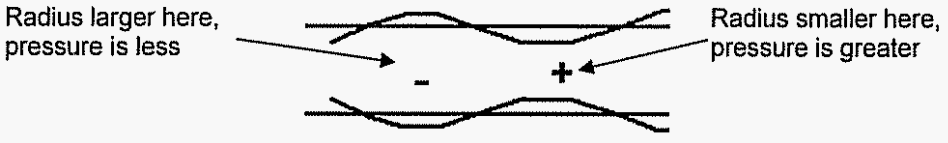

Figure 2. Jet instability is caused by surface tension.

The addition of quiescent air external to the jet adds additional pressure disturbances that are in phase with the pressures shown above, and further destabilizes the jet. This is most easily seen by moving in a reference frame riding with the wave, as in figure 3 below. From this reference frame, the external air is seen moving to the left at the speed of the wave, V_g, which is (nearly) equal to the speed U. From this reference frame, the air is seen flowing to the left, and producing pressure differences (Bernoulli's equation) along the boundary of the jet that favor the instability.

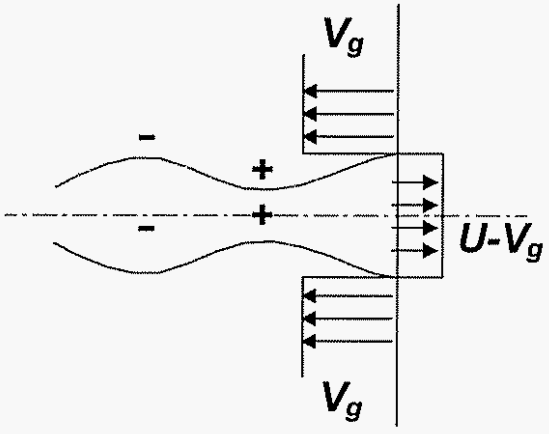

Figure 3. Riding with the jet in the presence of surrounding air.

Sheet break-up

Sheets of fluid are also involved in the production of spray. Deformed sheets are stable when by themselves, Figure 4. In the case of a sheet, the surface tension produces pressures (or forces) that restore the sheet to its original, un-deformed condition. For both varicose and sinuous waves (shown below), surface tension can lead to surface wave propagation along the sheet, but not to waves that grow in time.

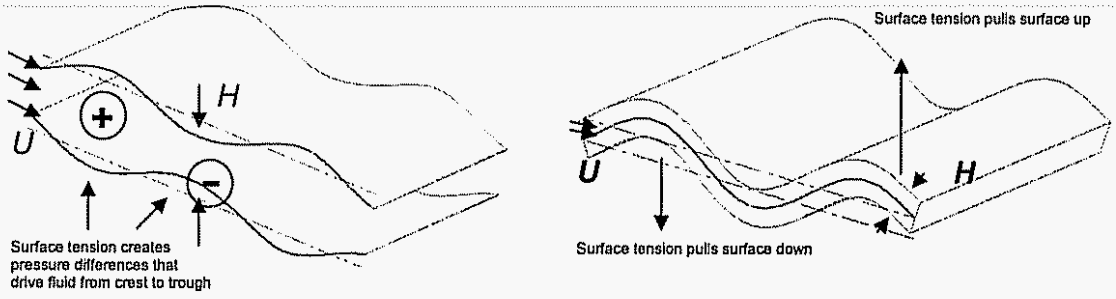

Figure 4. Only stable, traveling waves are possible on a sheet as a result of surface tension.

However, a surrounding air mass can destabilize the sheet, as shown below in Figure 5. Again, ride with the wave in the sheet and observe that the air mass is moving to the left at speed $V_g \approx U$. The pressure difference across the sheet produced by this motion is sufficient to create the unstable behavior.

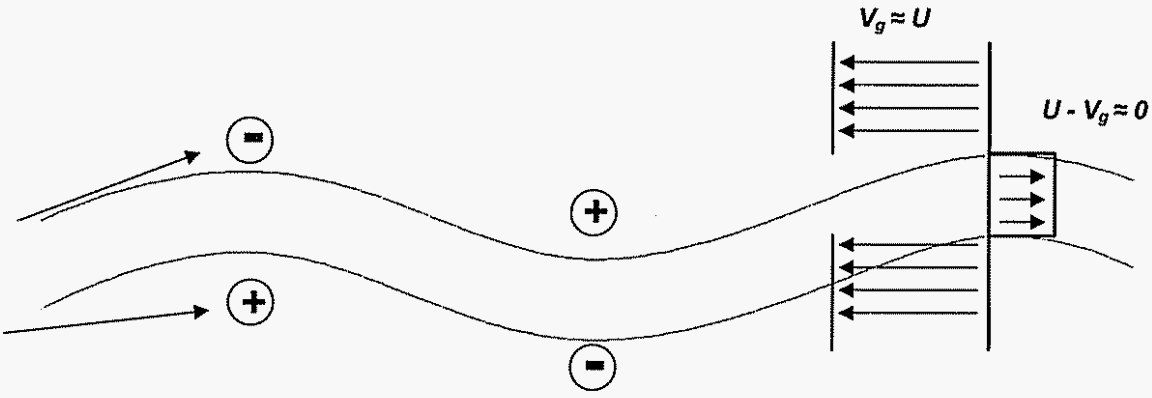

Figure 5. Pressure difference produced by the air mass on either side of the sheet drive the sheet laterally.

Sinuous disturbances, as depicted above, are usually the more unstable. The sheet will break up into droplets if the amplitude of the wave grows sufficiently large. Since the sheet is driven unstable by the inertia of the surrounding air, the larger the inertia the more violent the wave growth. The Weber number is a dimensionless quantity that relates the effective measured inertia to the (restorative) surface tension:

$$We = \frac{\rho_{liq} U^2 H}{\sigma} \tag{2}$$

where σ is the surface tension, and H is the sheet thickness. For a jet of diameter D, the Weber number becomes:

$$We = \frac{\rho_{liq} U^2 D}{\sigma} \tag{3}$$

The larger the Weber number, the more violent the sheet (or jet) break-up and the smaller the droplets that are formed. A simple example of a sheet break-up was studied by Clanet & Villermaux (2002), as shown in Figure 6. This experiment directs a laminar water steam of diameter D_0 onto a small post of diameter of D_i. As the jet impacts the post, it is forced to spread radially outward.

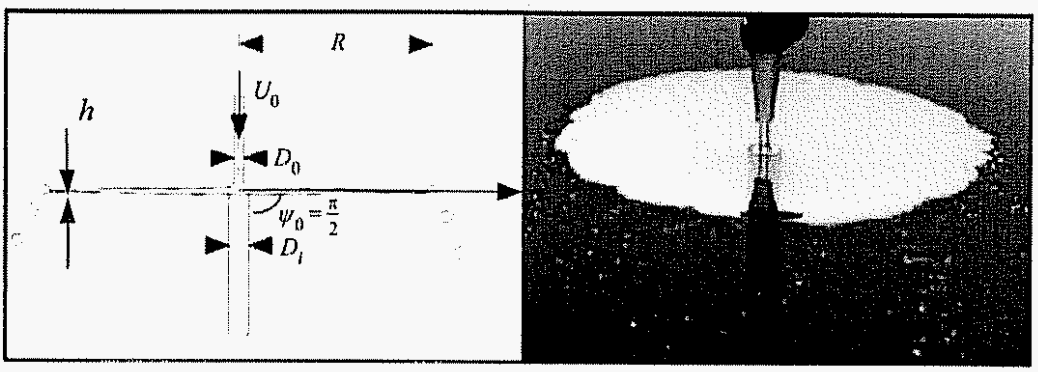

Figure 6. Sheet formation and geometry (Clanet & Villermaux).

As the radius of the sheet increases, the sheet thins as described by:

$$\frac{R}{D_0} \approx \frac{We}{16} \tag{4}$$

which becomes

$$\frac{h}{D_0} \approx \frac{10^{-1}}{We} \tag{5}$$

For a Weber number of 1000, h/D_0 is approximately 10^{-2}. For D_0 equal to one centimeter, the droplet size, h, becomes approximately 100 μm. Figure 7 shows photographs of sheet break-up with increasing Weber number from approximately 150 in frame (a) to $We \approx 1000$ in the last frame, frame (j).

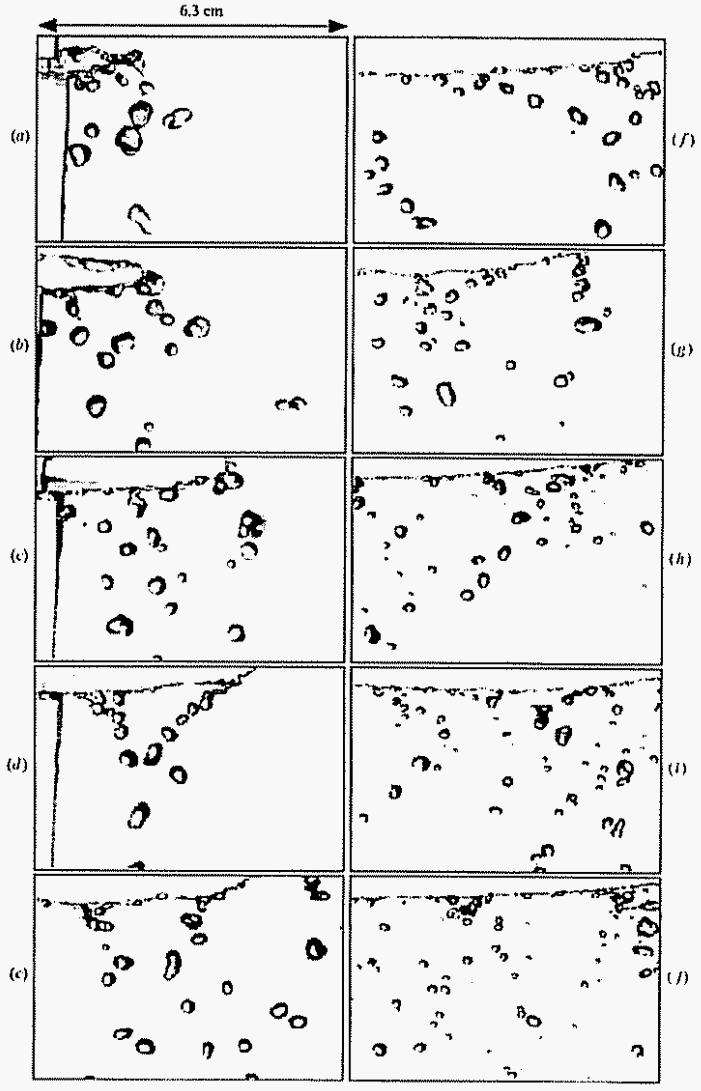

Figure 7. Sheet break-up. Increasing Weber number from 150 to 1000 from Clanet & Villermaux 2002.

When the Weber exceeds 1000, waves are much more in evidence. The droplets in the break-up can be described by:

$$\frac{D_{droplet}}{D_0} \approx \frac{1}{\left(\rho_{air}/\rho_{liq}\right)^{2/3}} \frac{1}{We} \approx \frac{90}{We} \qquad (6)$$

The sheet appears as below.

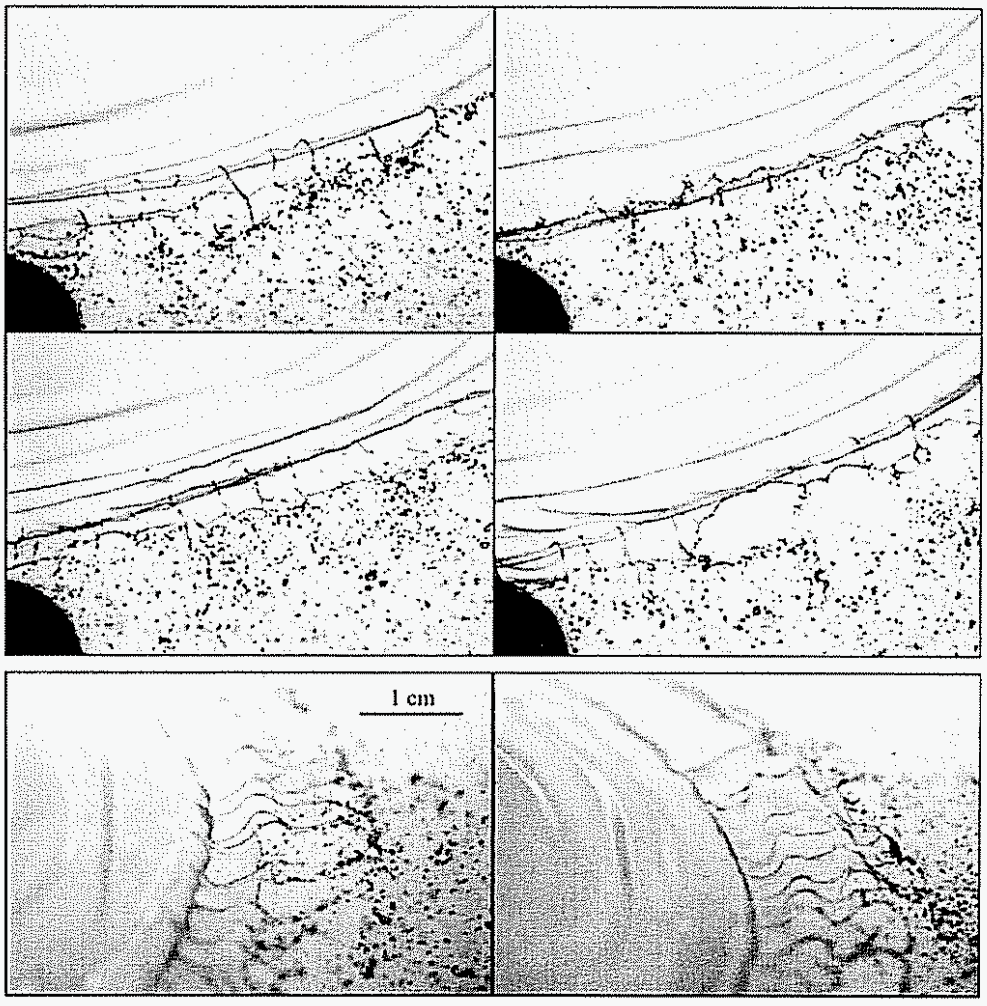

Figure 8. Flapping sheet at large Weber number from Villermaux & Clanet 2002.

The Tire Geometry in the Laboratory

In order to correctly model a tire rolling over a wet road, the physics of the tire patch must be understood. There are two reference frames applicable, as shown in Figure .

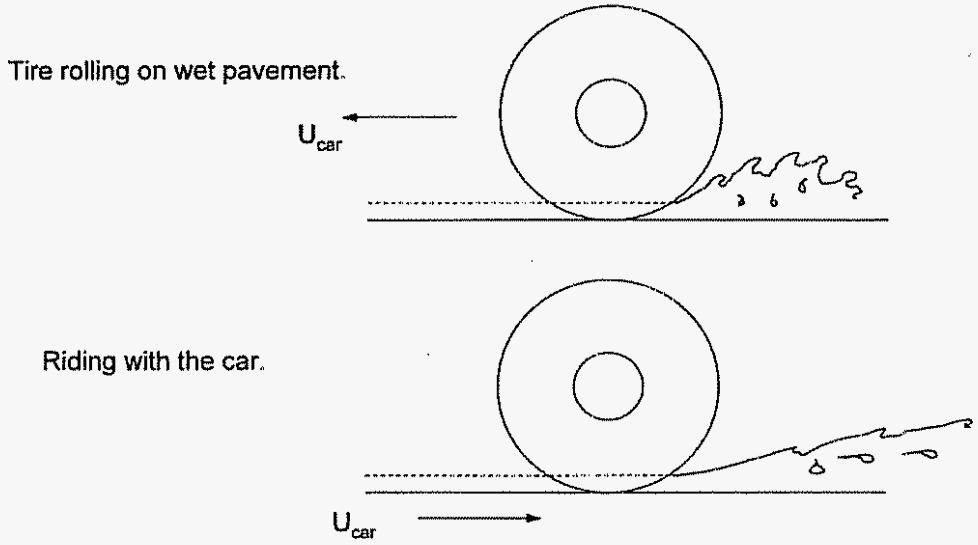

Figure 9. Two reference frames for tire rolling over a wet ground.

In the first reference frame, an observer watches a tire rolling along wet pavement. In this scenario, the tire moves at velocity U_{car} over stationary water. In the second reference frame, the observer rides with the car and sees water coming at the tire with velocity U_{car}. Now, using the principle of symmetry, the tire can be flipped so that a second tire represents the road, as shown in Figure 10. This principle of symmetry and a reference frame riding with the car is used to model the tire/water interaction in the laboratory.

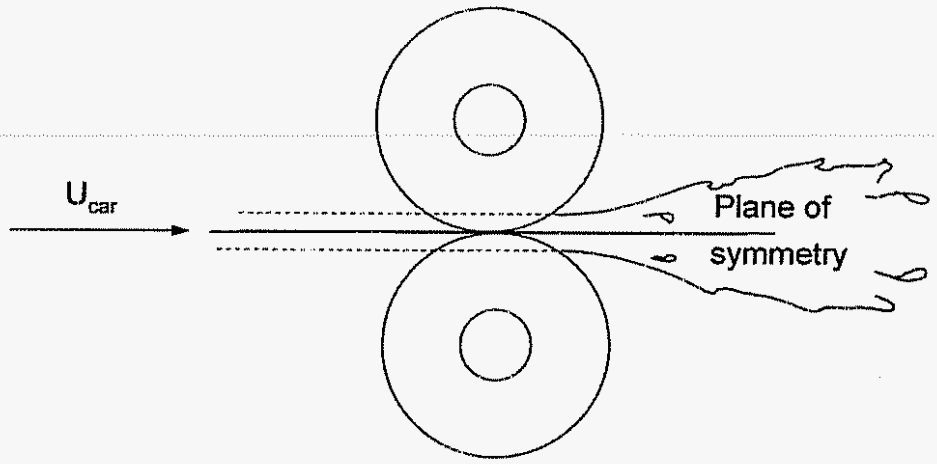

Figure 10. Using principle of symmetry, a second tire represents the road.

MATERIALS AND METHODS

Tire Spray Simulator

The experimental setup for capturing the formation of spray focuses on four main areas: the tire patch, the water jet, the imaging, and the lighting. The Tire Spray Simulator (TSS) machine met requirements for each of these four areas, as shown in Figure 11.

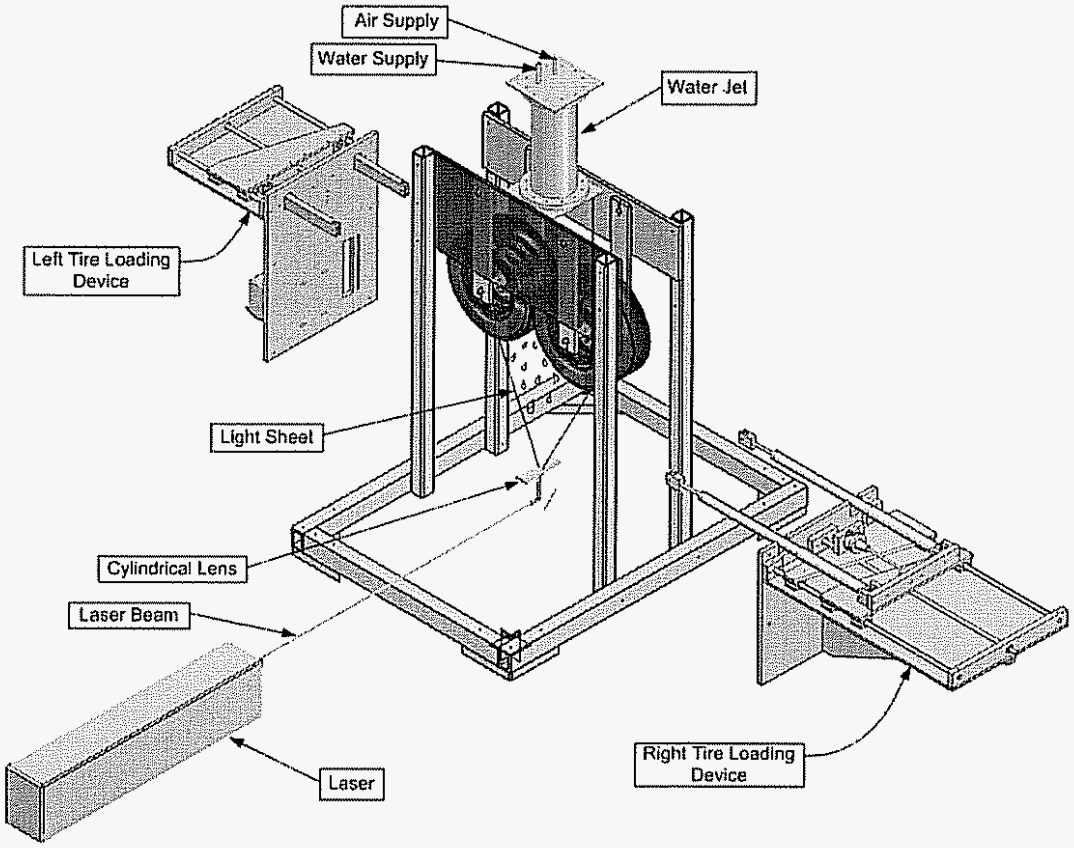

Figure 11. The Tire Spray Simulator.

The moving tire patch is created using one tire having a smooth surface to represent the road and another tire with a circumferential groove to simulate the tread of a car tire. The tire patch is formed when the two tires are pressed and held together using the left/right tire loading devices. Two shock/spring dampeners, controlled by two stepper motors, regulate the force on the tire patch (contact patch). A 0-250 lbs Sensotech load cell loaded in-line with the dampeners measures this force. A 3-hp Leeson DC electric motor controls the rotation velocity of the tire to the left—the smooth tire in the present case. The second tire is driven by contact at the tire patch. A gear ratio of 30:21 is selected to properly step down the rotation of the tire. A 50 gage chain and chain tensioner transfers rotational motion from the motor to the tires. Tires of varying grooves or tread patterns can be used to simulate different conditions.

In order to properly model the water coming into the tire patch, a jet of water traveling at the peripheral speed of the tire must be established. This is, by far the most difficult task. The water is stored in a pressurized stainless steel canister. Water and the air for pressurization enter at the top of the canister. At the bottom of the canister, a solenoid valve controls the water output to a thin-walled brass tube. The water jet issues from the end of the brass tube

Future tests will utilize a more sophisticated water delivery system for better control of the water supply, as shown in Figure 12. This system will use the previously mentioned pressurized canister, but the opening mechanism is different. A high-speed stepper motor drives a lead screw attached to a sliding gate at the bottom of the canister. A Teflon-sheet wraps around the gate and actually provides a rolling contact with the seal at the exit nozzle. In operation, the stepper motor moves the sliding gate and the Teflon sheet rolls away from the exit nozzle. This process takes between 10 and 20 milliseconds. The gate remains open and water flows from the canister for a specified time, and the gate is closed. Nozzles of different sizes and shapes can easily be interchanged to allow tire treads of different sizes and geometries to be explored.

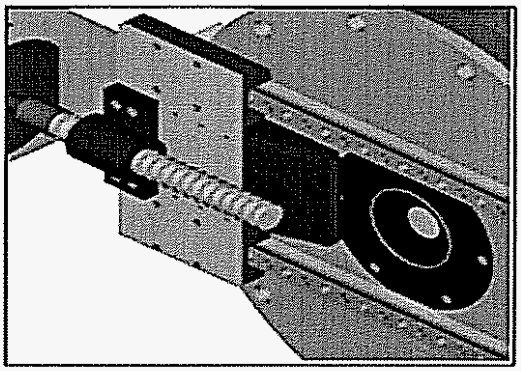

Bottom view of water jet, showing sliding wedge-shaped gate with leadscrew. A teflon sheet wraps around the wedge, sliding over the rounded nose as the gate is opened. The circular cutout receives nozzle inserts, allowing the nozzle shape to be easily changed.

Figure 12. stepper-motor-controlled slider for precise water delivery.

Imaging

Image capture of the tire spray utilizes a high-speed digital video camera from Integrated Design Tools, Inc. (IDT). The camera has a resolution of 1260×1024 pixels. The camera has on-board memory of one gigabyte, or about 1000 images. On-board memory is expandable to 8 gigabytes. Framing rate and exposure time can be controlled independently. The smallest exposure time is approximately 1 micro-second (μs). The maximum framing rate is dependent upon the size of the image. The camera limit represents a maximum transfer rate of about 7 gigabits/second for 10-bit pixel information.

Two types of lighting are presently used to visualize the flow. In backlighting, a single 1000 W lamp and two 650 W lamps light a piece of frosted glass—either single or double sided—placed behind the tires; this method provides a silhouetted droplet

image. When backlighting, typical camera settings are: 2-4 μs exposure time, framing rate of approximately 1600-1700 fps, and a field of view of 250 mm x 70 mm. These settings produced images suitable for time history and digital particle image velocimetry (DPIV).

Both backlighting and a laser sheet are used to light the region of interest because they provided different views of the flow. Backlighting integrates all the water droplets between the frosted glass and the camera, although some of these features may be intentionally out of focus. In contrast, the laser sheet illuminates the features in a thin sheet of light—usually 2-3 mm in thickness. In the cases shown here, the sheet is perpendicular to the plane of tire rotation, and passes through the central symmetry plane of the tire. In principle, the light sheet can be moved laterally across the face of the tires (from sidewall to sidewall), and it can be broadened beyond the usual 2-3 mm.

We are presently using a Quantel Scientific, twin-tube Yag laser capable of 150 mJoules per pulse. The lasing time is approximately 5-10 nano-seconds, and the repetition rate is 10 Hz (pulses per second). The laser can be operated with one of the two tubes firing at 10 Hz, or with both tubes firing (10 Hz) with a prescribed time delay. The delayed—or double-pulse—mode is necessary for laser digital particle image velocimetry (DPIV).

RESULTS – *How do "jets" and "sheets" fit the tire spray picture?*

Before regarding images from the experiment, the previously mentioned characteristics of jets, sheets and droplet formation should be related to the geometry of the tires. Figure 13 shows the experimental tire orientation a second time, and defines three cross-planes (A, B and C) at various distances downstream from the tire patch.

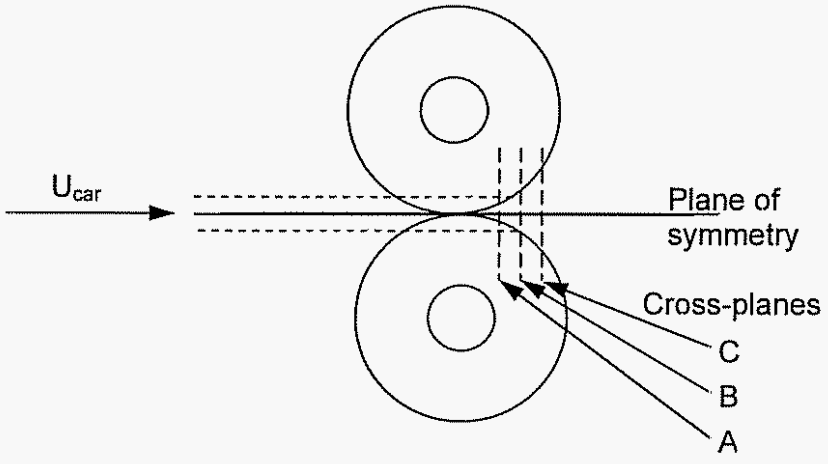

Figure 13. Tire orientation with three cross-planes A, B and C.

For the sake of simplicity through symmetry, let both tires have the circumferential groove. Figure 14 shows what might be expected of the fluid at each cross-plane as it exits the tire groove (downstream from the tire patch). At section A, just beyond the tire patch, water completely fills the tire groove. Farther downstream at section B, the tires separate and are subjected to high accelerations. In a sense, the water is left behind. Some of the water remains in near the plane of symmetry as a jet, and some water remains in the grooves. At section C, the tires have moved farther apart, the central jet is more clearly defined, and the water remaining in the groove is connected to this central jet by a thin web. With increasing tire separation the web continually thins until breaks form and droplets are produced. Disturbances also act on the surface of the jet, and eventually break the jet into droplets.

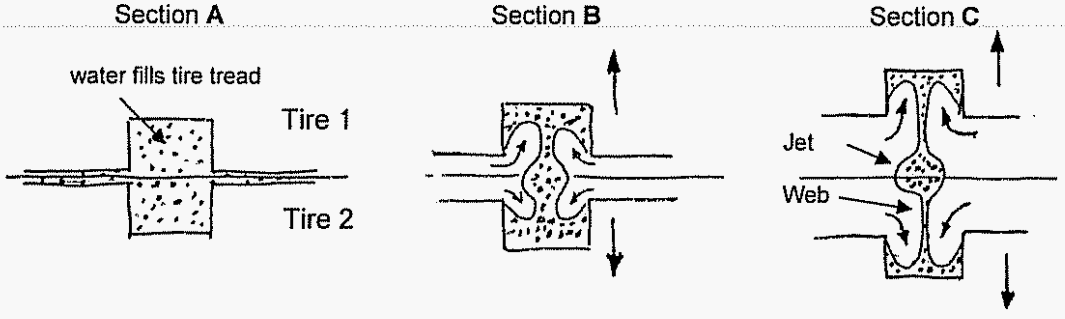

Figure 14. Expected behavior of water as it leaves the tire groove downstream from the tire patch.

A pair of sequential images using backlighting is shown in Figure 15. The two images are about 600 μs apart. During this time the features have moved approximately 5-8 mm. This experiment uses one grooved tire and one smooth tire rather than two grooved tires. One notices the lack of symmetry about a line between the two tires, but it is not so clear in the image because only one tire is shown. This is the driven tire containing the groove.

The central jet is visible in the center of the frame. As it continues to move downstream it breaks ups into droplets—presumably due to Rayleigh instability. The effect of having incomplete symmetry is evident by the upward direction of the central jet. What is additionally interesting is the large-scale wavy-structure of the jet. We have no explanation for this behavior at present, but it is a sign that the central jet is probably subjected to a shearing motion in the vertical direction.

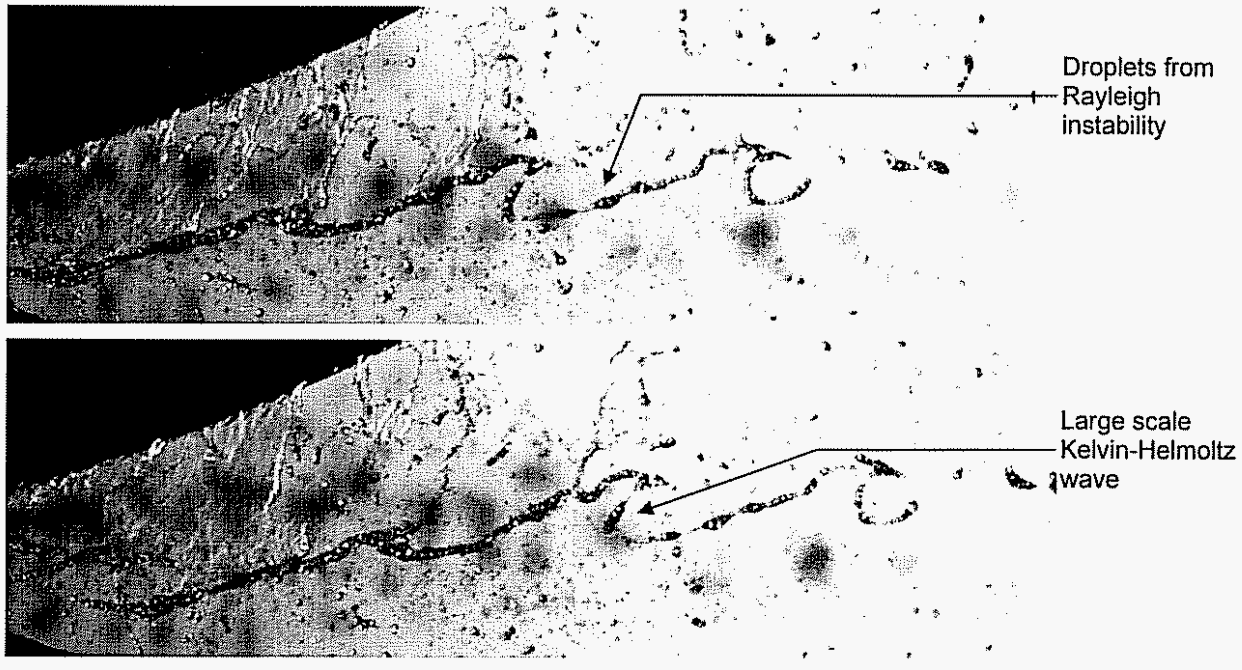

Figure 15. Consecutive backlight images showing central jet and web structure.

The backlit images shown in Figures 16 and 17 give a clearer visualization of the web evolution. The three consecutive images in Figure 16 are each displaced in time by about 600 μs. Central jet and web are both present. The web contains two features—waves which show up as highlighted features riding on the web, and actual breaks in the web which appear to occur in the thinnest portions. We did not measure local web thickness, but it is probably of the order of 300-500 μm in the central portion of Figure 16. Droplets form along the edges of the break having comparable dimension—that is droplets of the order of 200-500 μm in diameter, and considerably smaller than the droplet formed from the break-up of the central jet.

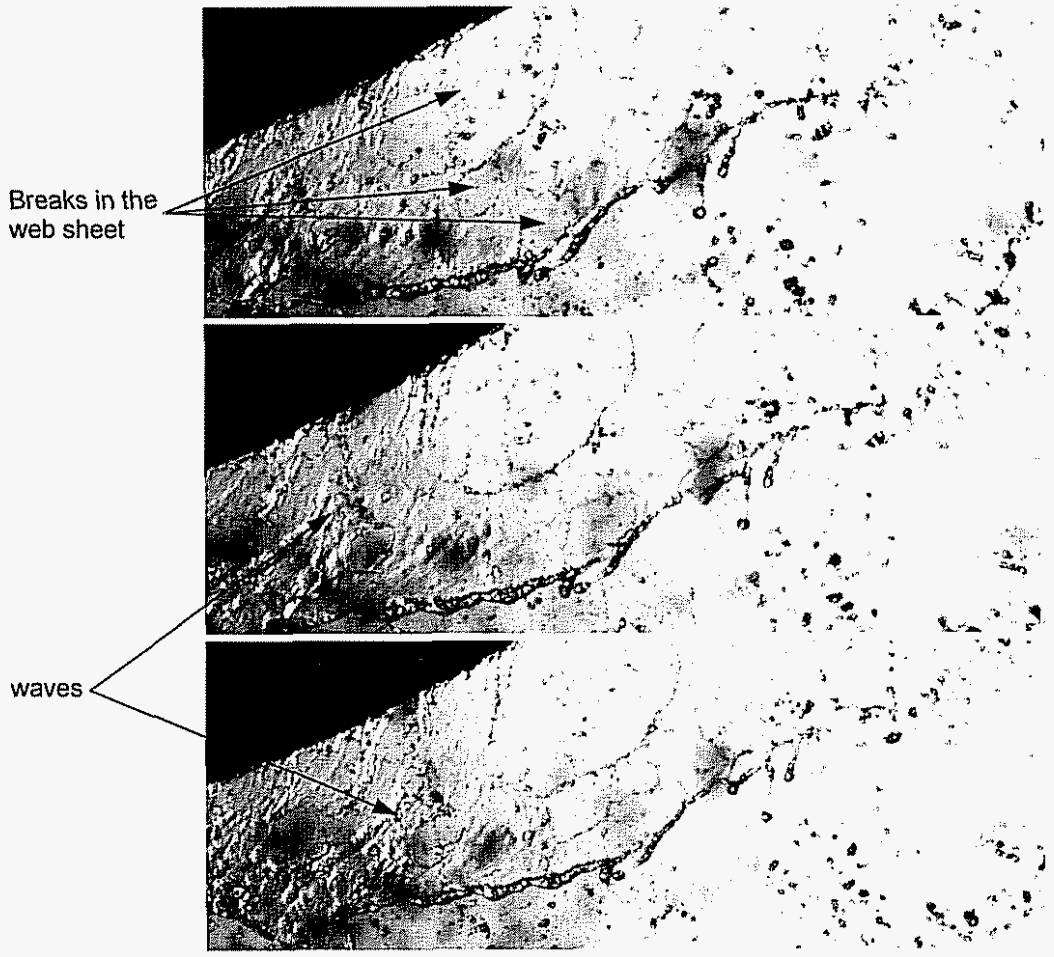

Figure 16. Consecutive backlight images showing web break-up (each frame 600 μs delay).

Figure 17 gives a wider-angle view of the spray. Both tires are observed. The lower tire is the driving, smooth tire and the upper tire is the driven, grooved tire. Lack of symmetry about a central horizontal line is evident. In the case shown, the incoming water velocity has been matched to the peripheral speed of the tires. This makes the initial Weber number of the jet larger, and the flow appears more disturbed or fractured. The central jet is seen as a nearly periodic row of (darkened) water blobs connected to the tire by ligaments. The ligaments are relatively thick regions, and may indeed be a developing wave structure. Breaks in the web appear on both sides of the central jet, but more appear on the lower side next to the smooth tire. The web probably thins near the surface of the smooth tires, because replenishment from the groove is not possible.

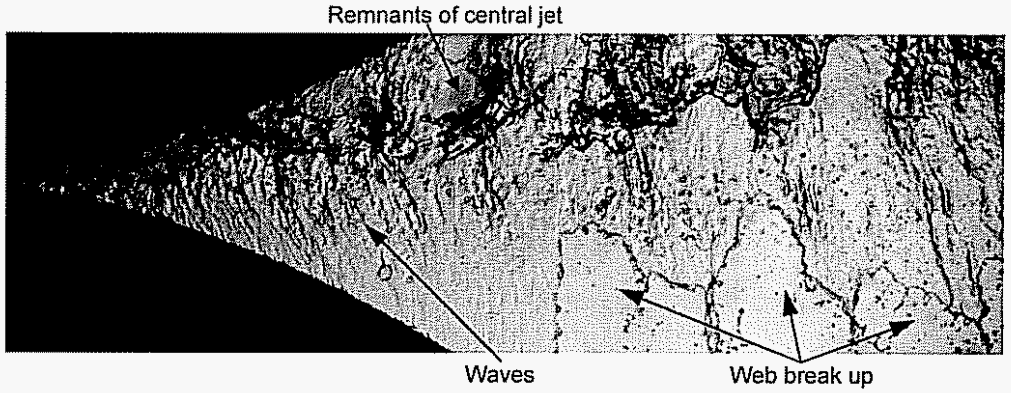

Figure 17. Spray from wider-angle perspective.

Figure 18 displays an image taken using a laser sheet. Similar to the backlight images, the web, central jet and connecting ligaments can be resolved. In addition there is a

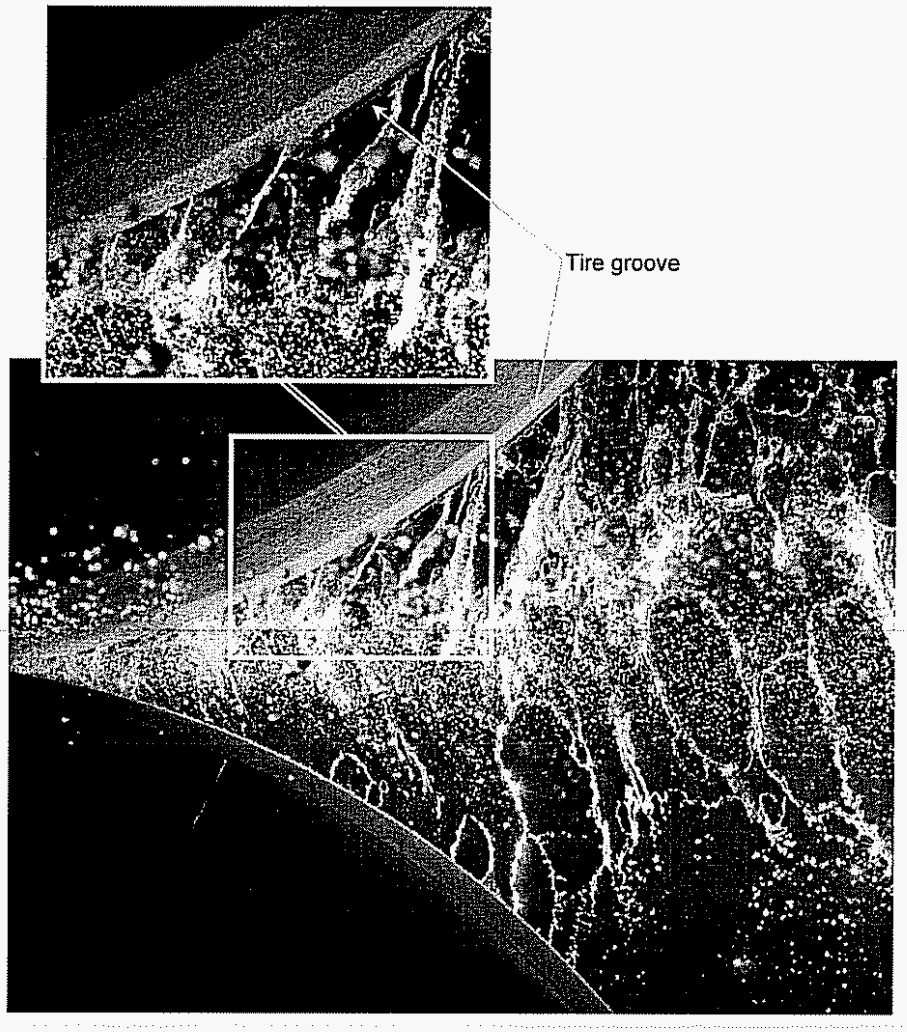

Figure 18. Spray image using a laser sheet (10 nano-second pulse time).

fine mist of extremely small droplets along the central plane in the picture. We believe these smallest droplets are a result of water forced between the tires themselves and into the contact patch. Digital particle imaging velocimetry (DPIV) is possible using images from this laser sheet technique.

CONCLUSION – *Current and future progress*

The Tire Spray Simulator (TSS) has demonstrated its usefulness in creating realistic spray. Qualitative results have been obtained using the backlight and laser sheet procedures, leading to an understanding of some the mechanisms behind the formation of jets and sheets, and of the eventual formation of droplets. The next step in analysis will be to measure droplet size and droplet velocity as a function of position within the spray field. Droplet sizes within the spray field are of first importance in themselves, but size information is also needed in order to resolve the velocity field according to size. We imagine evaluating droplet size in each image pair and filtering each image before the DPIV algorithms are applied. Local droplet size or local scale can be determined either by application of an image-segmenting technique or by application of a localized scale-filtering process such as a wavelet transform (see references 3 and 4).

Remaining modifications to the TSS include implementing a new water delivery system, and placing the experiment under computer control. Computer control will utilize LabView software.

REFERENCES

1. Clanet, C., & Villermaux, E., (2002), Life of a smooth liquid sheet, *Journal of Fluid Mechanics*, vol. 462, pp 307-340.
2. Villermaux, E., & Clanet, C., (2002), Life of a flapping liquid sheet, *Journal of Fluid Mechanics*, vol. 462, pp 341-363.
3. Sinkewitsch, V. & Browand, F.K. An Algorithm for Rapid Image Segmenting, *Experiments in Fluids*, vol. 15, pp 467-469, Oct. 1993.
4. Dallard, T. & Browand, F.K.. The Growth of Large Scales at Defect Sites in the Plane Mixing Layer, *Journal of Fluid Mechanics*, vol. 247, pp 339-368, 1993.

Final Report, Part II

Experimental Measurement of the Flow field of Heavy Trucks

DE-AC26-98EE50512

Appendix Table of Contents

Basic Frame

The first section of parts includes the basic frame and wheels.

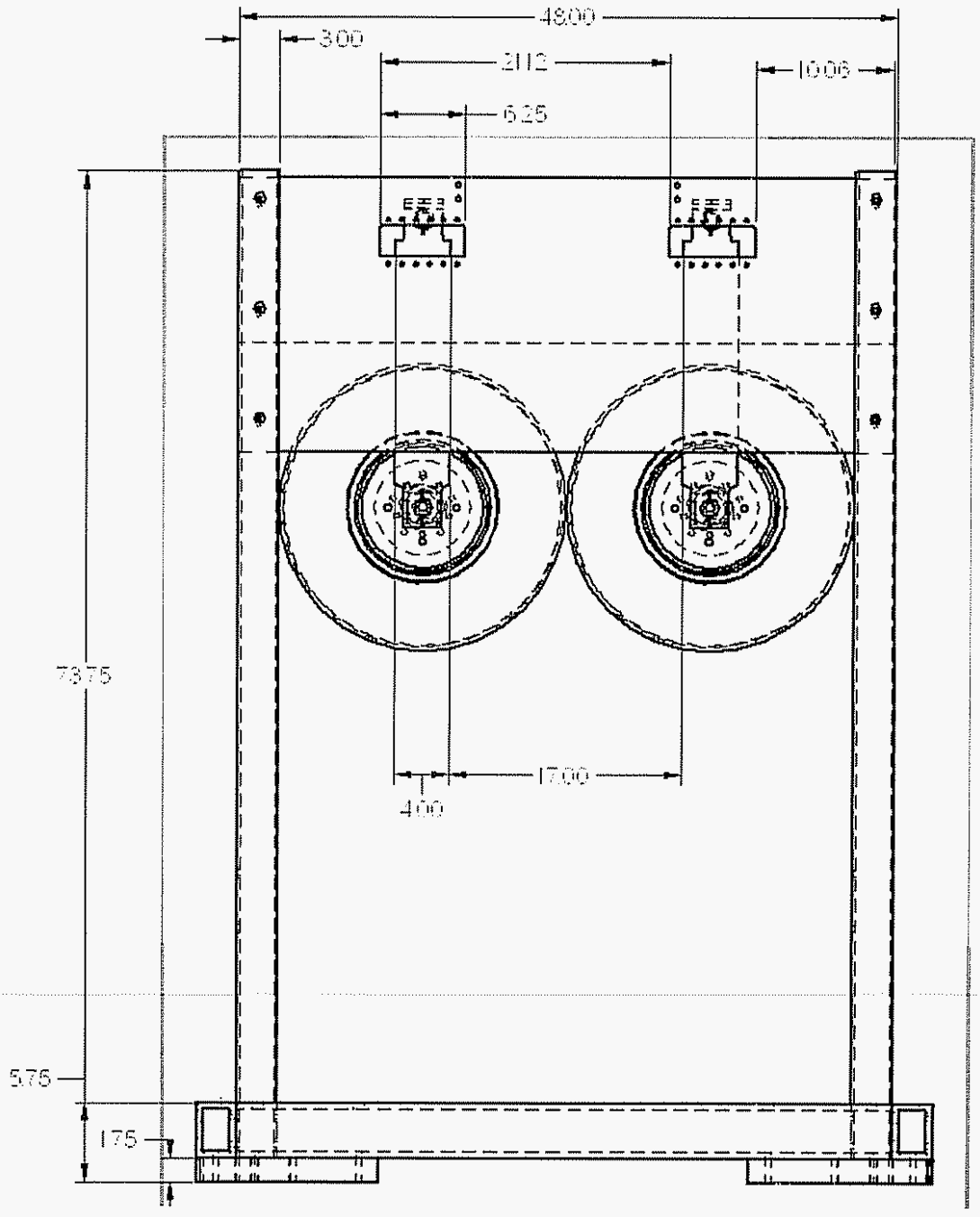

Figure 1. Tire Spray Simulator - Front View

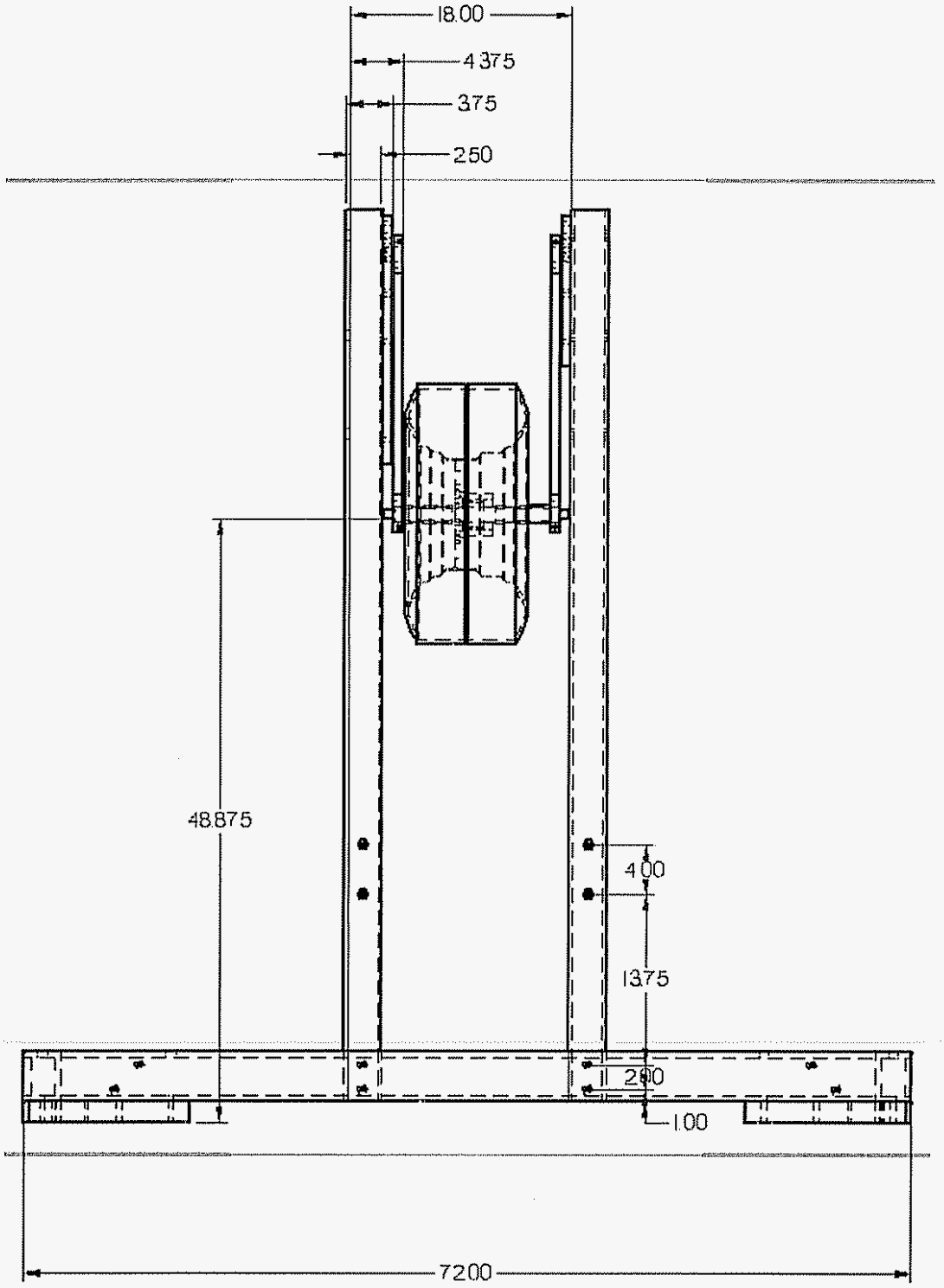

Figure 2. Tire Spray Simulator- Side View

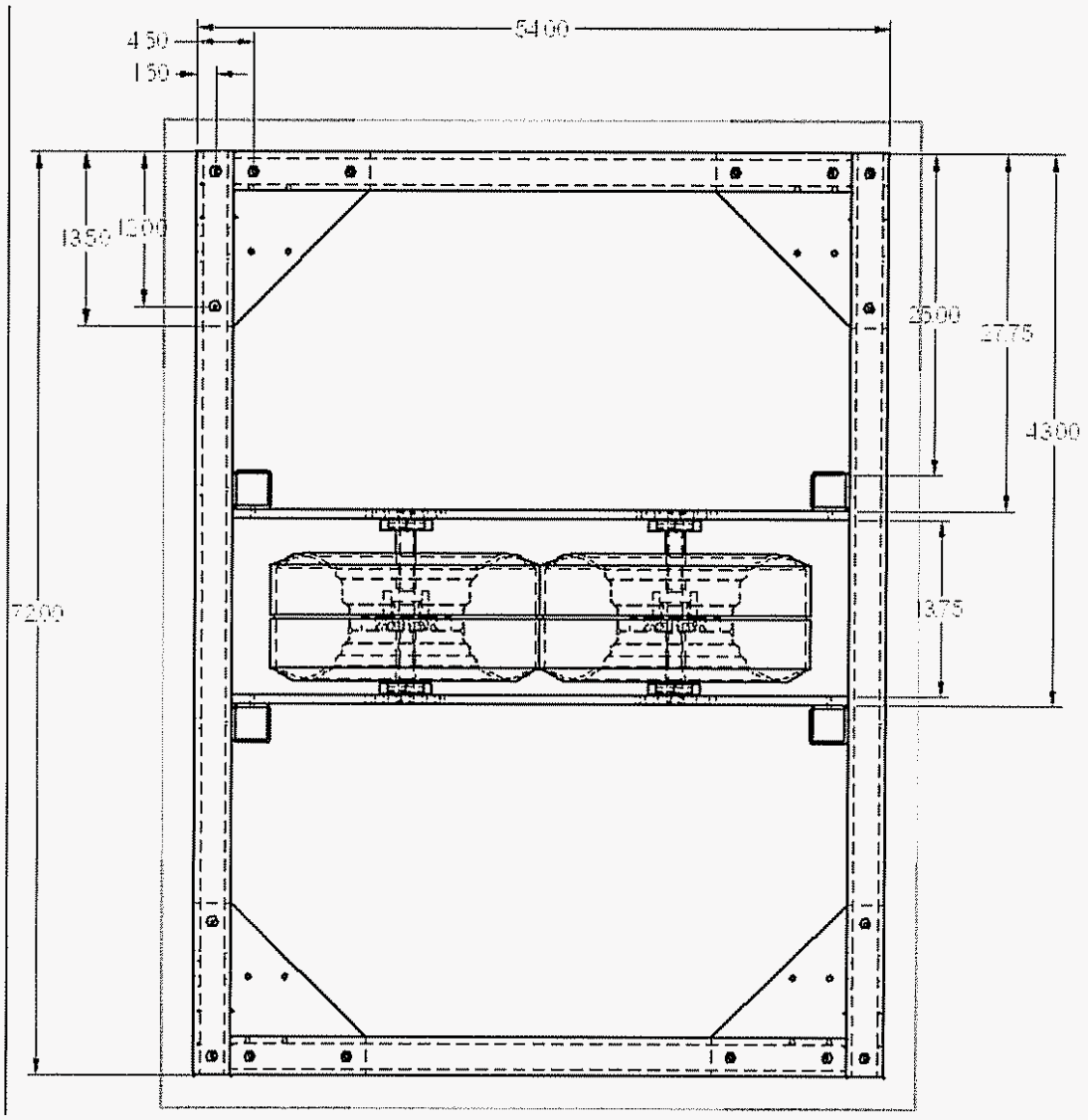

Figure 3. Tire Spray Simulator - Top View

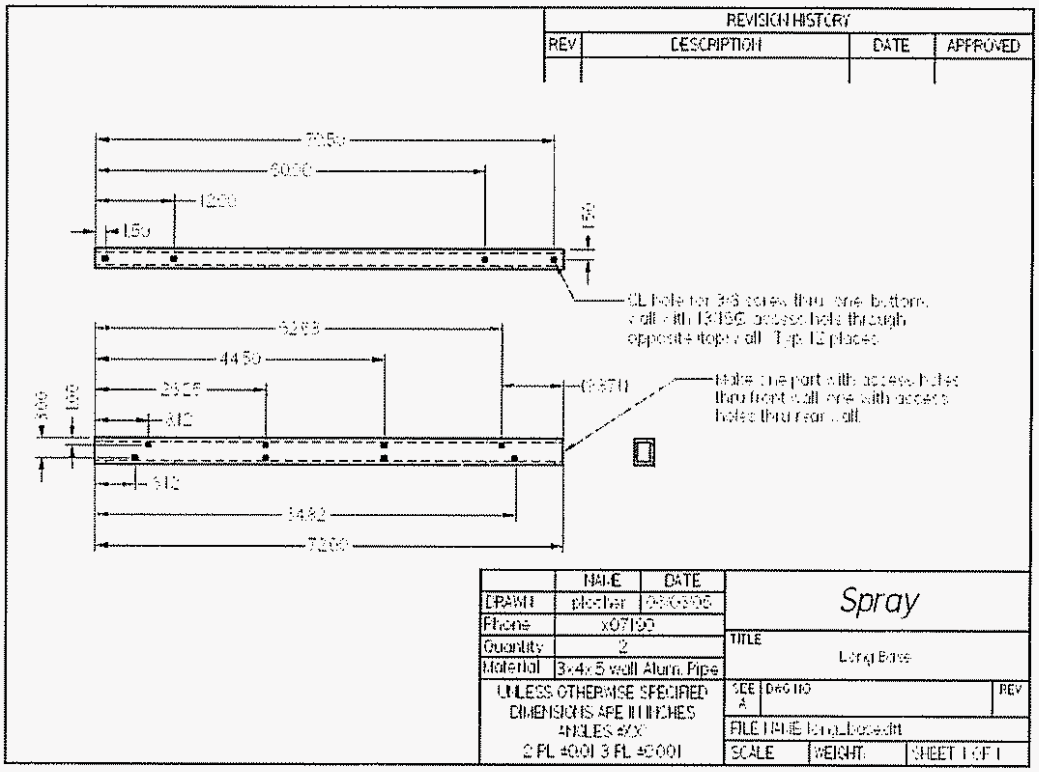

Figure 4. Base Beam Support

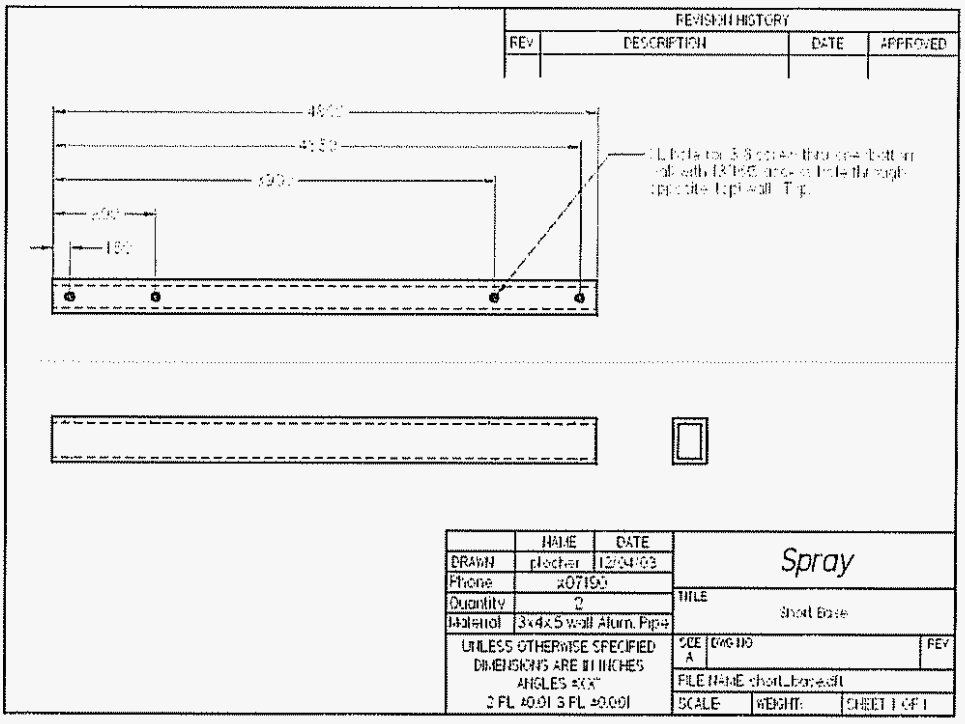

Figure 5. Short Base Beam Support

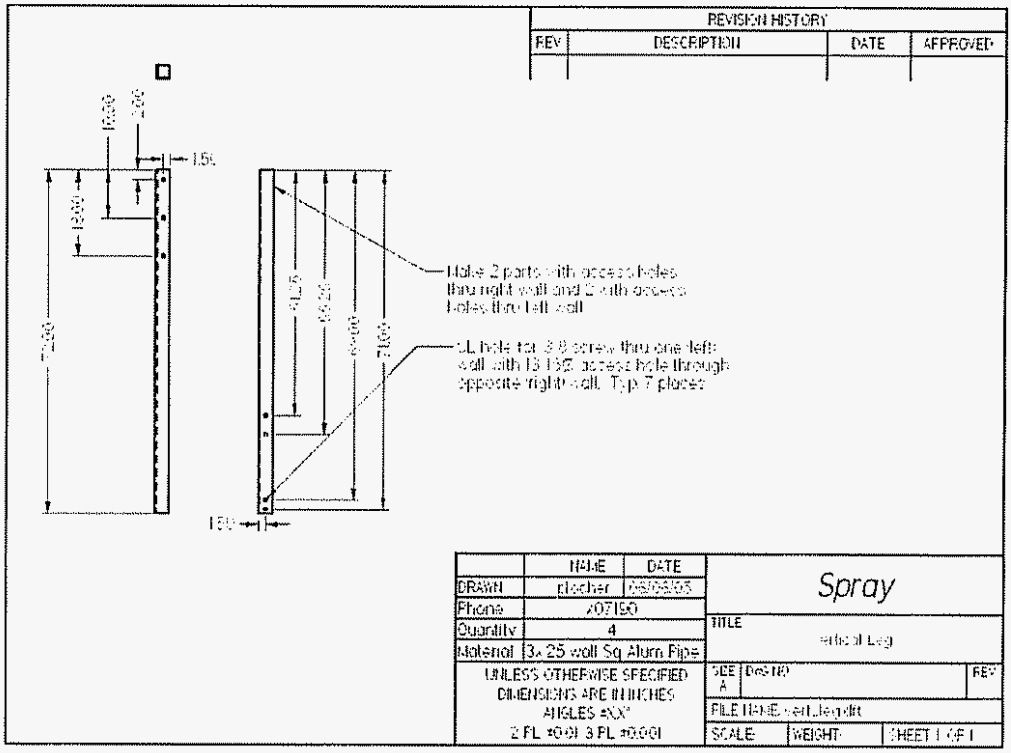

Figure 6. Vertical Support General Drawing

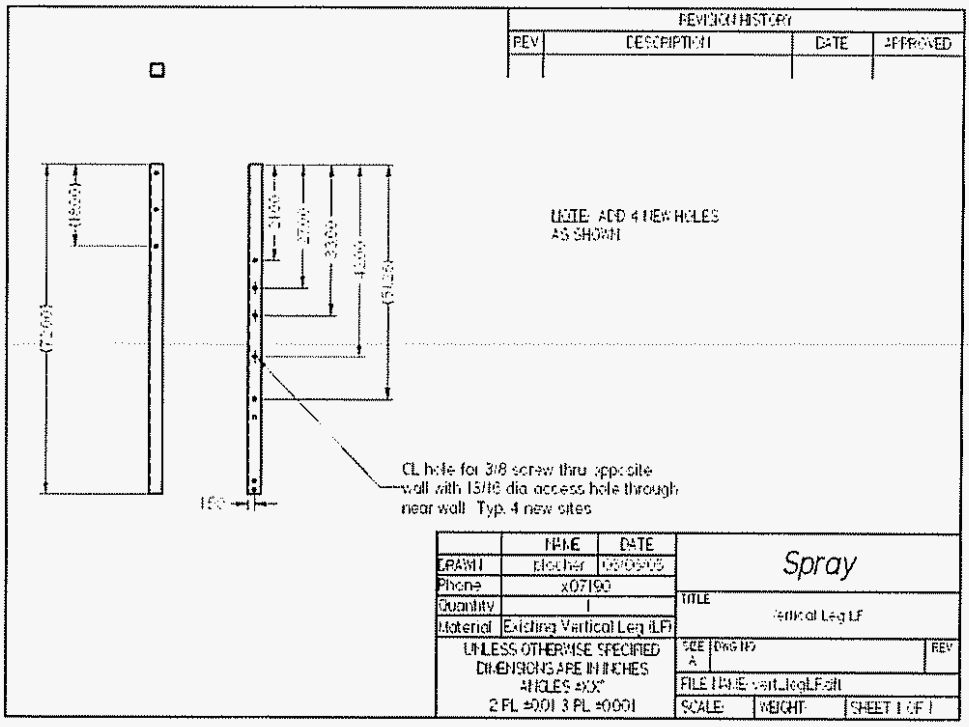

Figure 7. Vertical Support – Left Front Corner

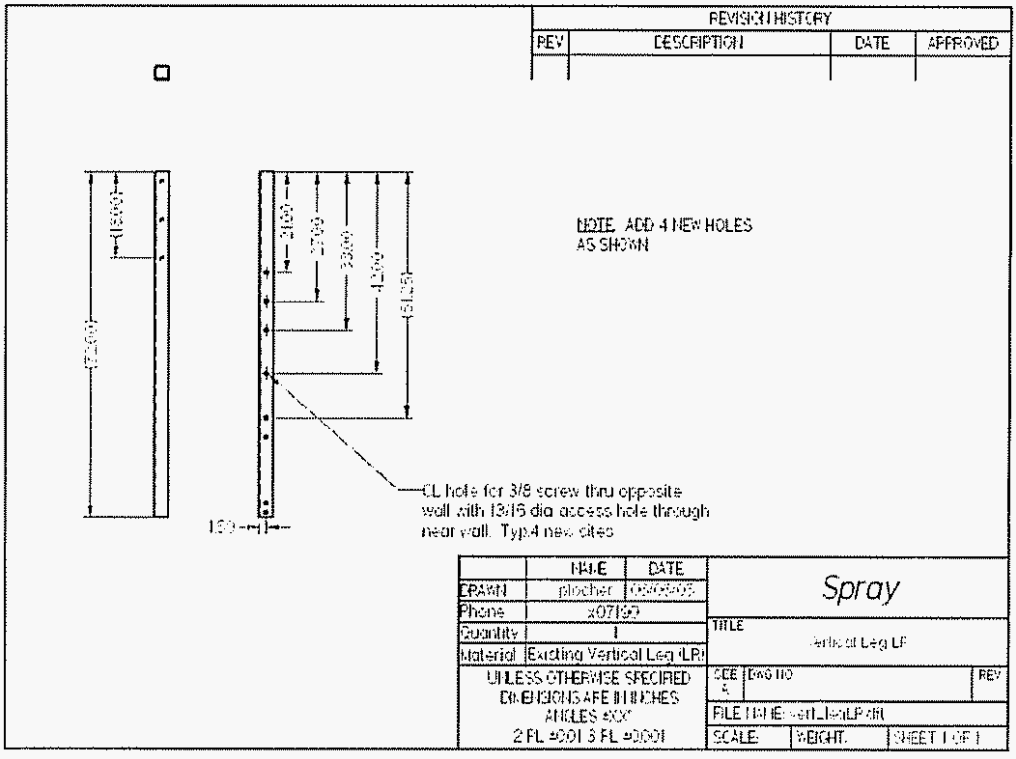

Figure 8. Vertical Support Right Front Corner

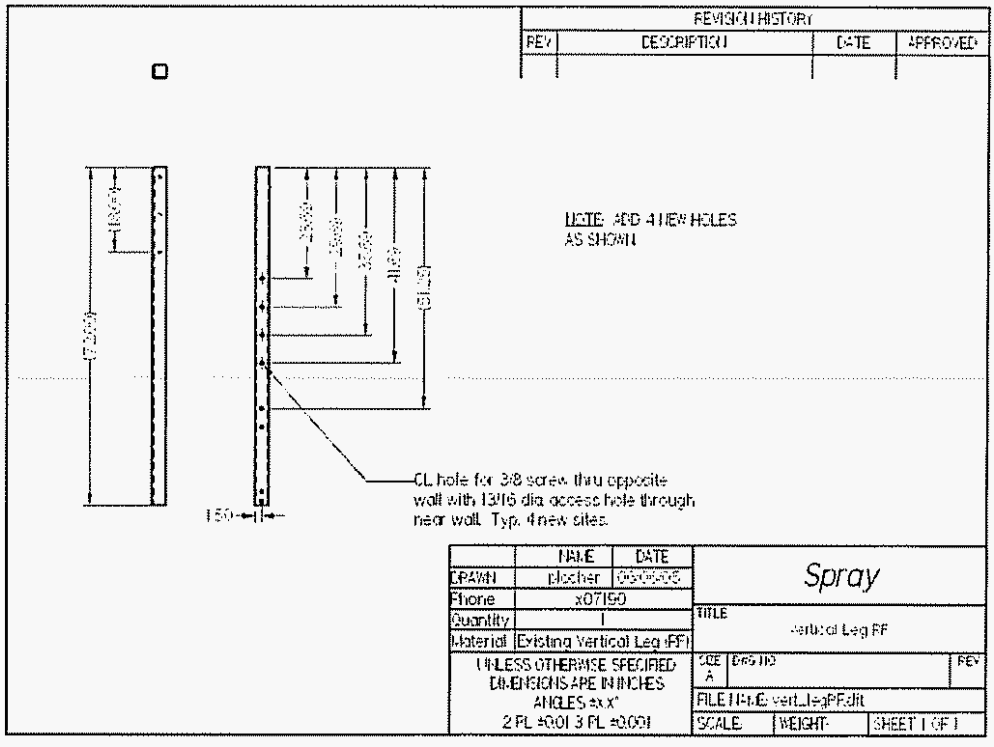

Figure 9. Vertical Support - Right Front Corner

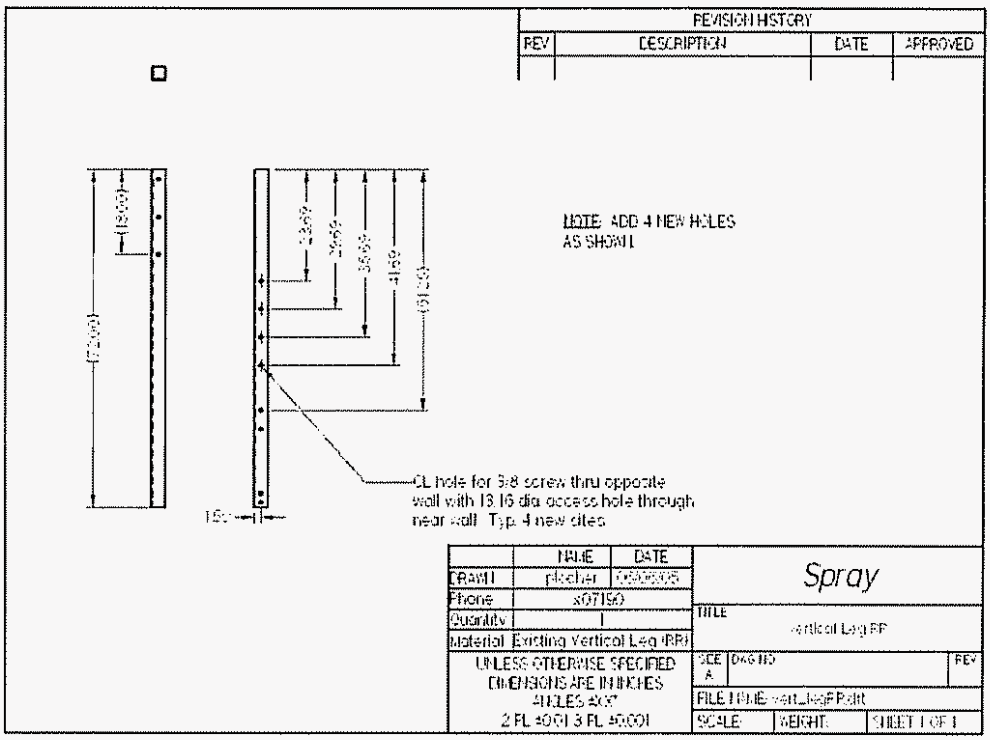

Figure 10. Vertical Support - Right Front Corner

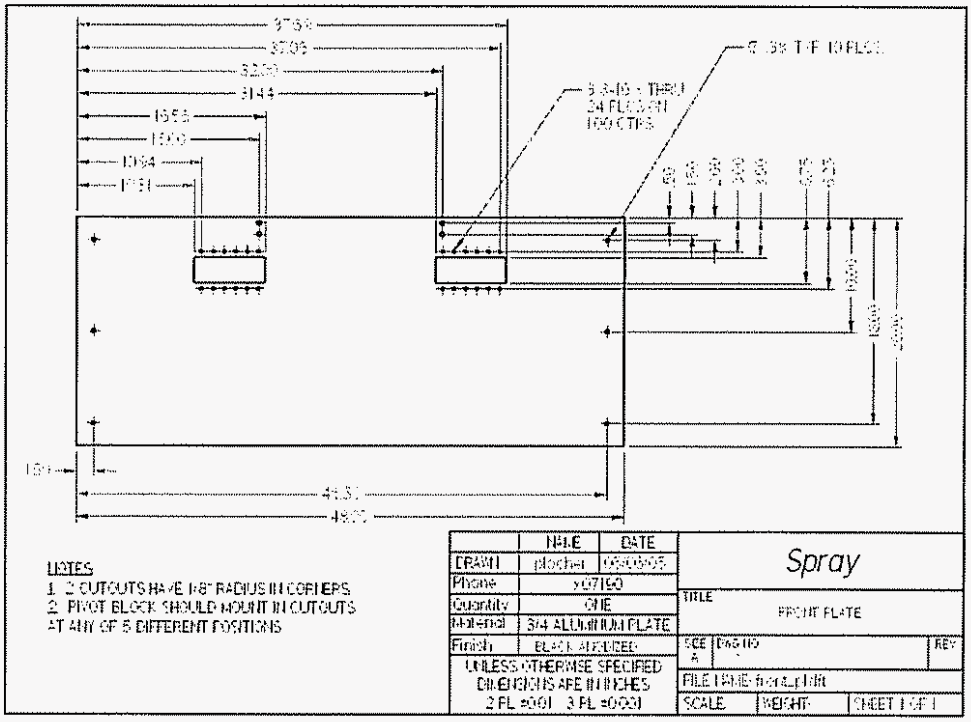

Figure 11. Front Tire Mounting Plate

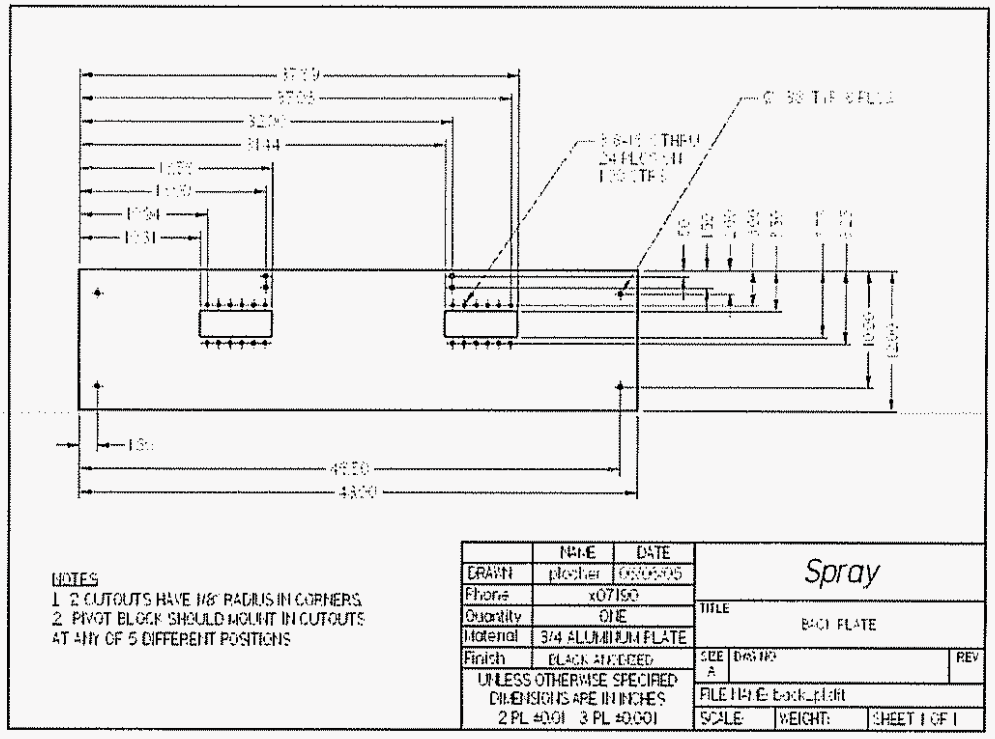

Figure 12. Rear Tire Mounting Plate

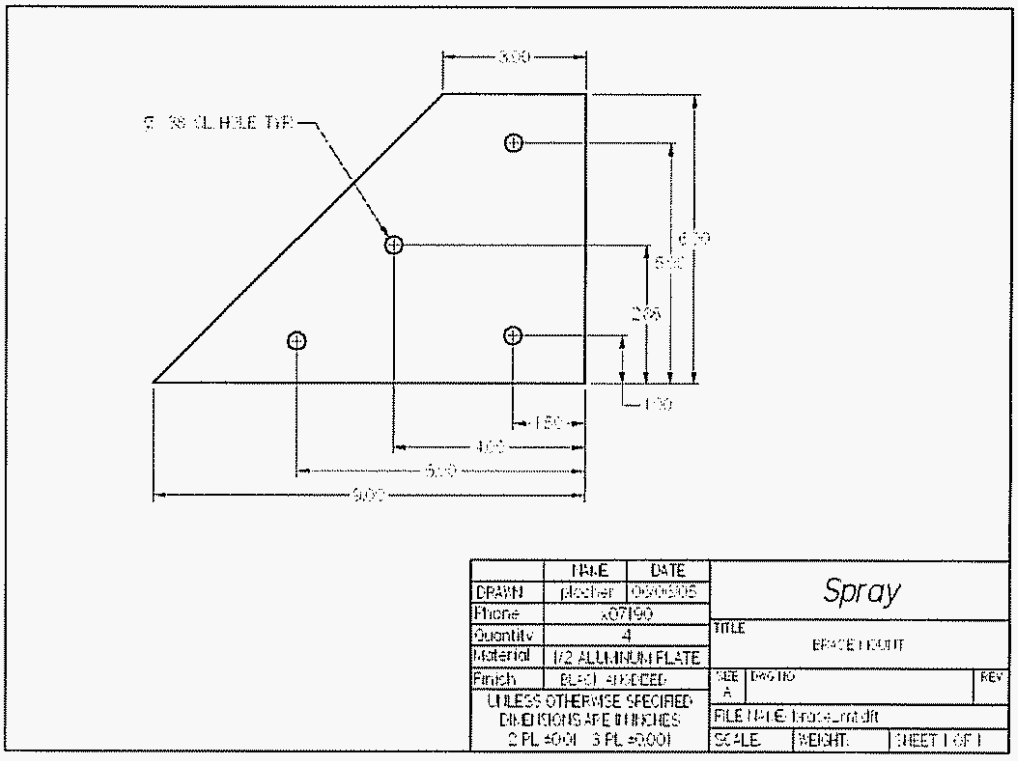

Figure 13. Bottom Brace Mount

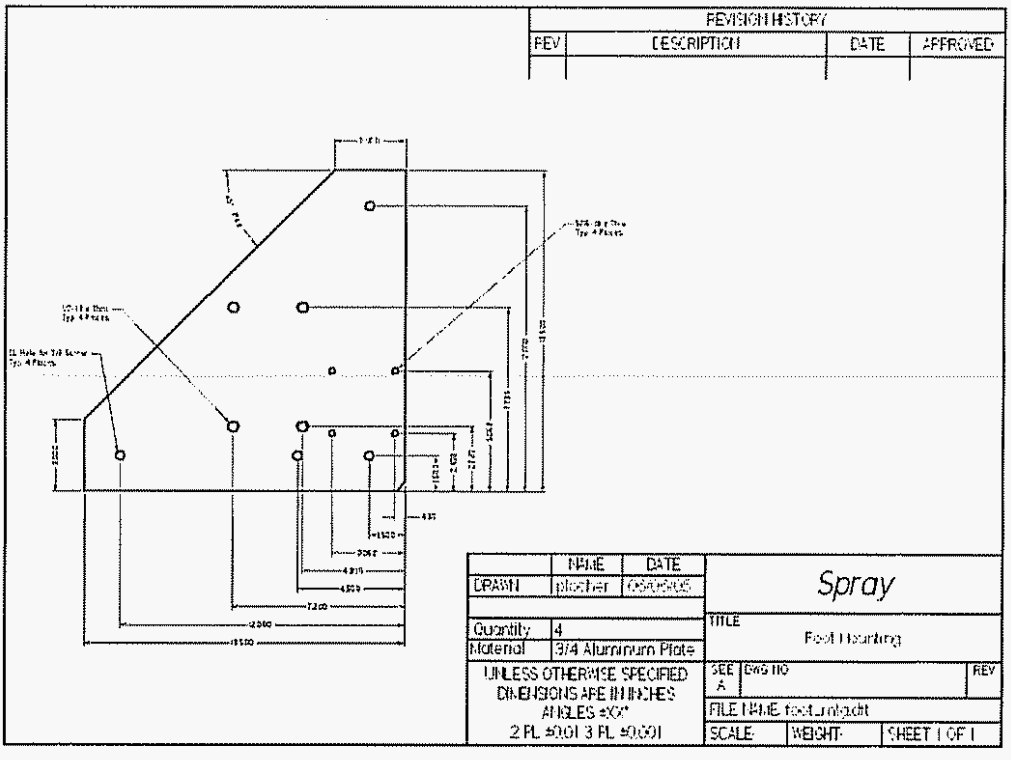

Figure 14. Bottom Foot Mount

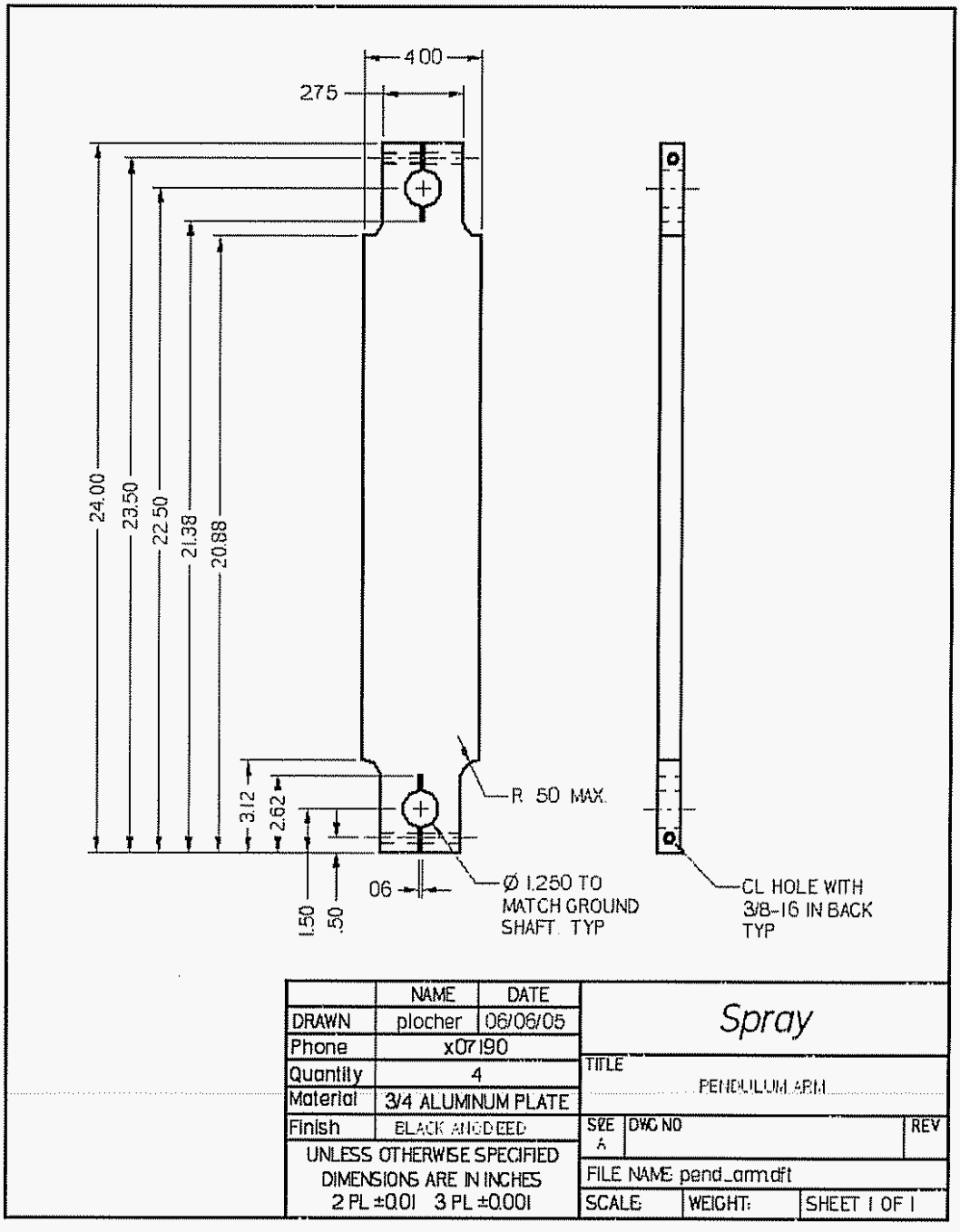

Figure 15. Pendulum Arm General Arraignment

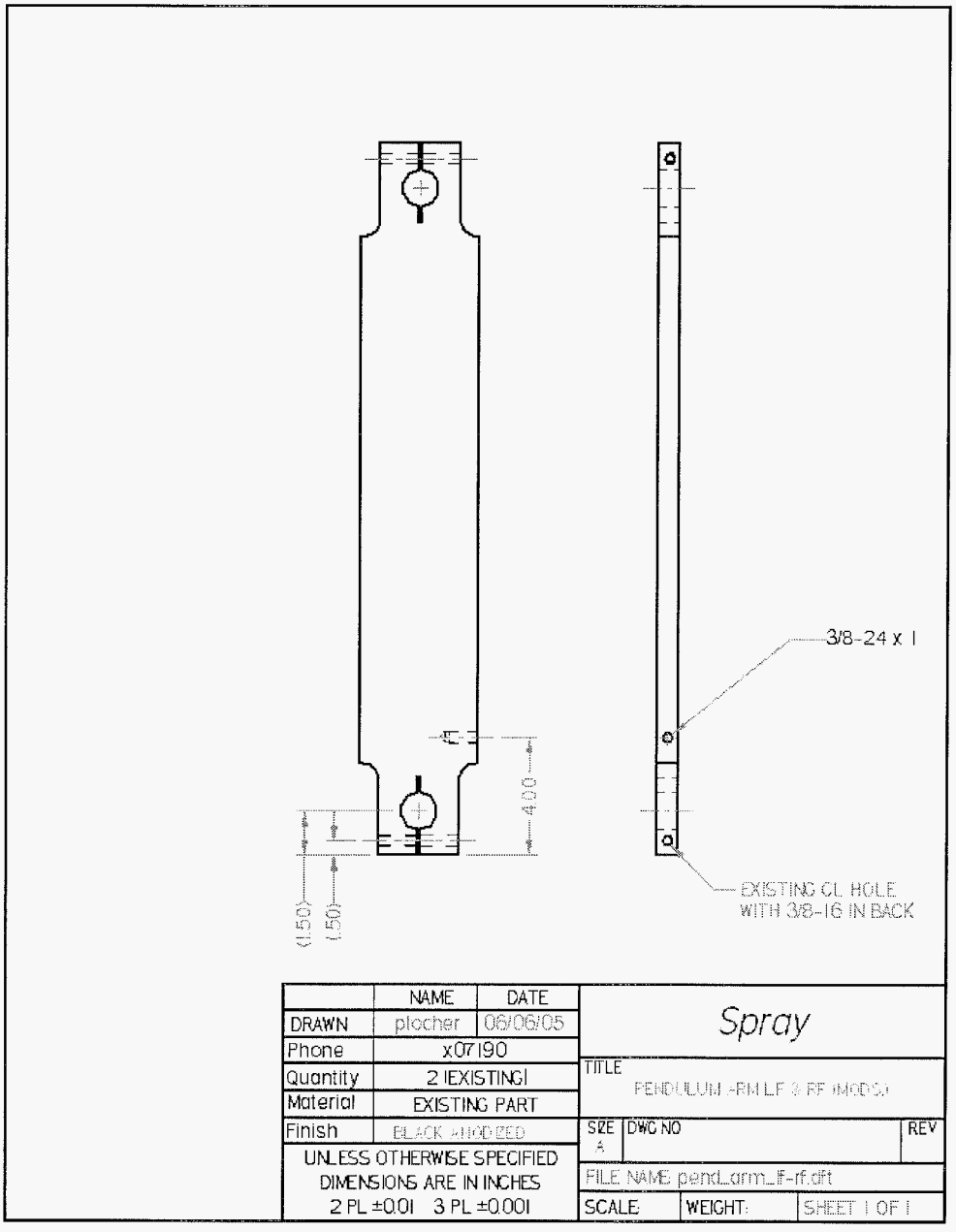

Figure 16. Pendulum Arm - Left and Right Front

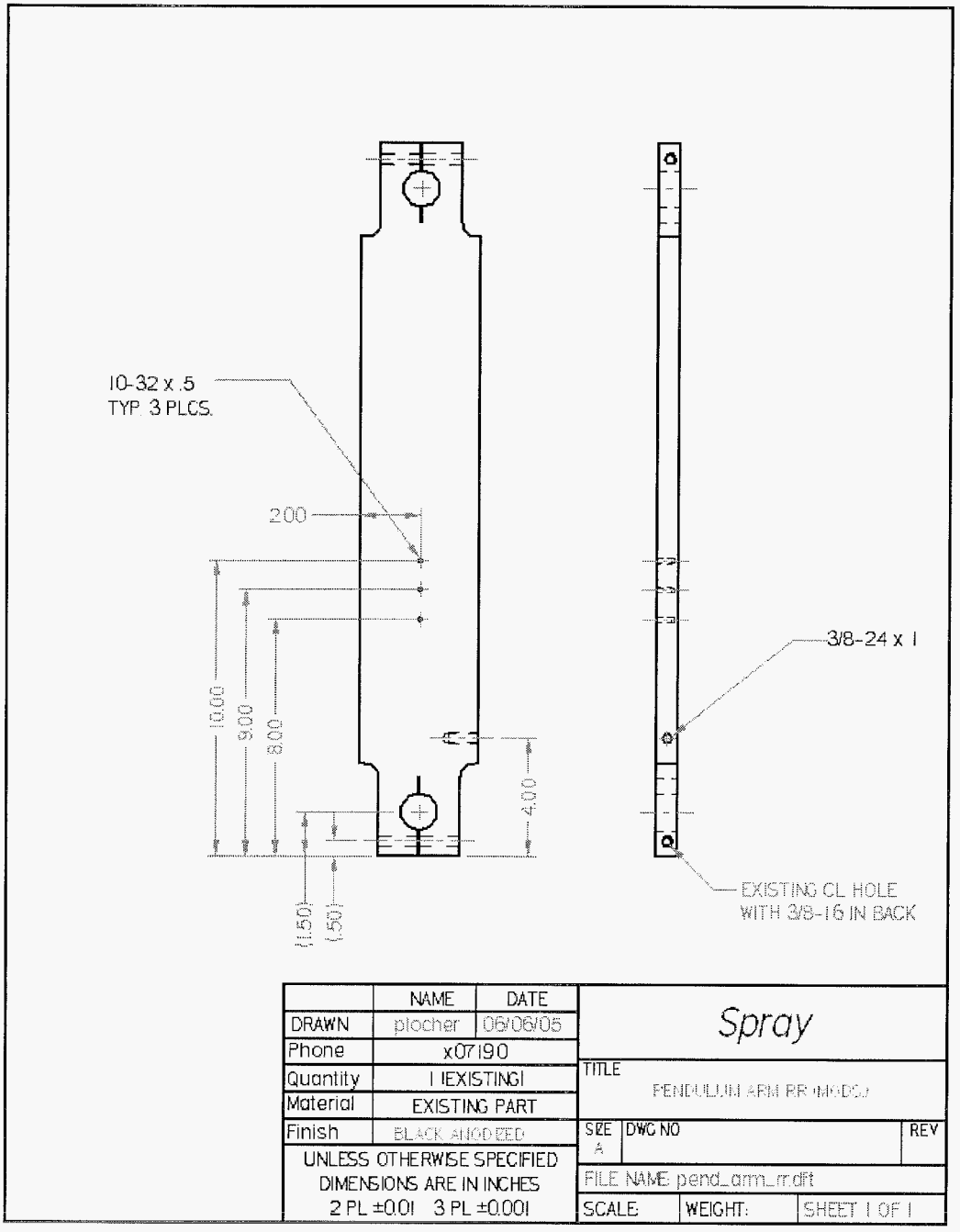

Figure 17. Pendulum Arm - Left and Right Rear

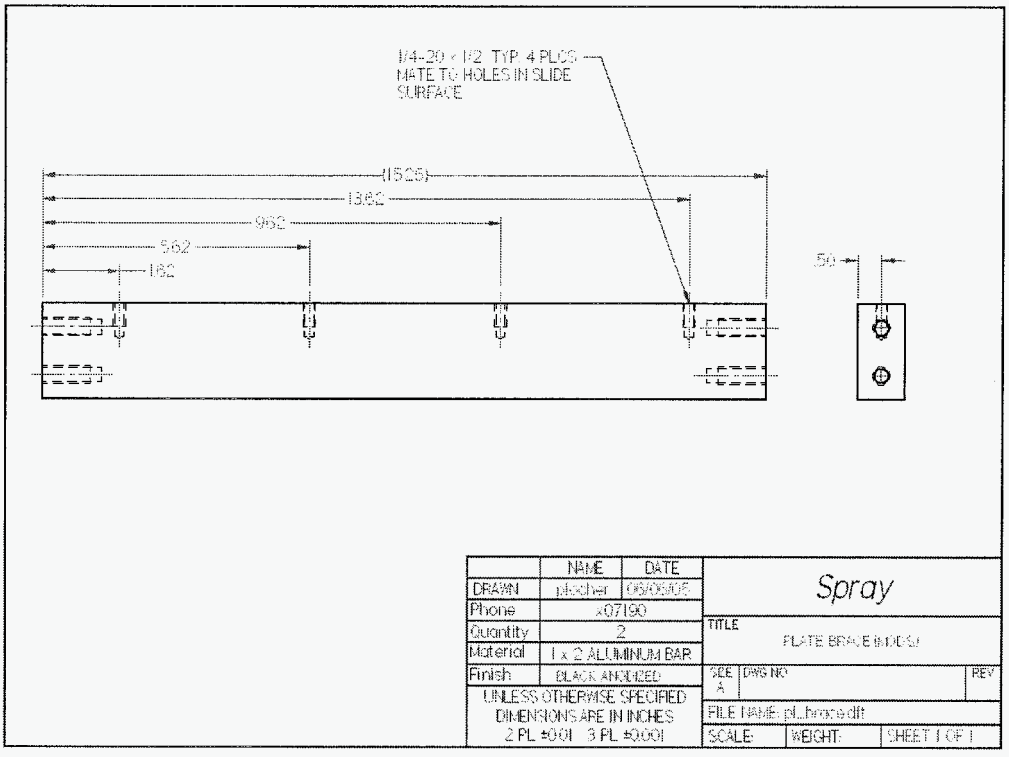

Figure 18. Plate brace

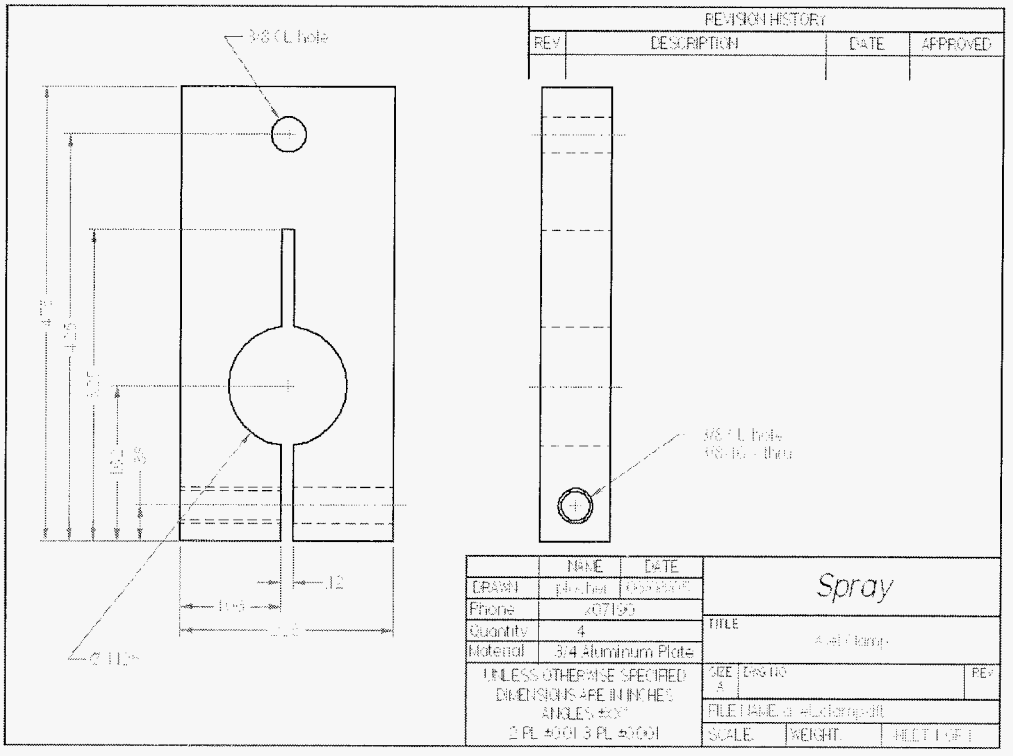

Figure 19. Axle Clamp for tire

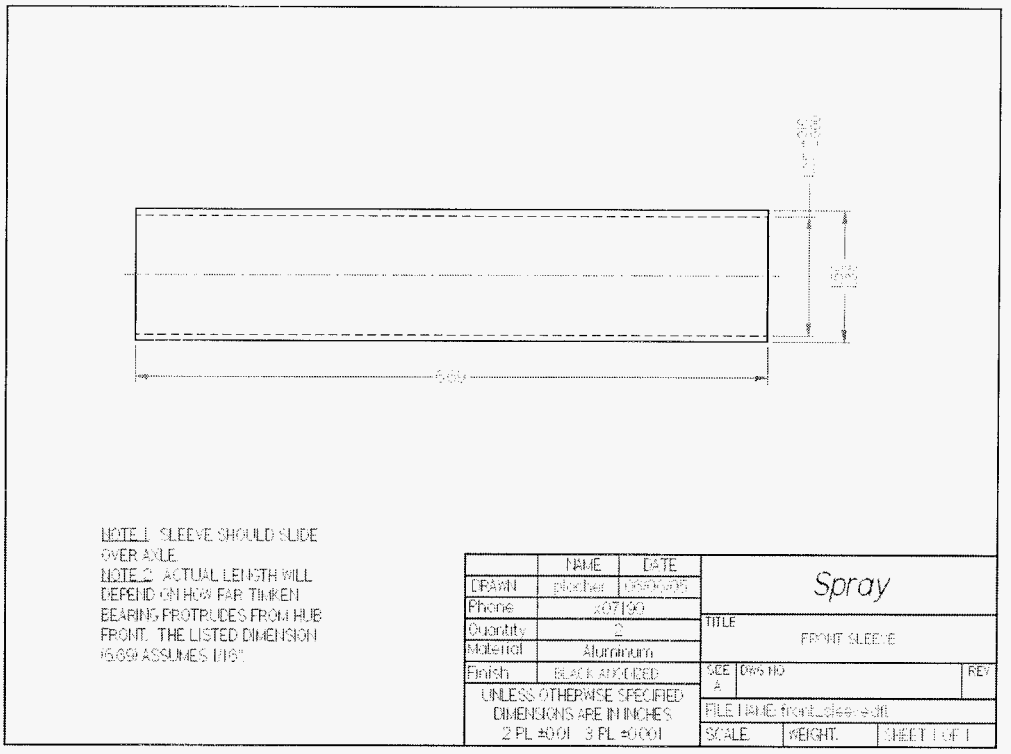

Figure 20. Sleeve for axle

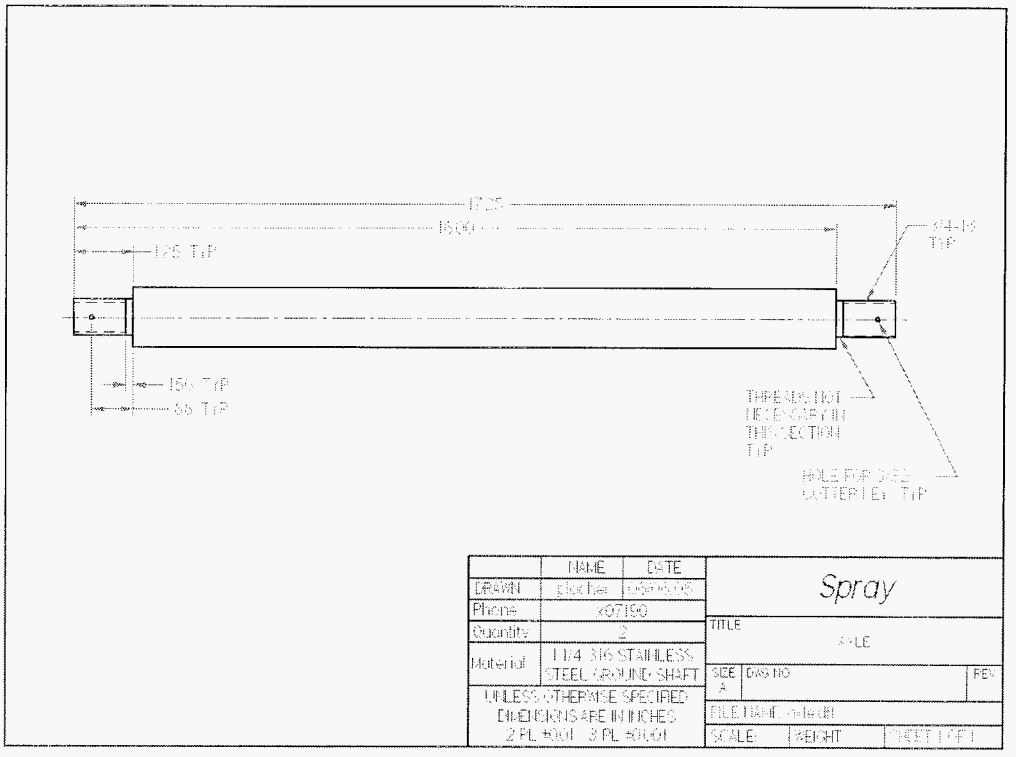

Figure 21. Tire Axle

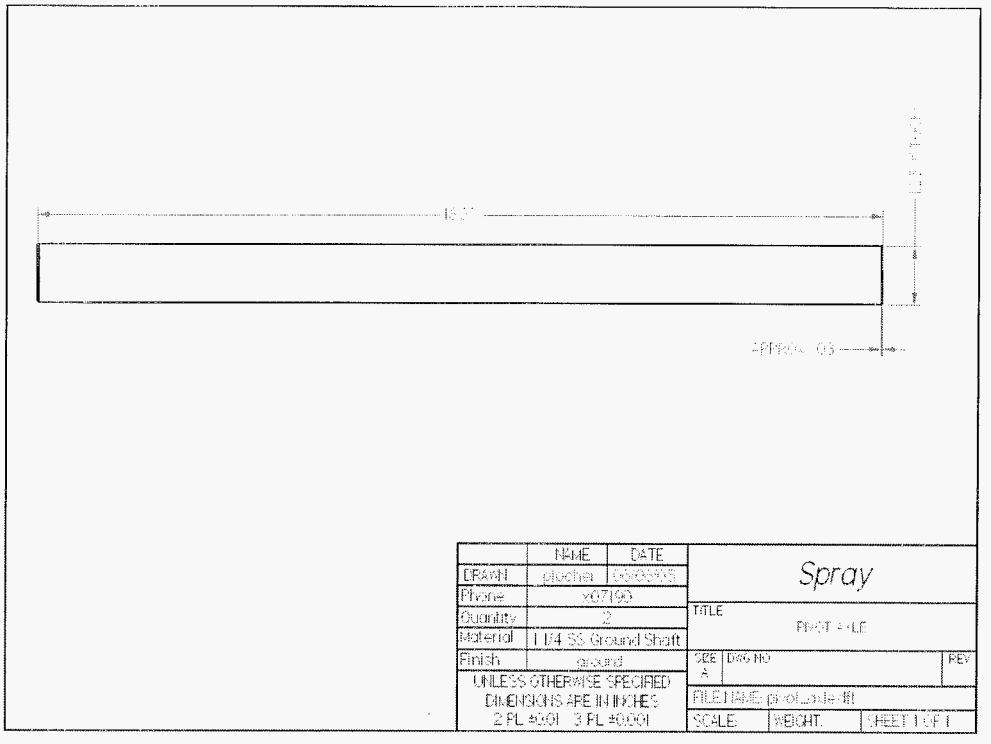

Figure 22. Top axle for pivoting tire

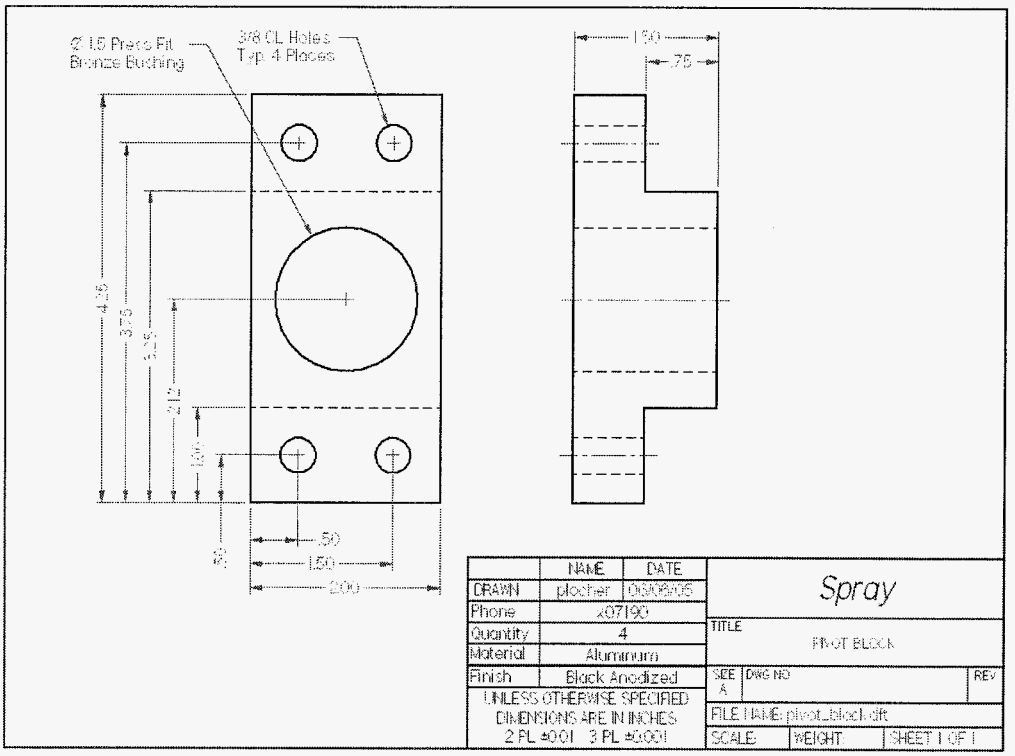

Figure 23. Pivot block for pivoting tire

Wheels/Tires

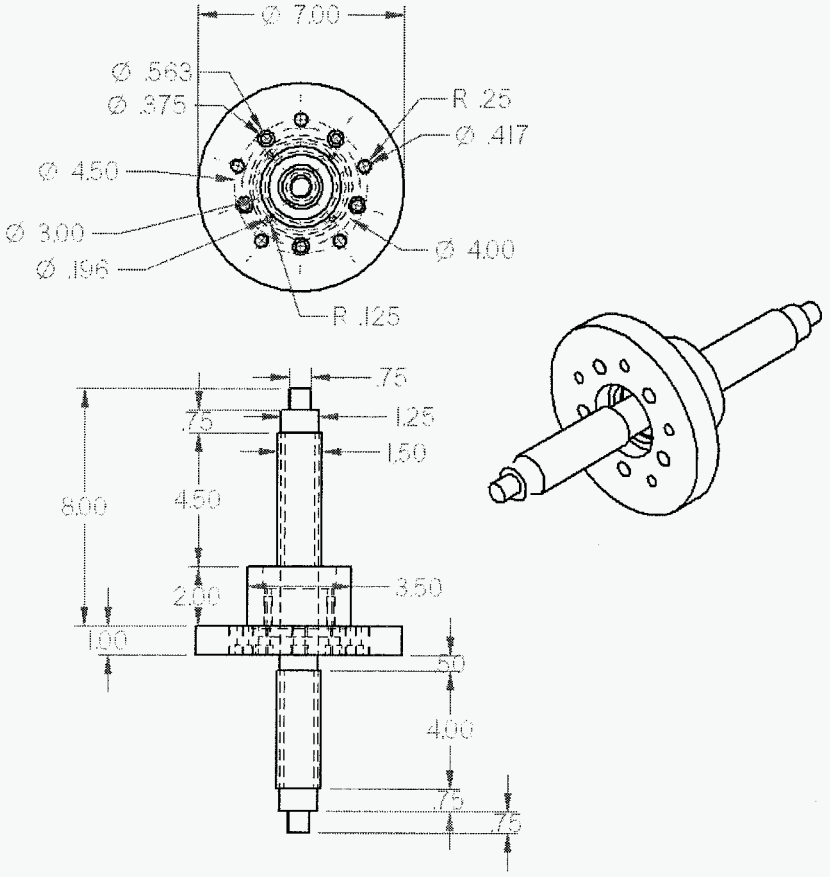

Figure 24. Tire Hub Assembly

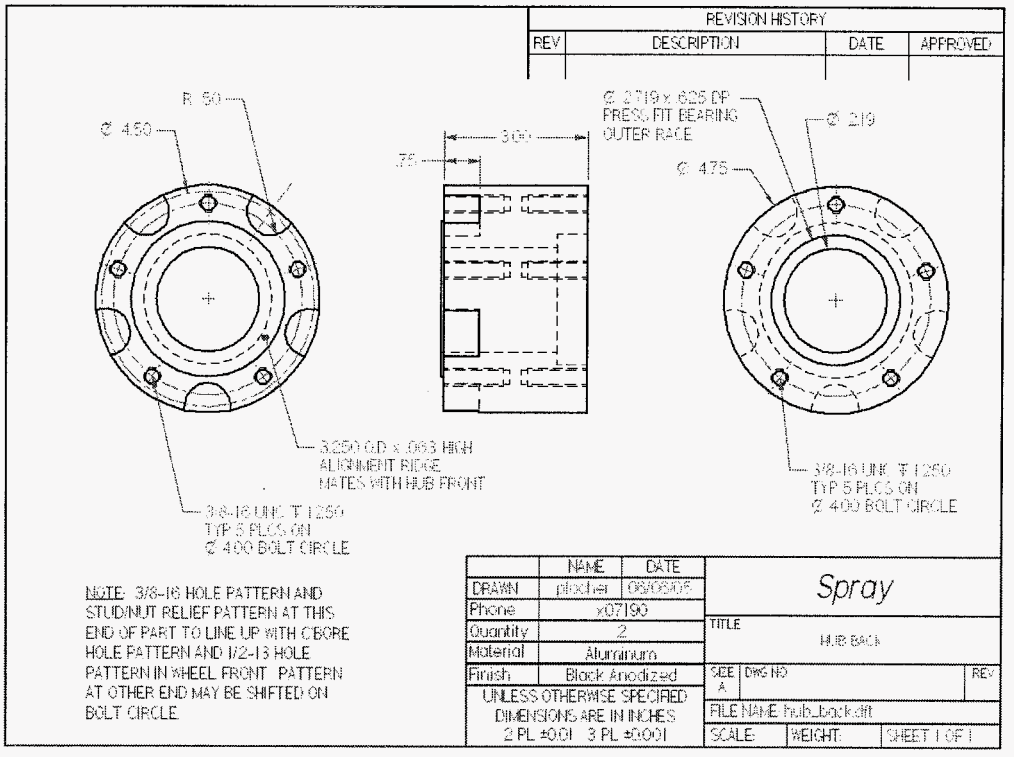

Figure 25. Tire hub back part

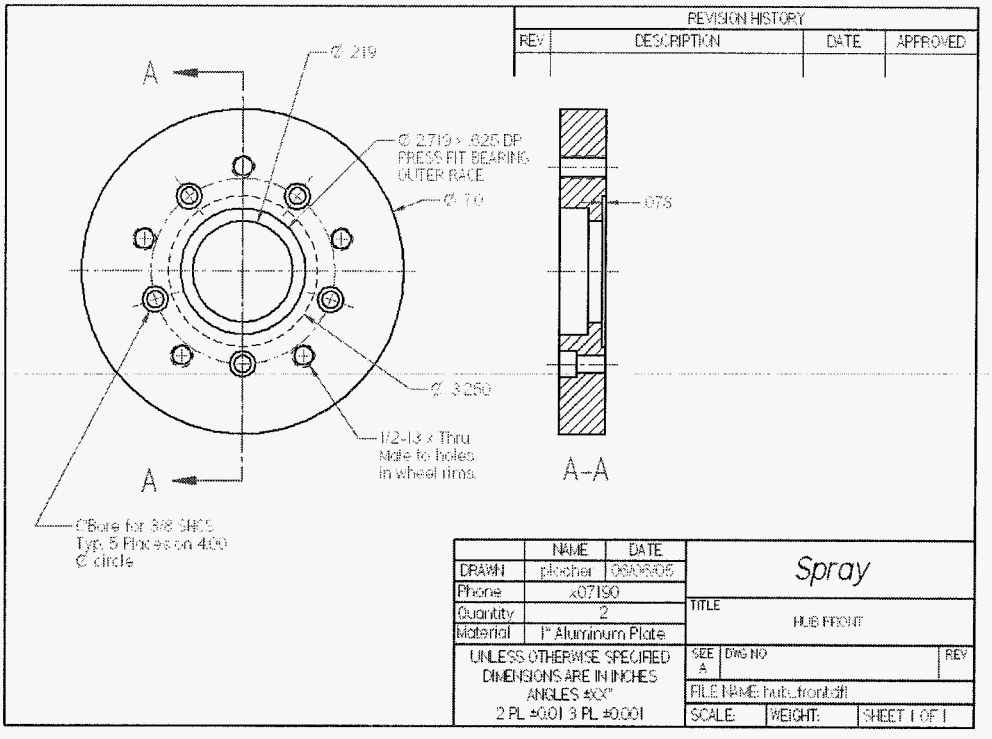

Figure 26. Tire Hub front part and mounting plate

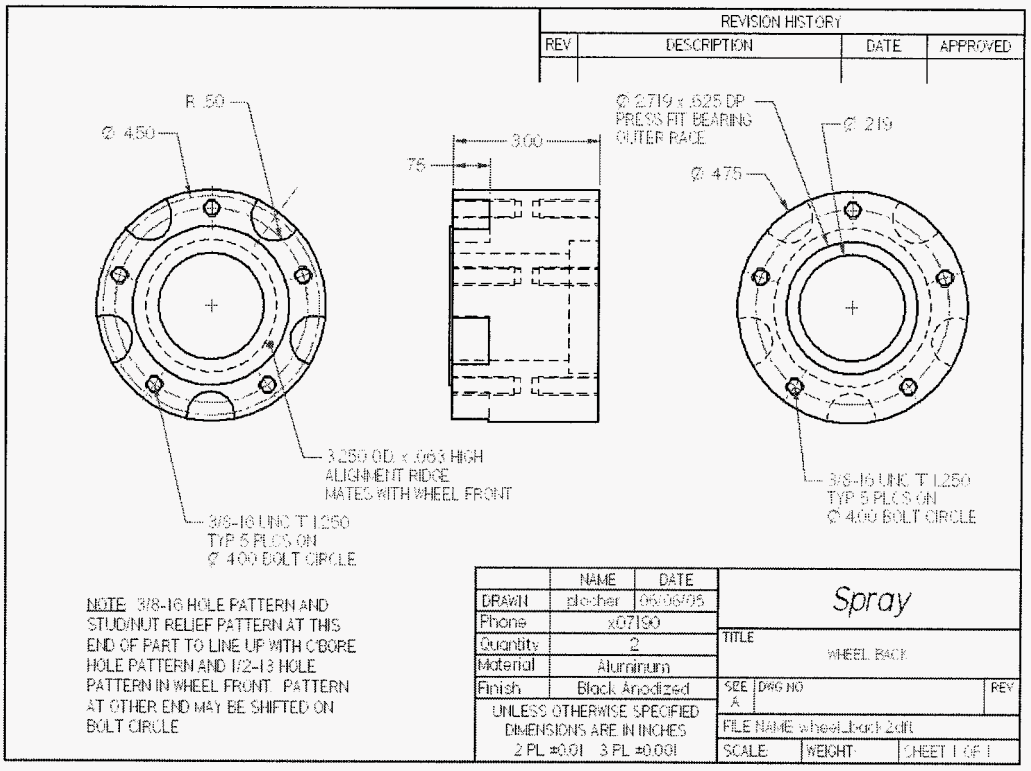

Figure 27. Wheel mount back part

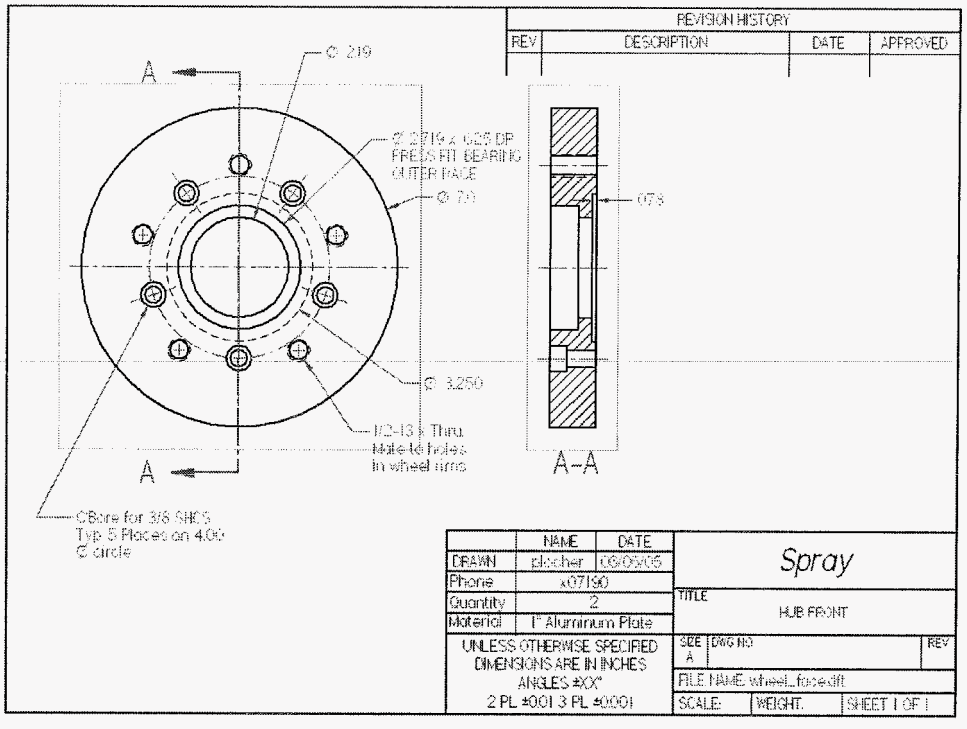

Figure 28. Tire hub front part

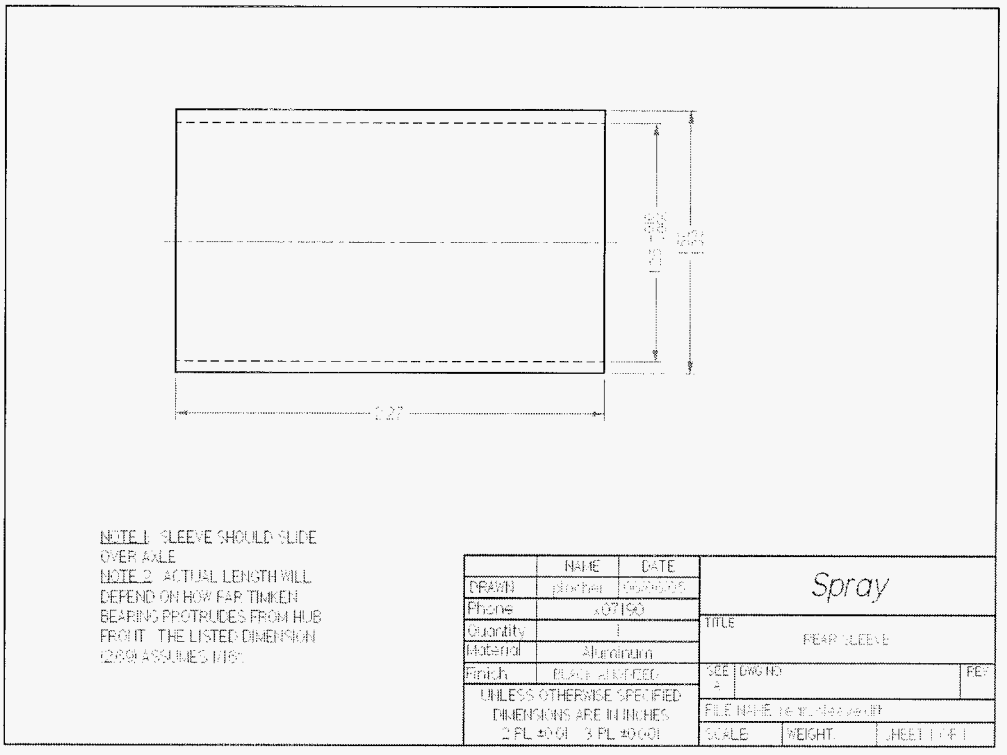

Figure 29. Rear sleeve for tire pivot

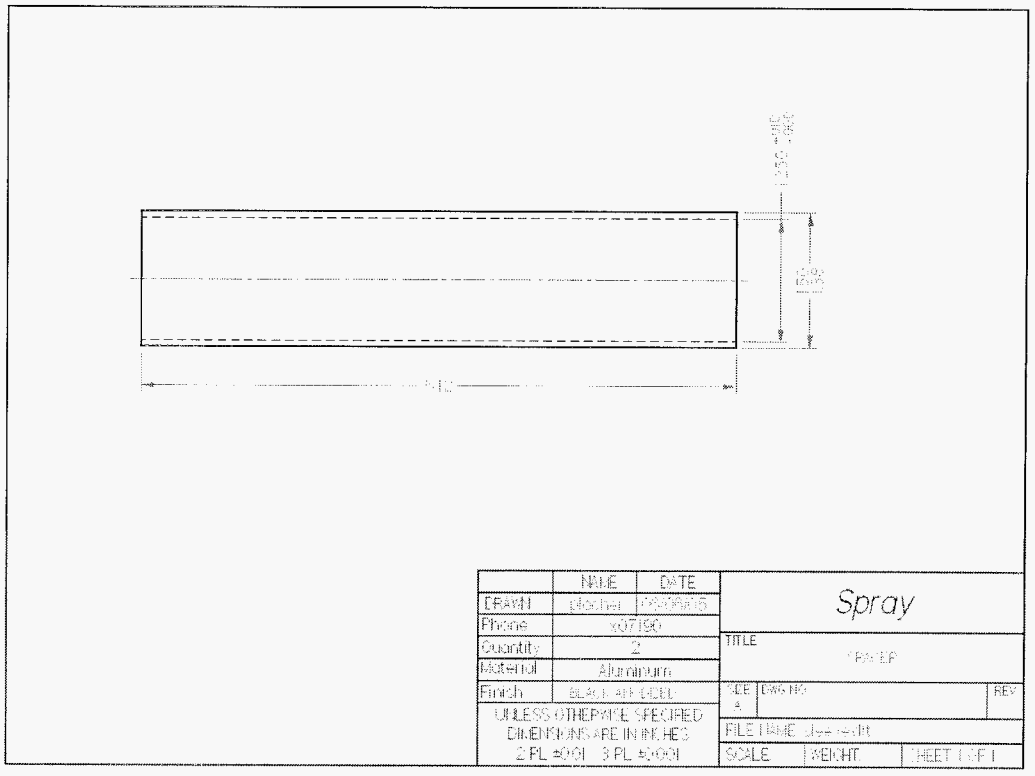

Figure 30. Axle spacer

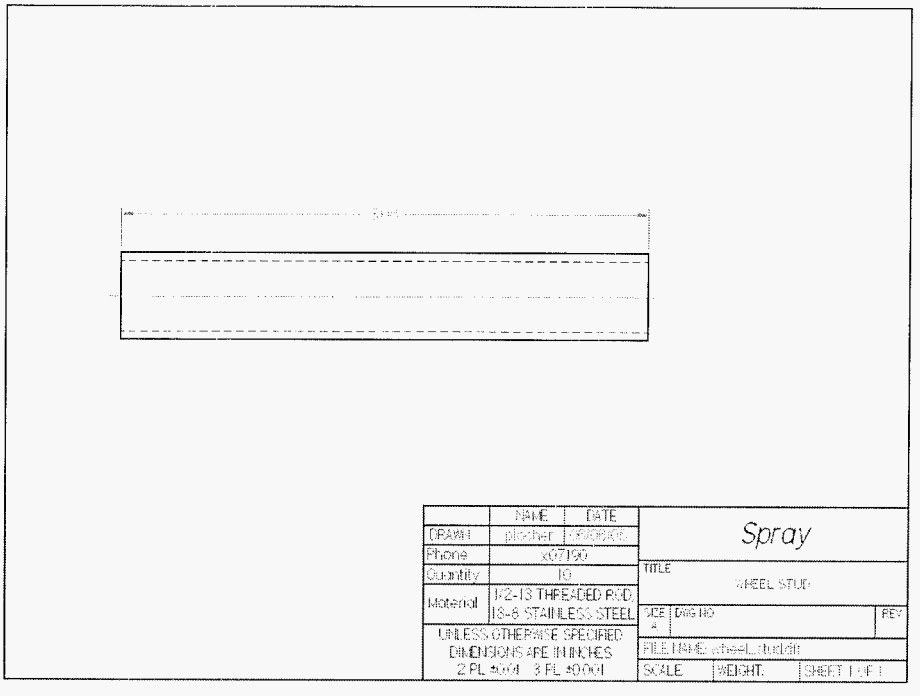

Figure 31. Wheel stud

Tachometer

The following parts are from the tachometer system that will measure the rotation rate of the moving tires.

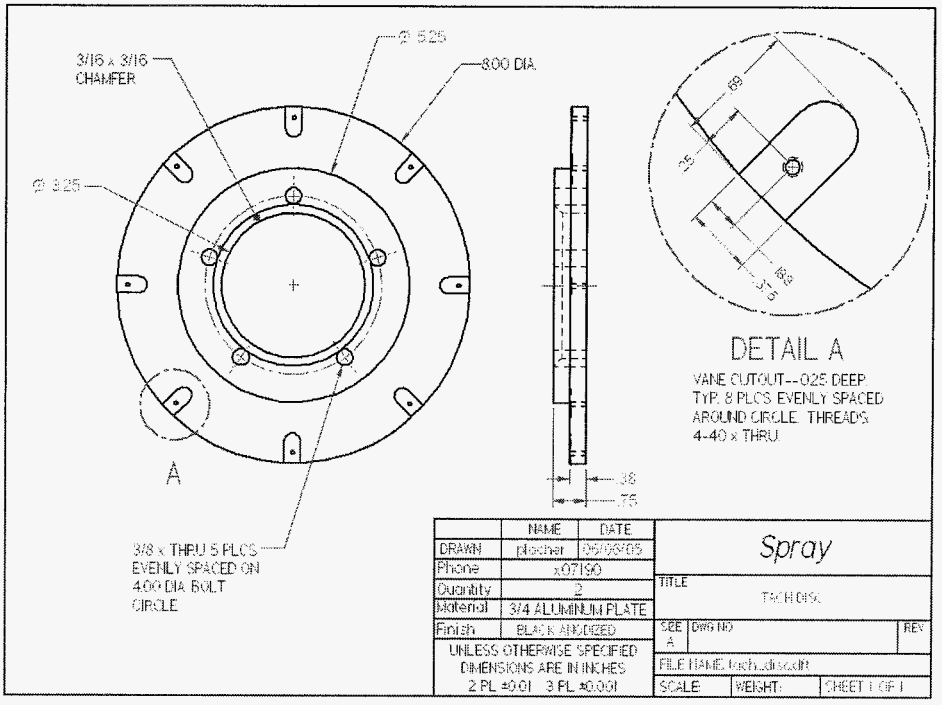

Figure 32. Tachometer Disc

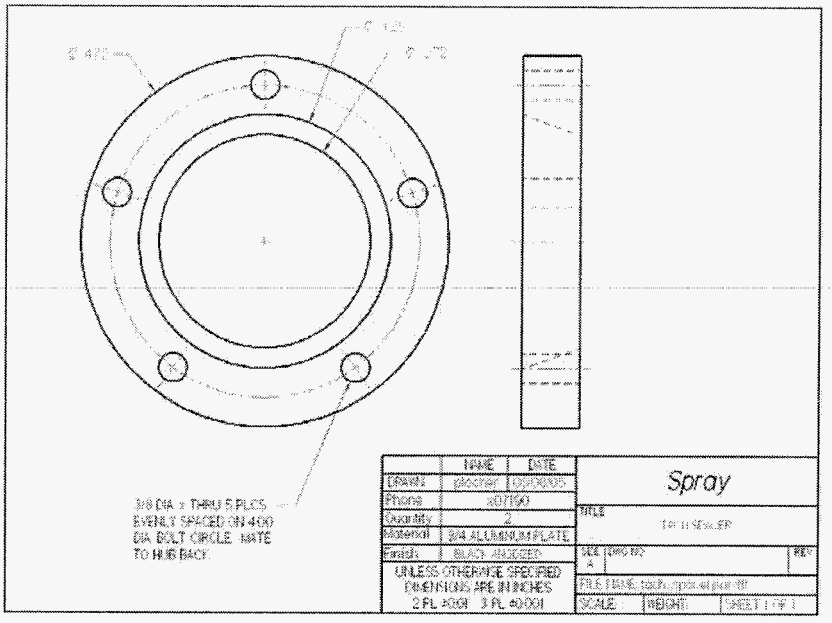

Figure 33. Tachometer spacer

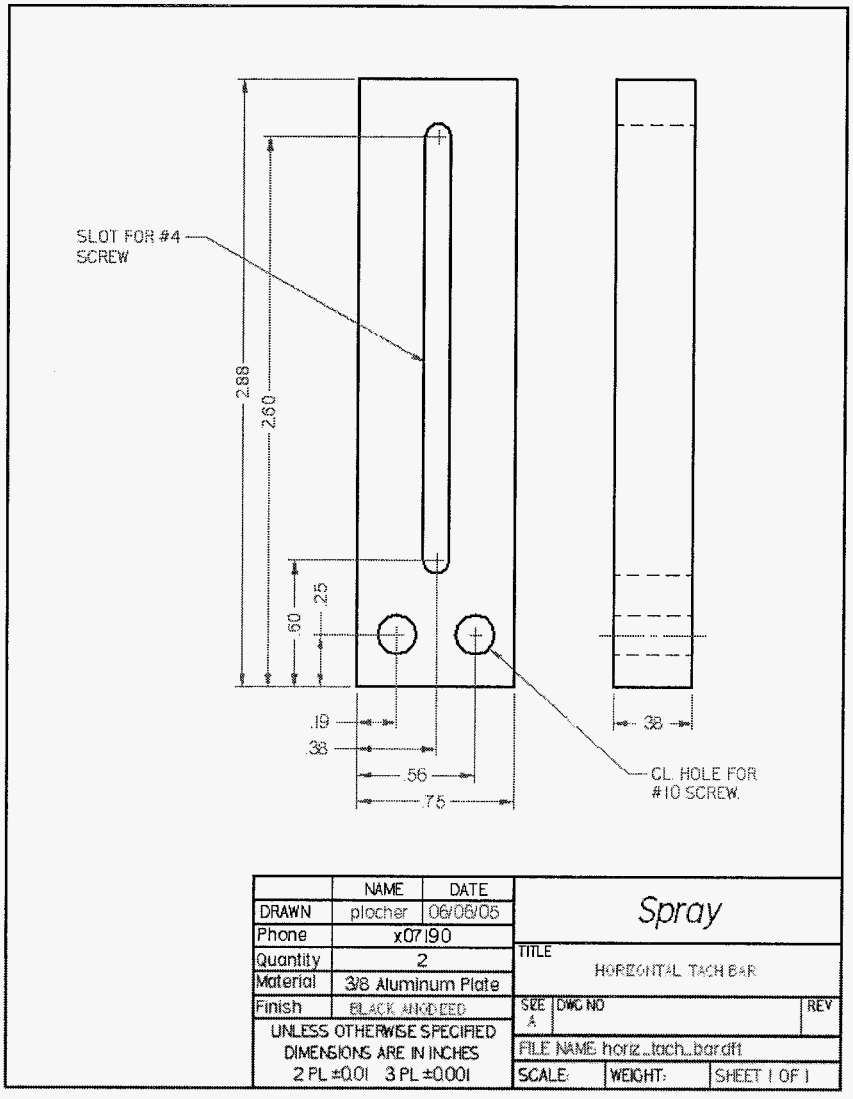

Figure 34. Horizontal support for tachometer assembly

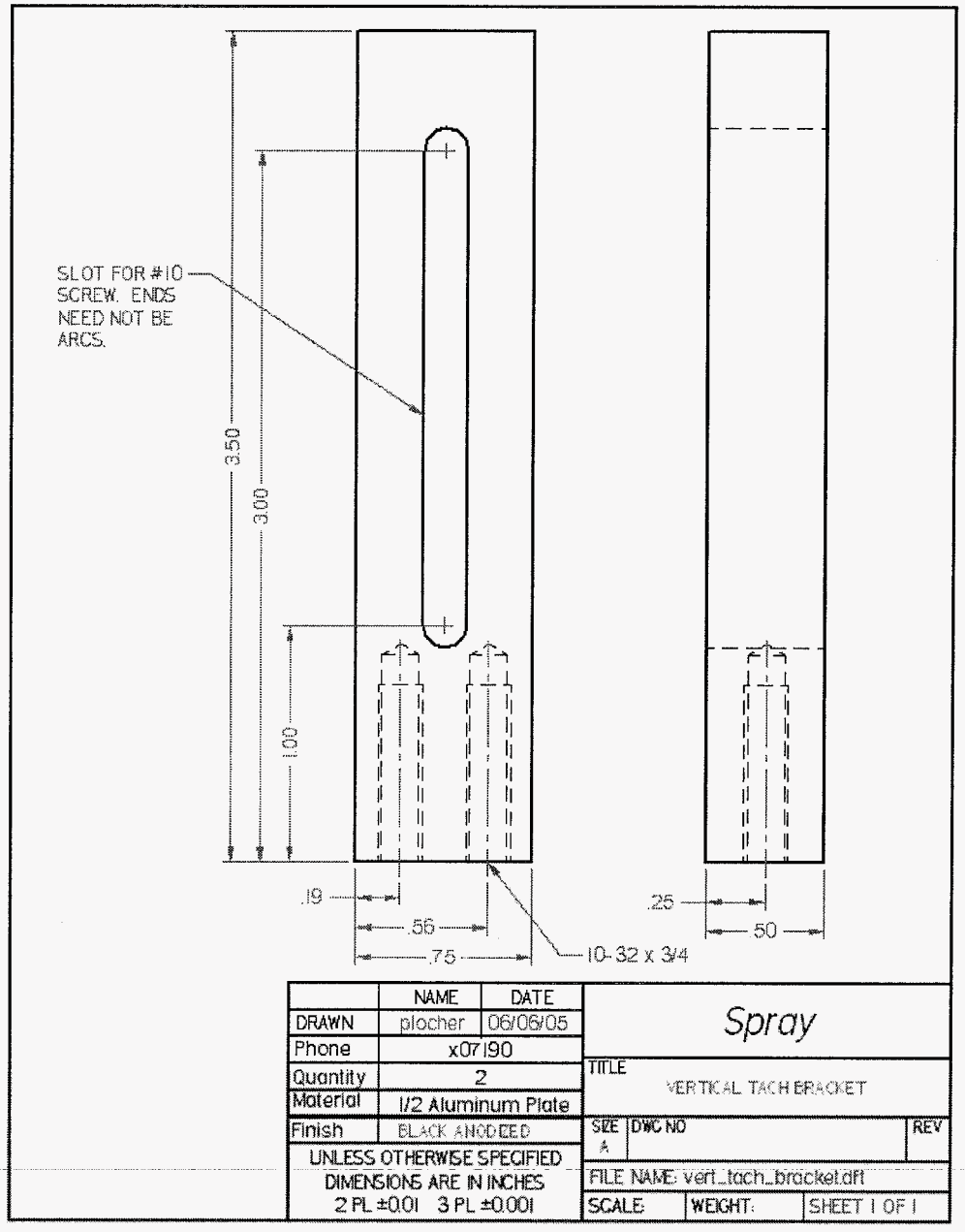

Figure 35. Vertical support for tachometer assembly

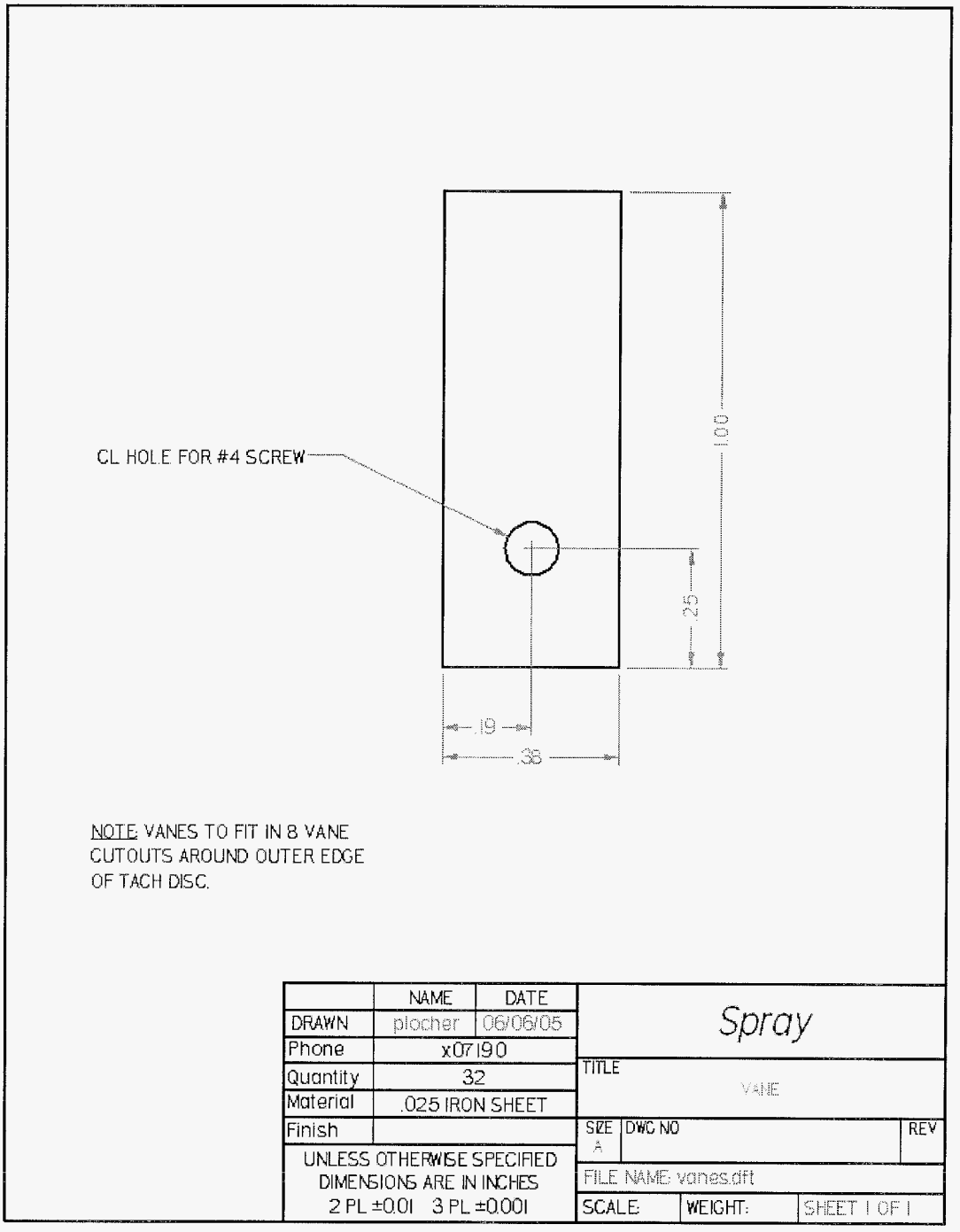

Figure 36. Vane for tachometer sensor

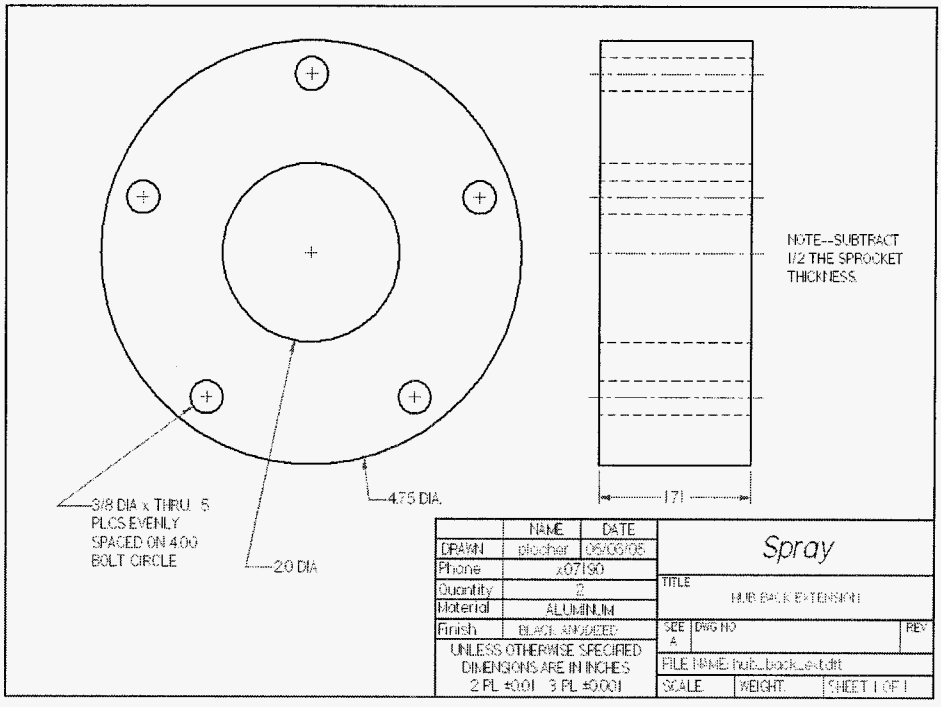
3/8 DIA x THRU. 5
PLCS EVENLY
SPACED ON 4.00
BOLT CIRCLE
2.0 DIA
4.75 DIA.
NOTE--SUBTRACT
1/2 THE SPROCKET
THICKNESS.
1.71
NAME
DATE
DRAWN
blocher
05/09/05
Phone
x0715G
Quantity
2
Material
ALUMINUM
Finish
BLACK ANODIZED
UNLESS OTHERWISE SPECIFIED
DIMENSIONS ARE IN INCHES
2 PL ±0.01 3 PL ±0.001
Spray
TITLE
HUB BACK EXTENSION
SIZE
A
DWG NO
REV
FILE NAME hub_back_ext.dft
SCALE
WEIGHT
SHEET 1 OF 1

Left Hand Side Traverse System

The left traverse system includes the motor and the left hand of the suspension system. Its assemblies as well as part files are included. Parts common to both the left and right traverse systems are included in the left traverse system portion of the appendix.

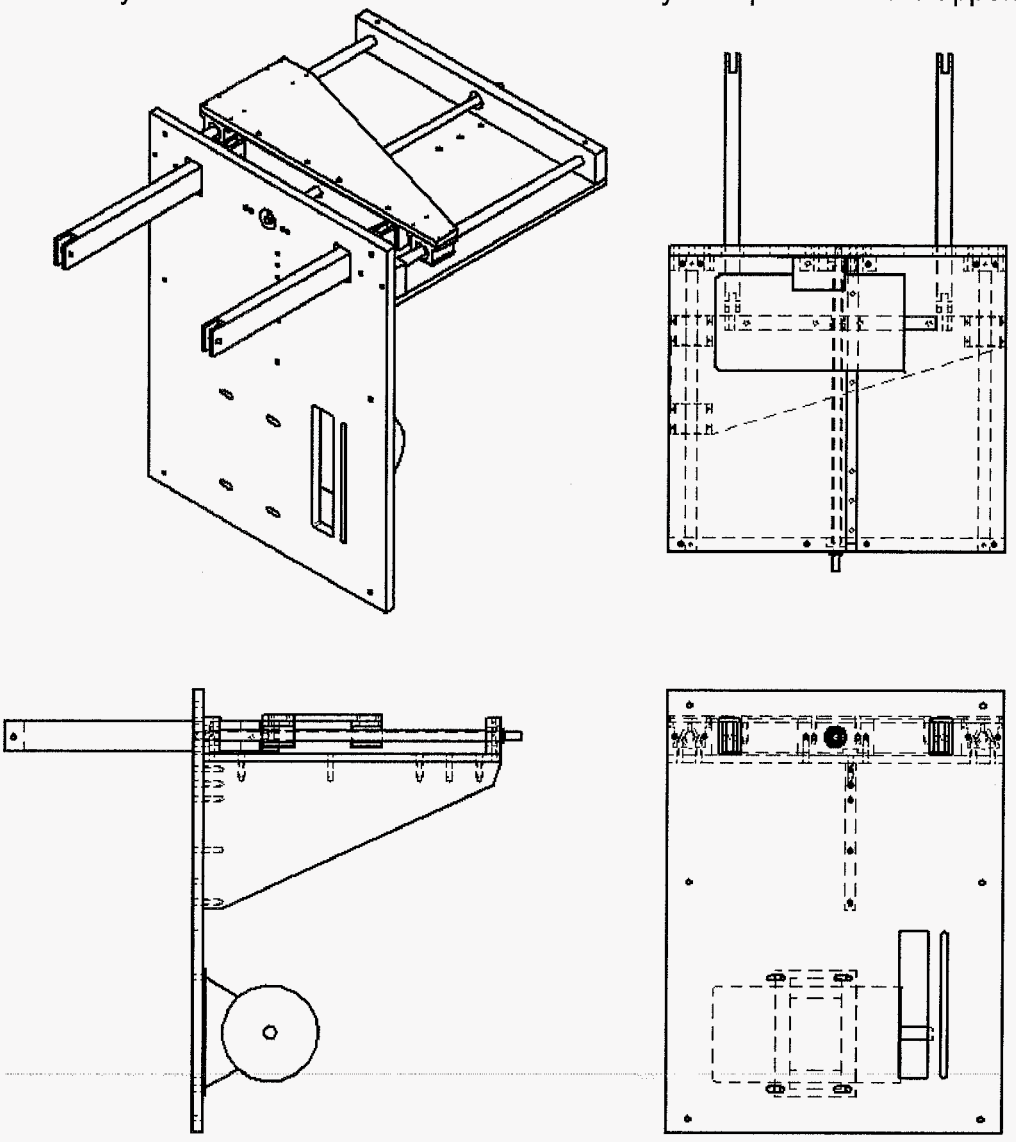

Figure 37. Traverse system with motor attached

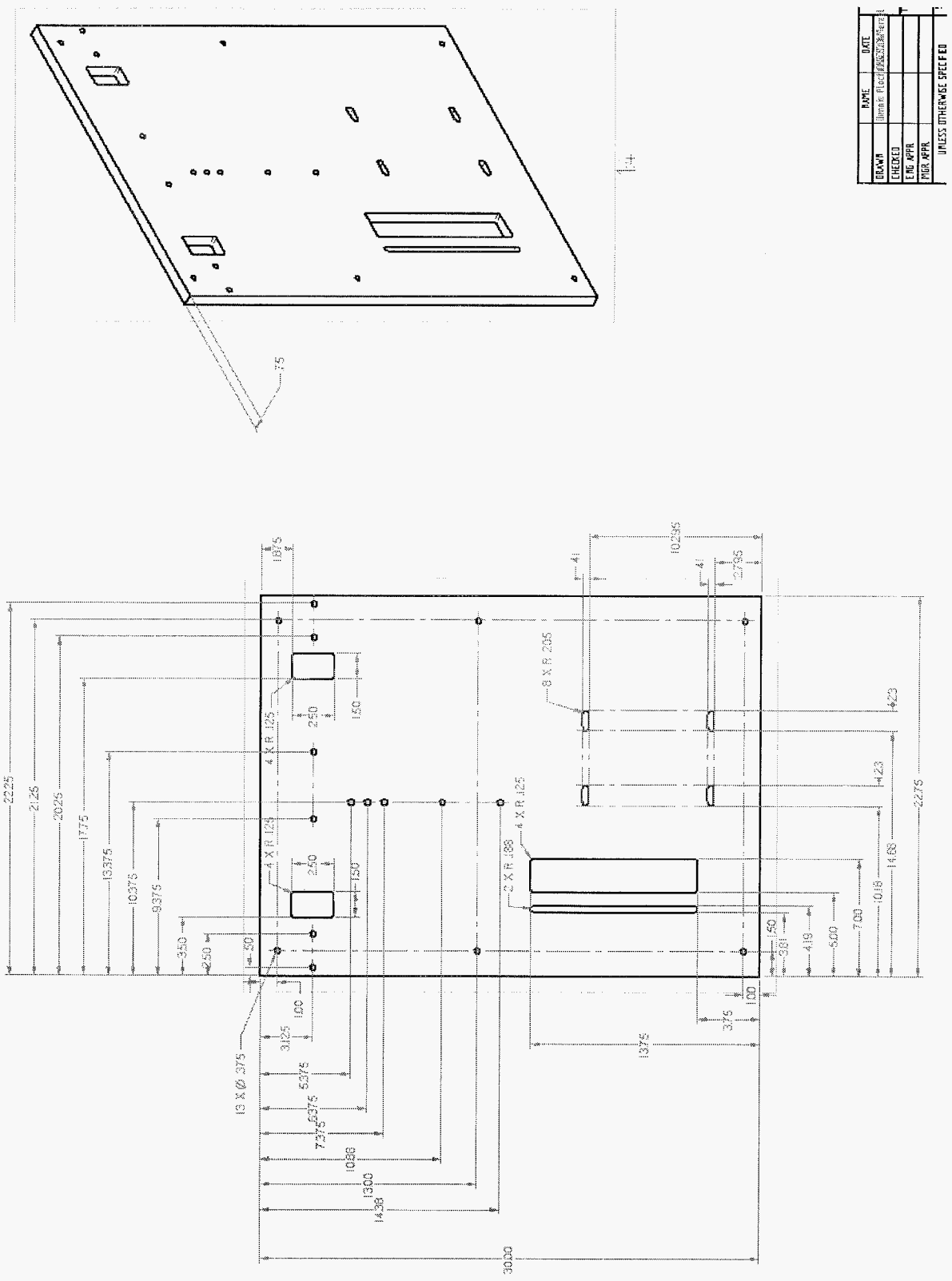

Figure 38. Mounting plate for motor

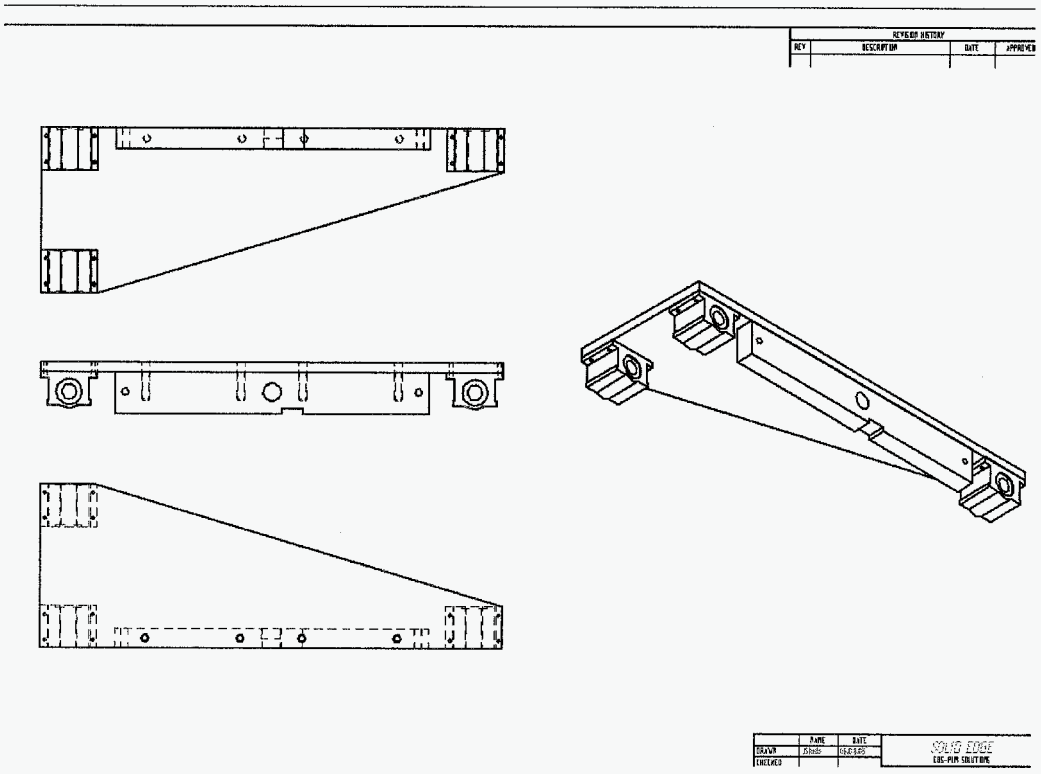

Figure 39. General traverse plate

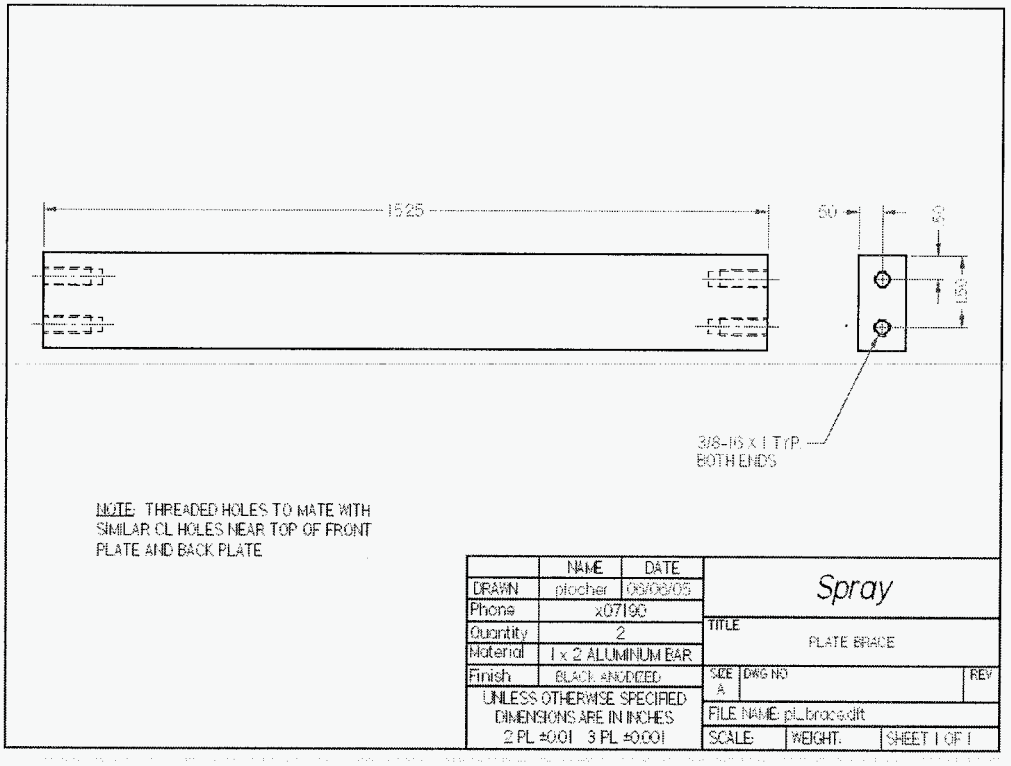

Figure 40. Plate brace

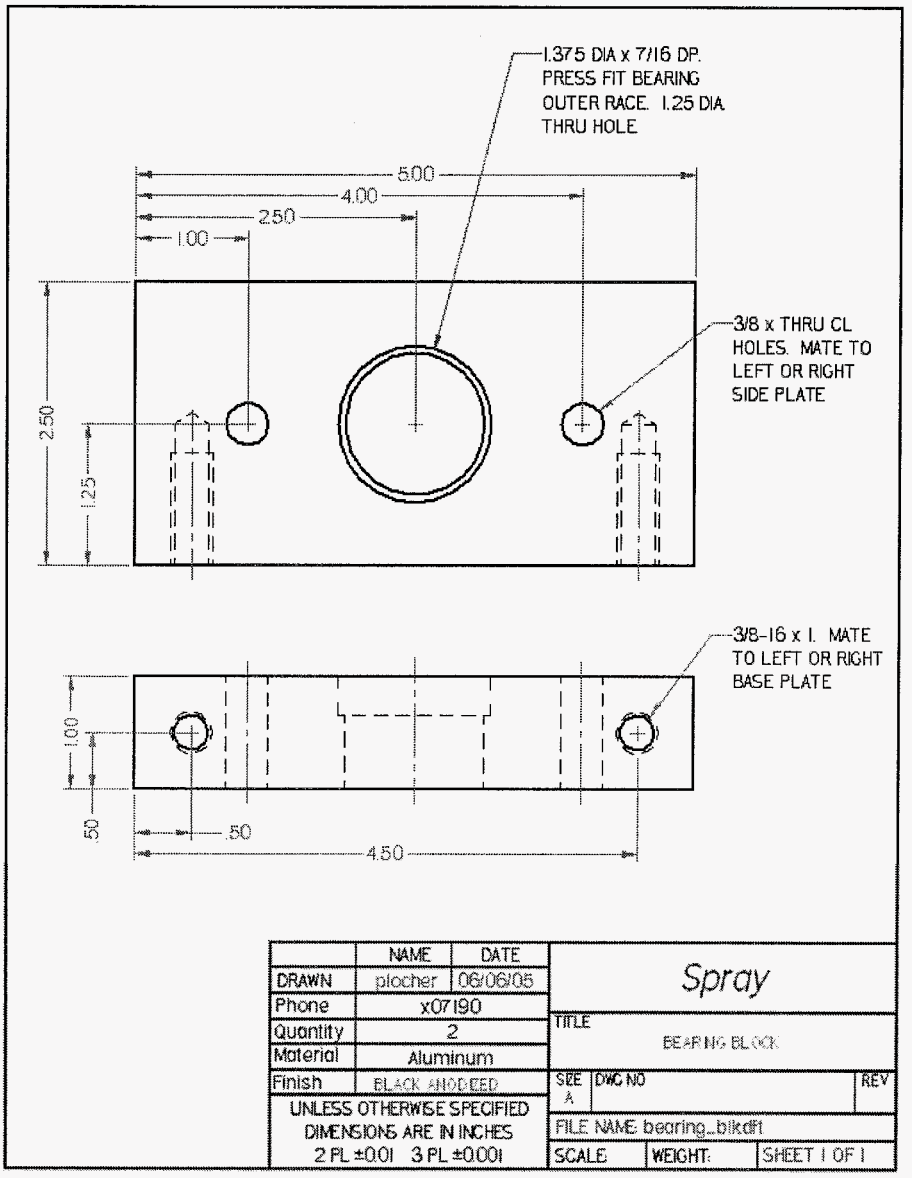

Figure 41. Bearing block

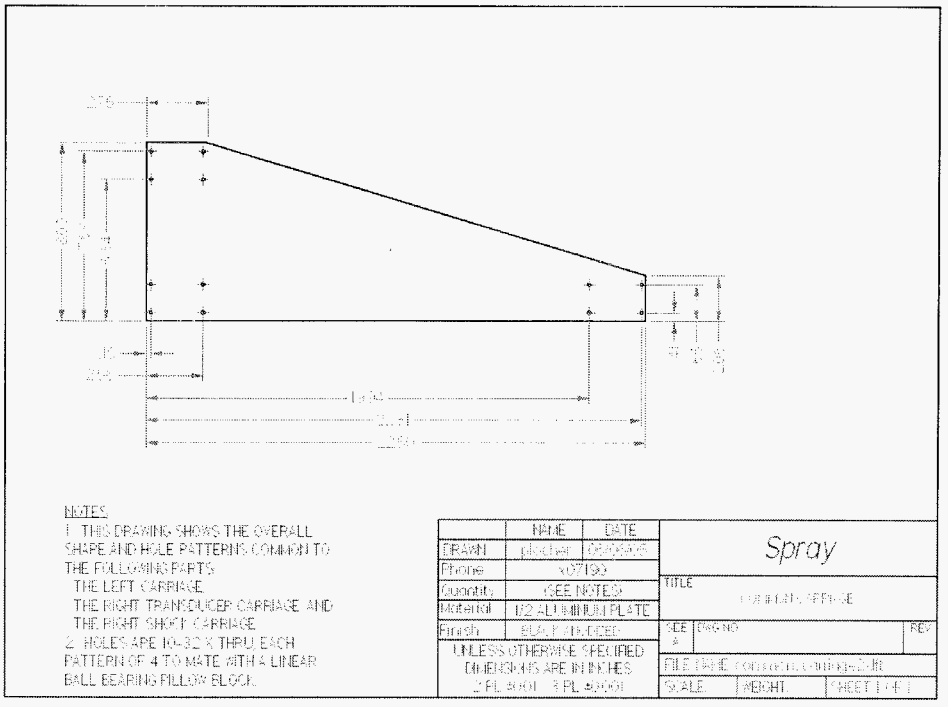

Figure 42. General Carriage

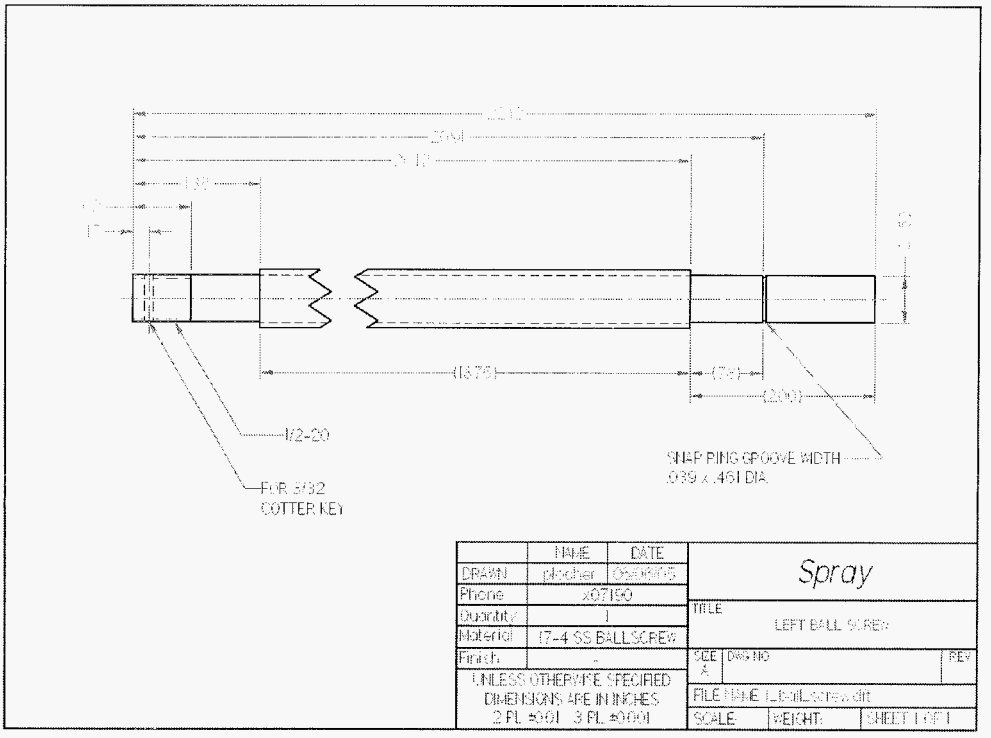

Figure 43. Ball screw for left side

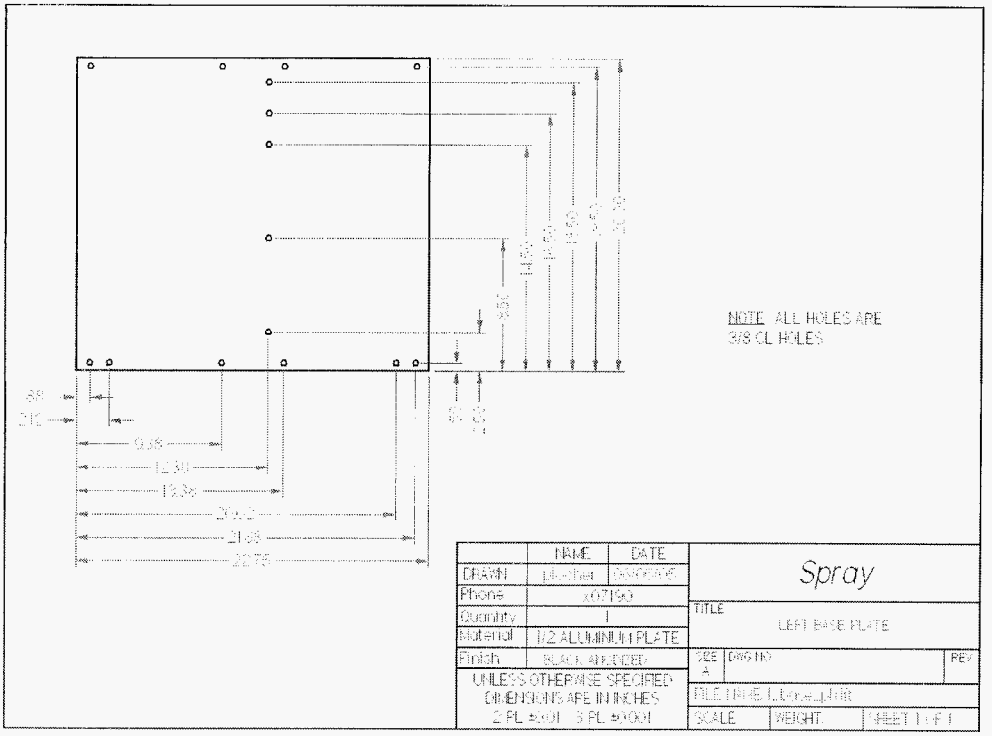

Figure 44. Left Base plate

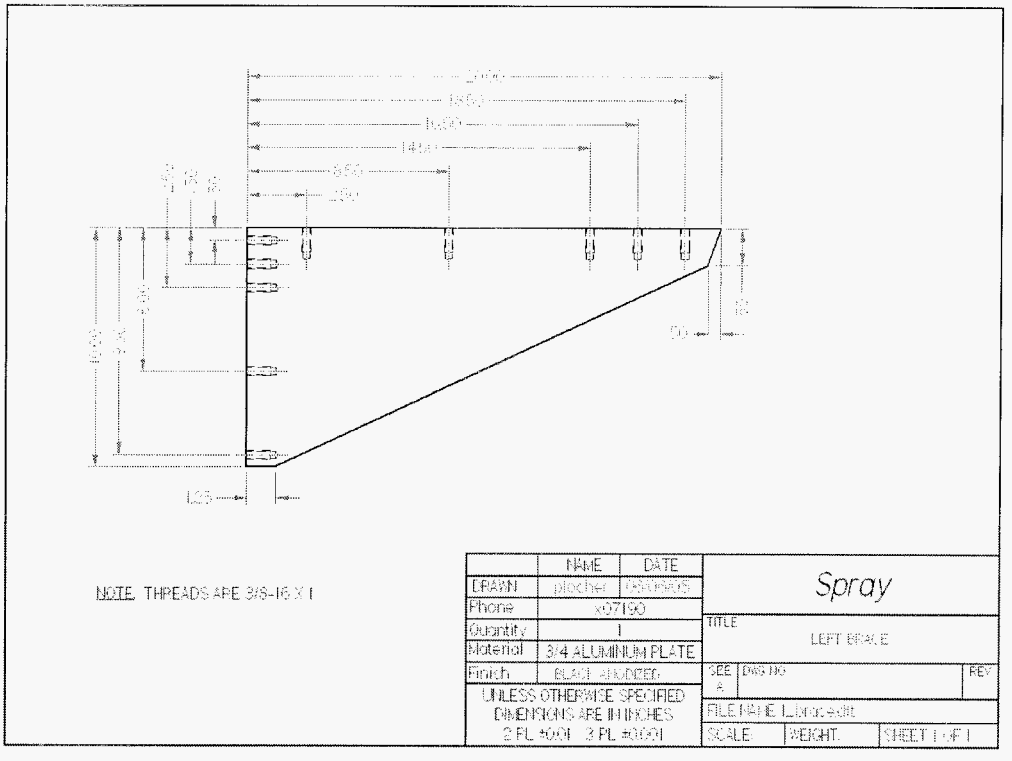

Figure 45. Brace for left traverse

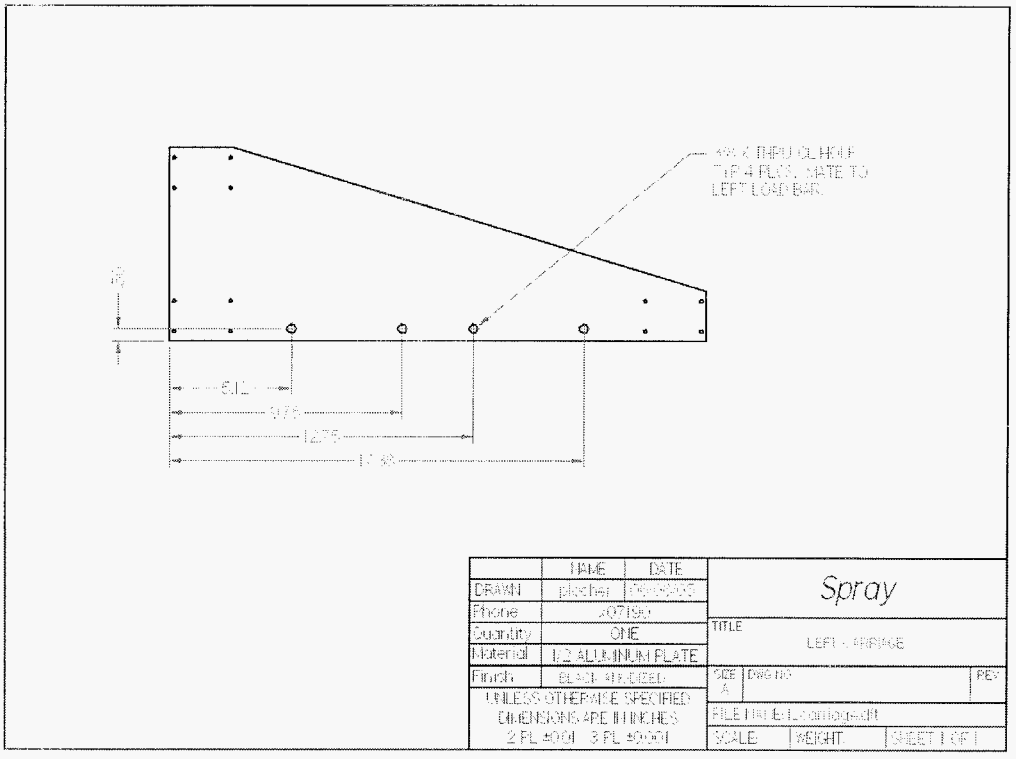

Figure 46. Left side Carriage

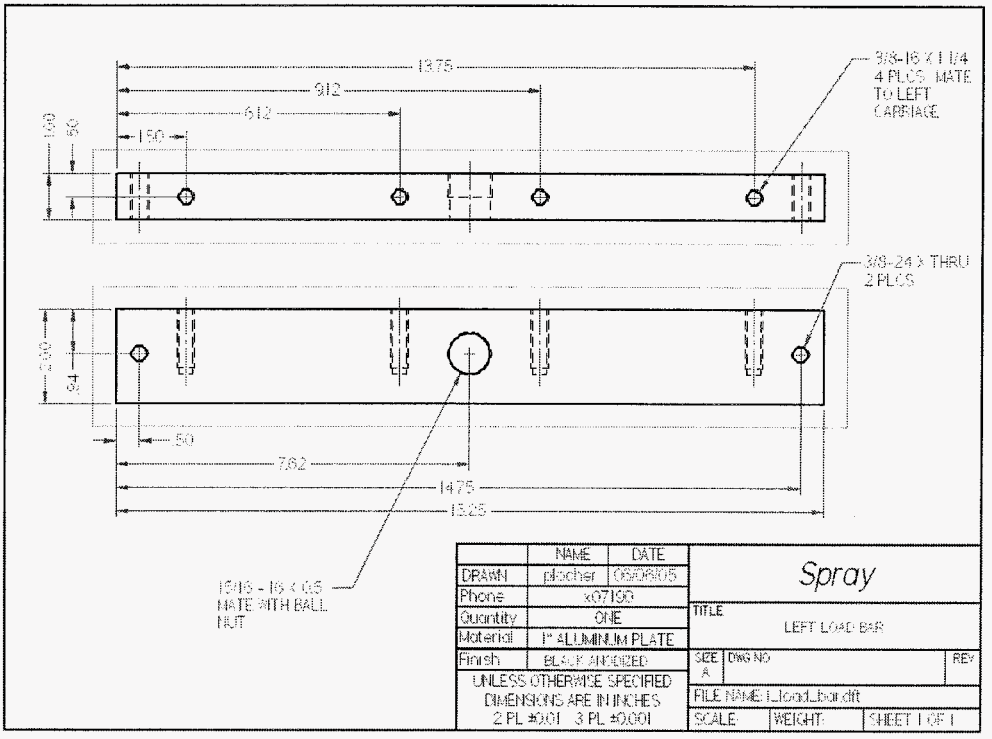

Figure 47. Left side load bar

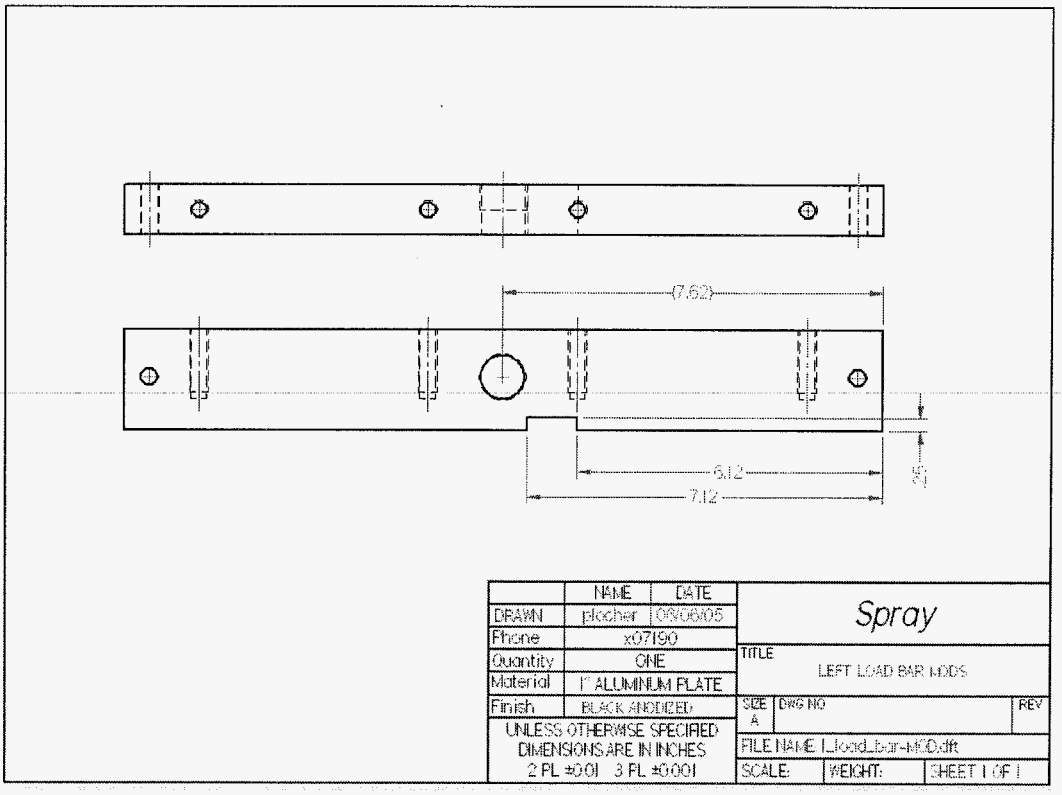

Figure 48. Left side load bar with center hole modification

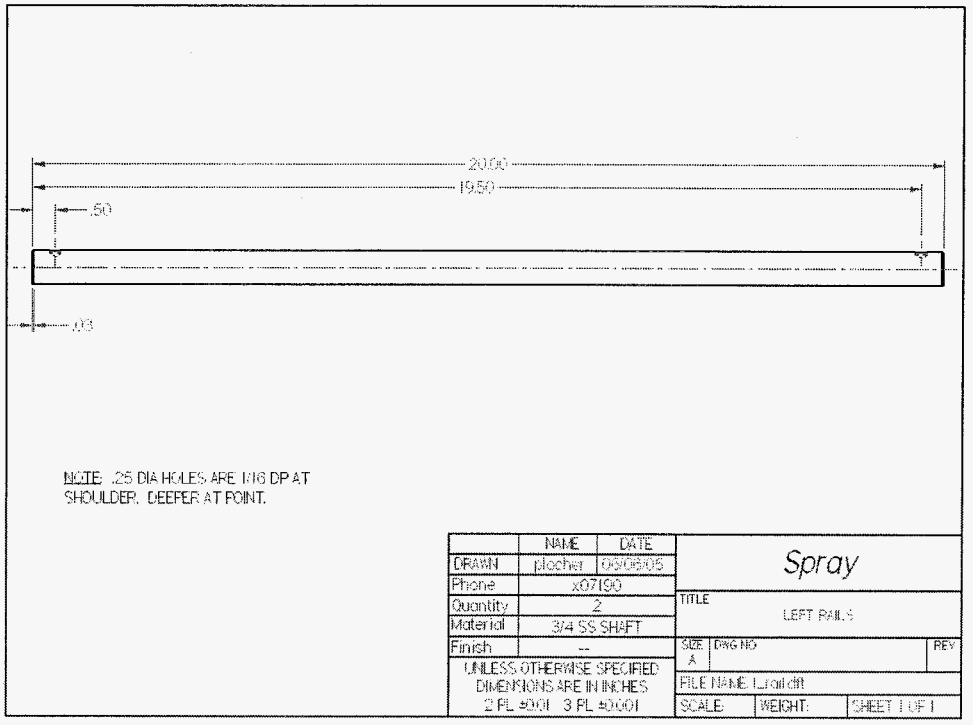

Figure 49. Left side rail.

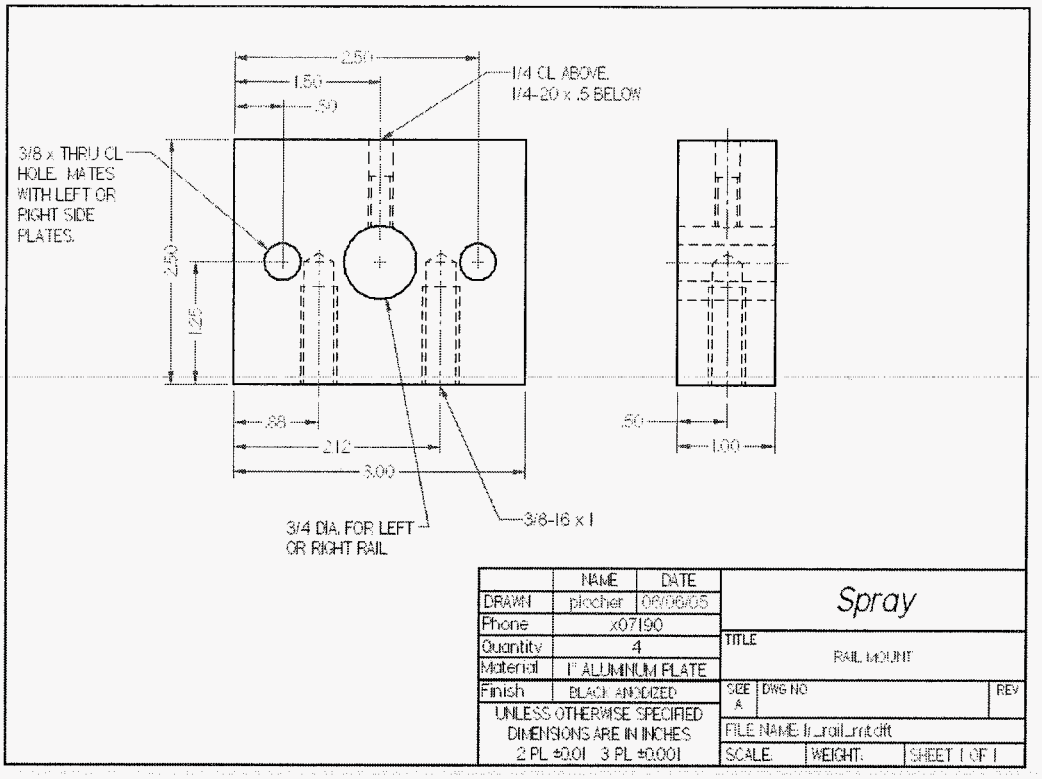

Figure 50. Mount for rail

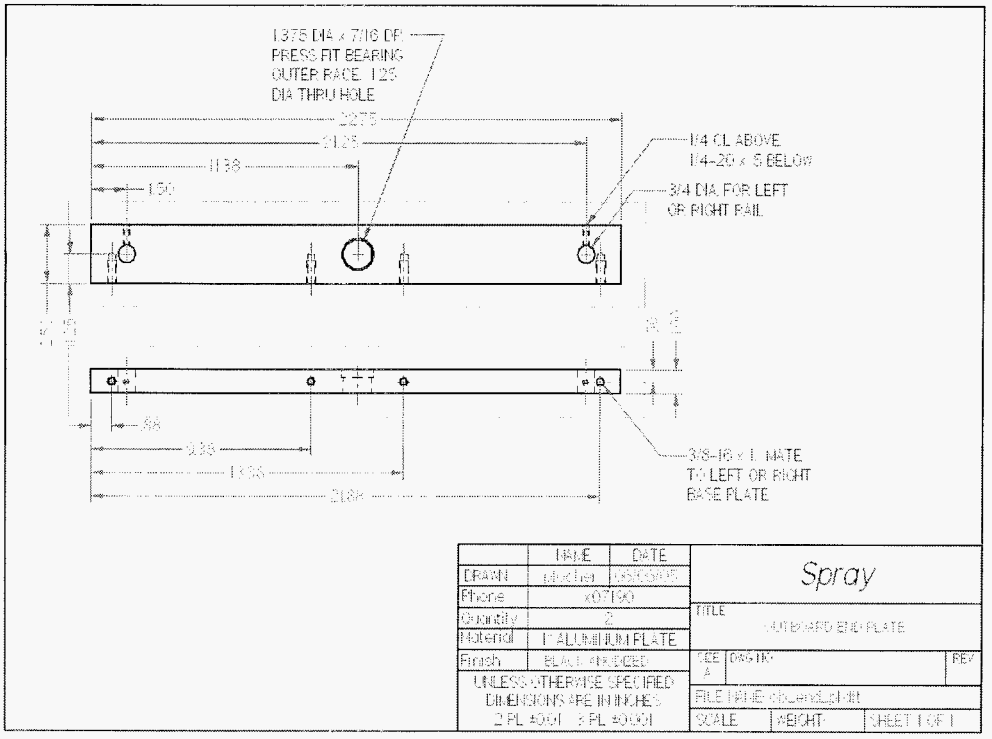

Figure 51. Outboard end plate.

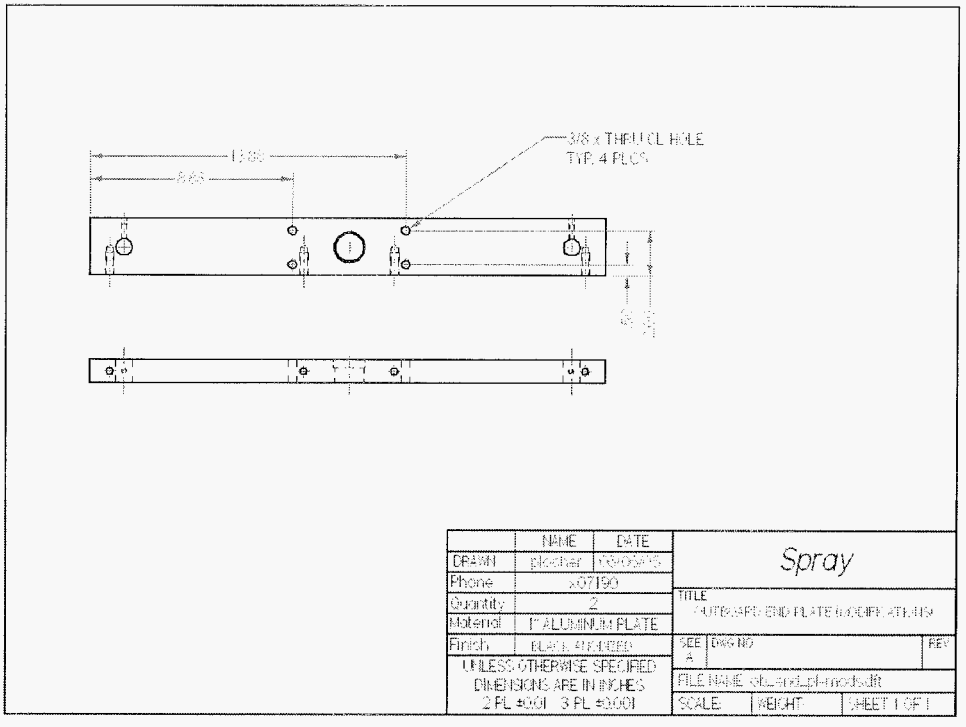

Figure 52. Outboard end plate with hole modifications

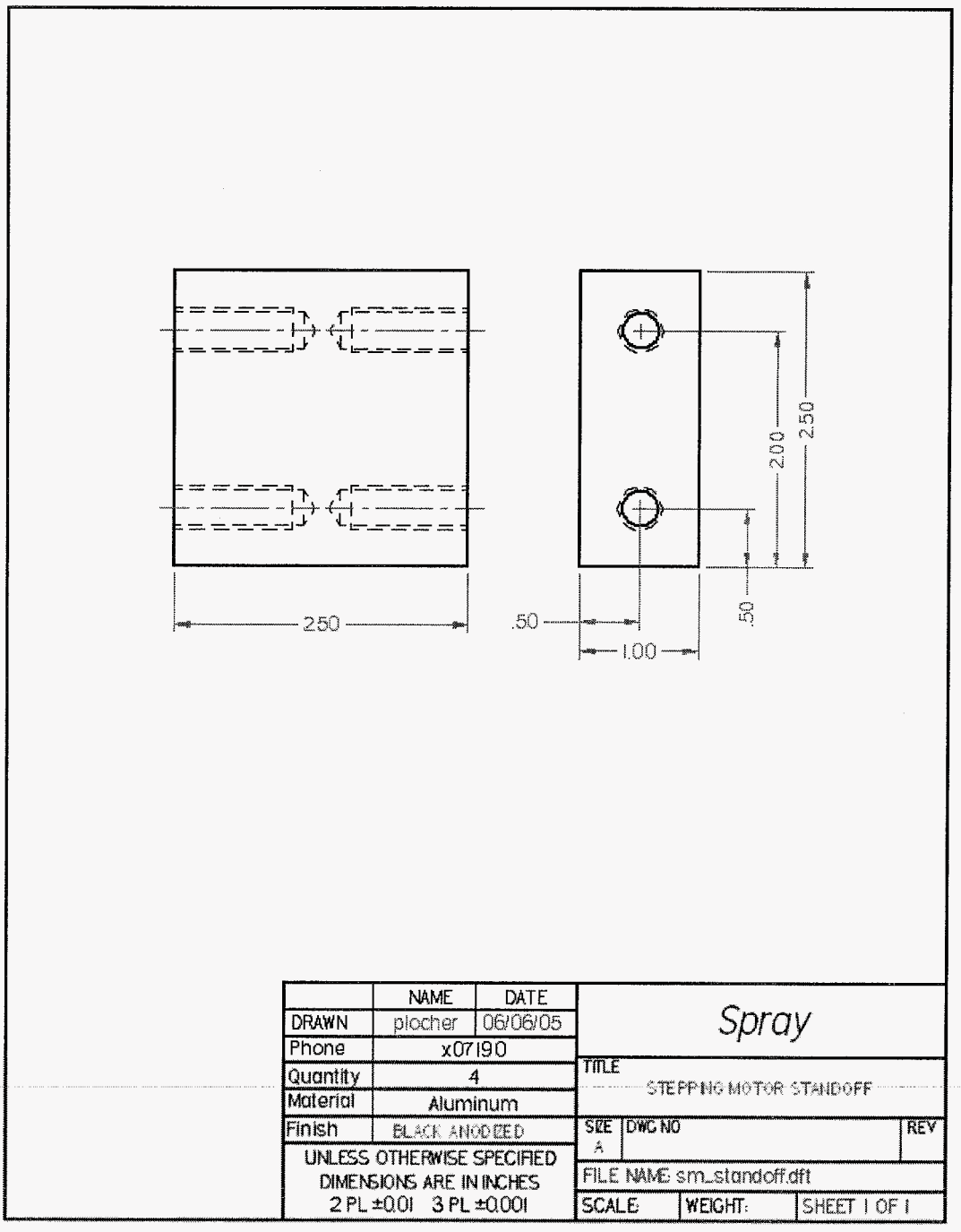

Figure 53. Stepper motor stand-off block

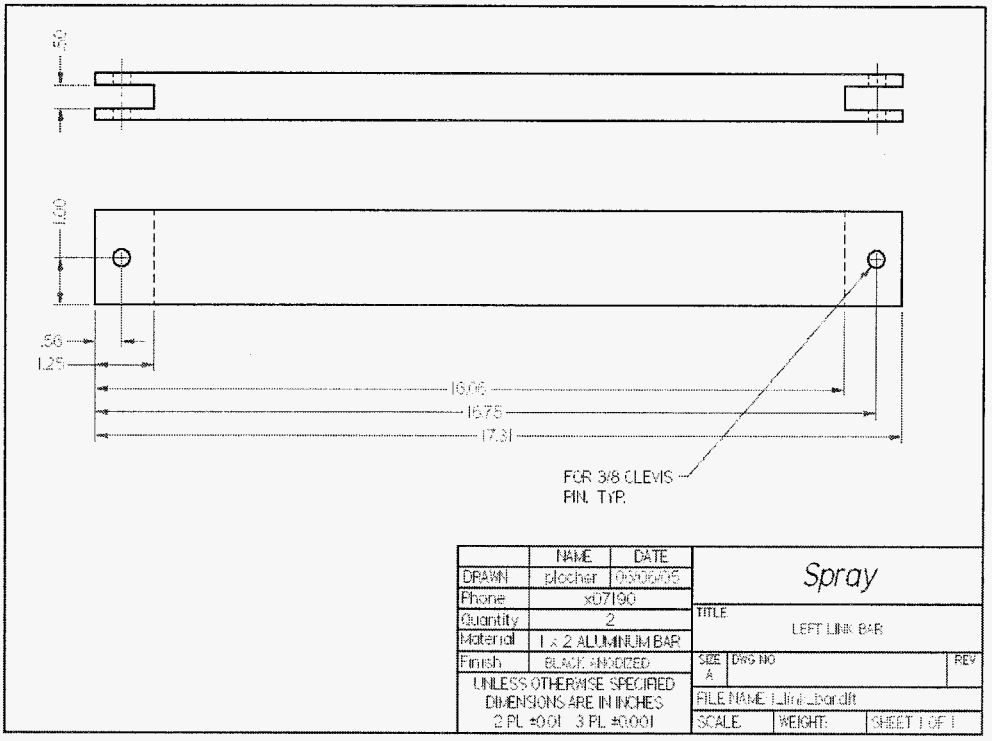

Figure 54. Left link bar

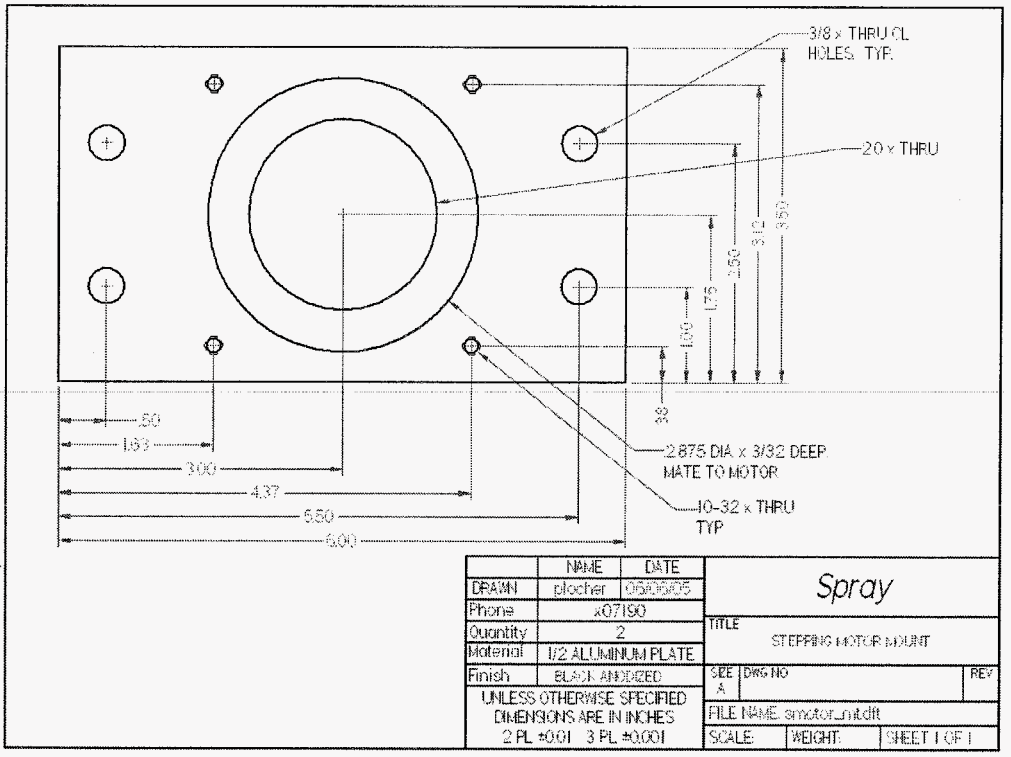

Figure 55. Stepper motor mounting plate

Right Hand Side Traverse System

The assembly and parts for the right traverse system are included. The right traverse system includes the shock absorbers which attach to the right tire (non-motorized) as well as the load cell which measures the pressure in the contact patch.

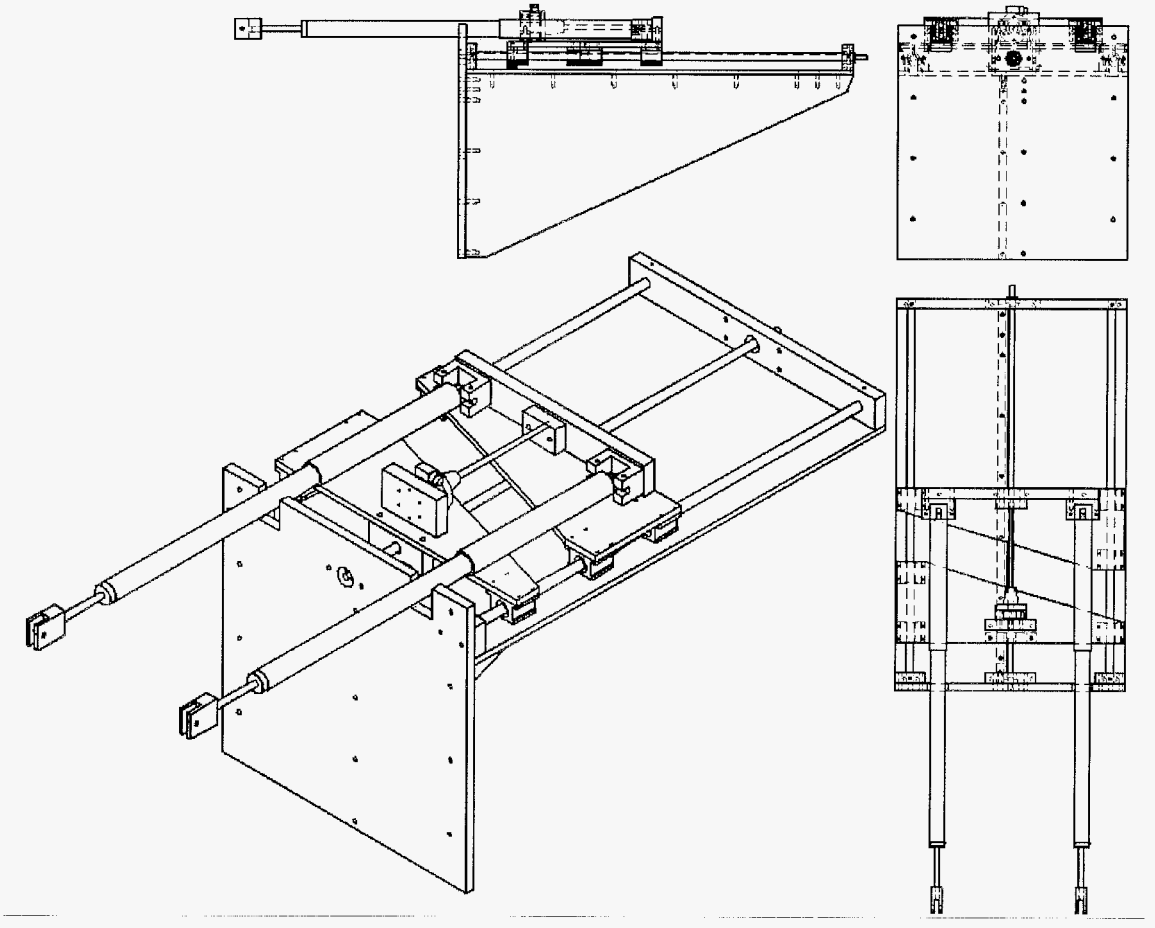

Figure 56. Right hand side traverse system with load cell system

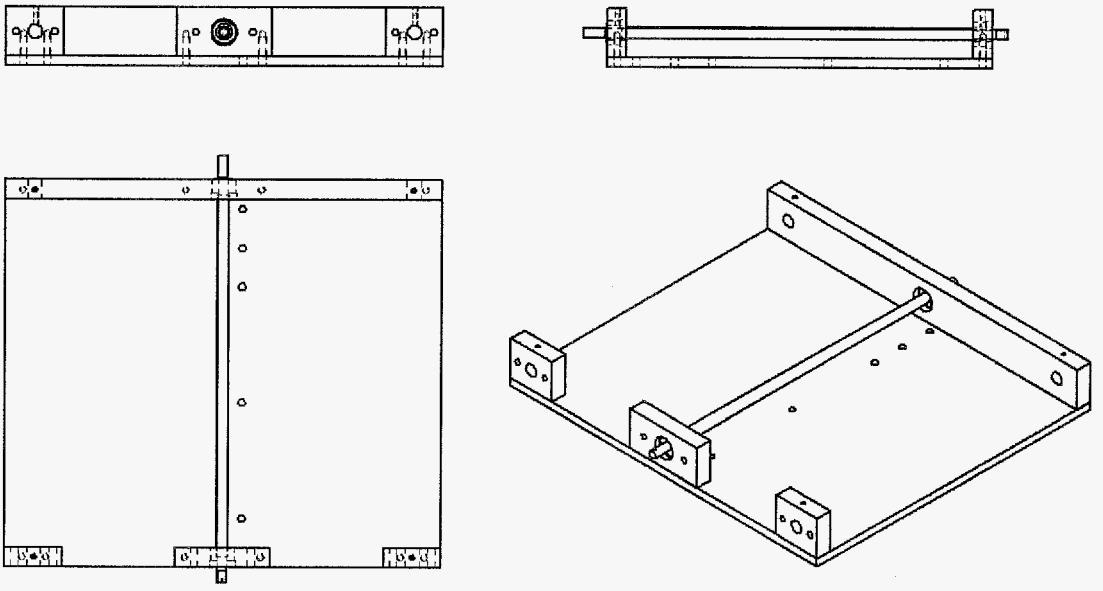

Figure 57. Right hand side traverse plate

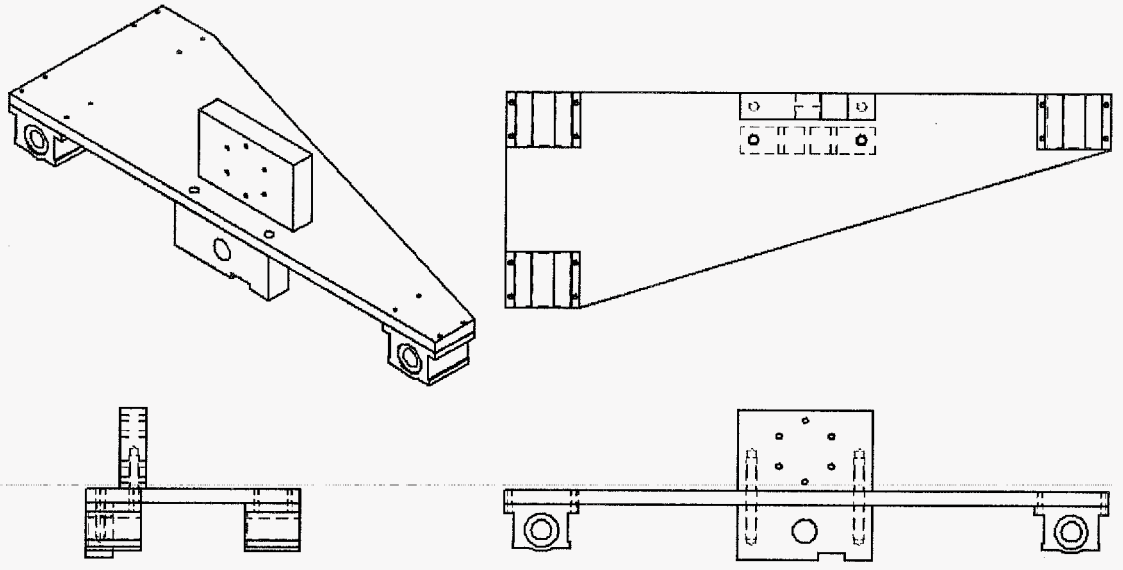

Figure 58. Inboard traverse moving plate

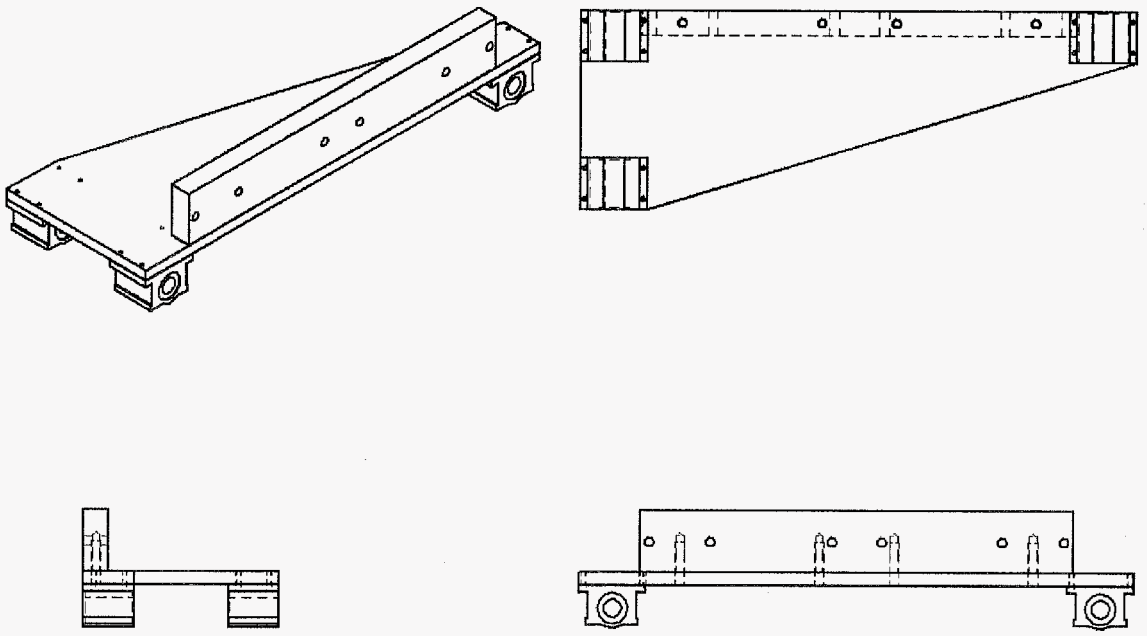

Figure 59. Outboard traverse mounting plate

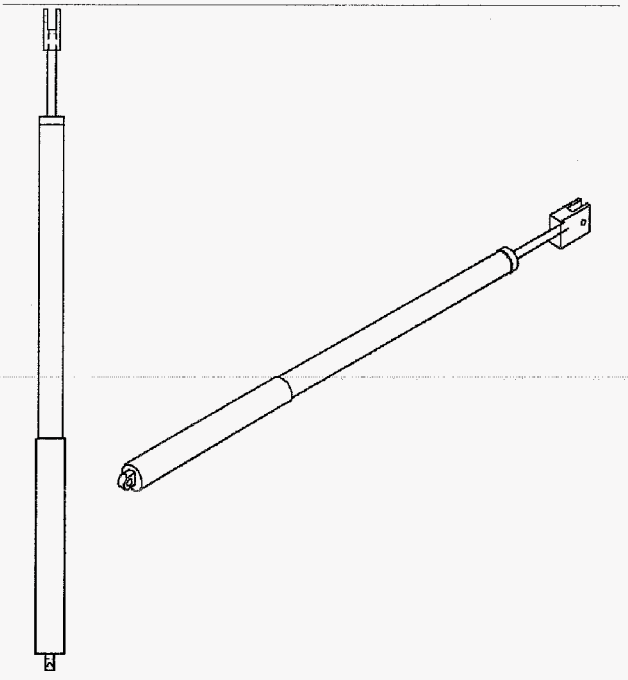

Figure 60. Shock / Spring Dampener

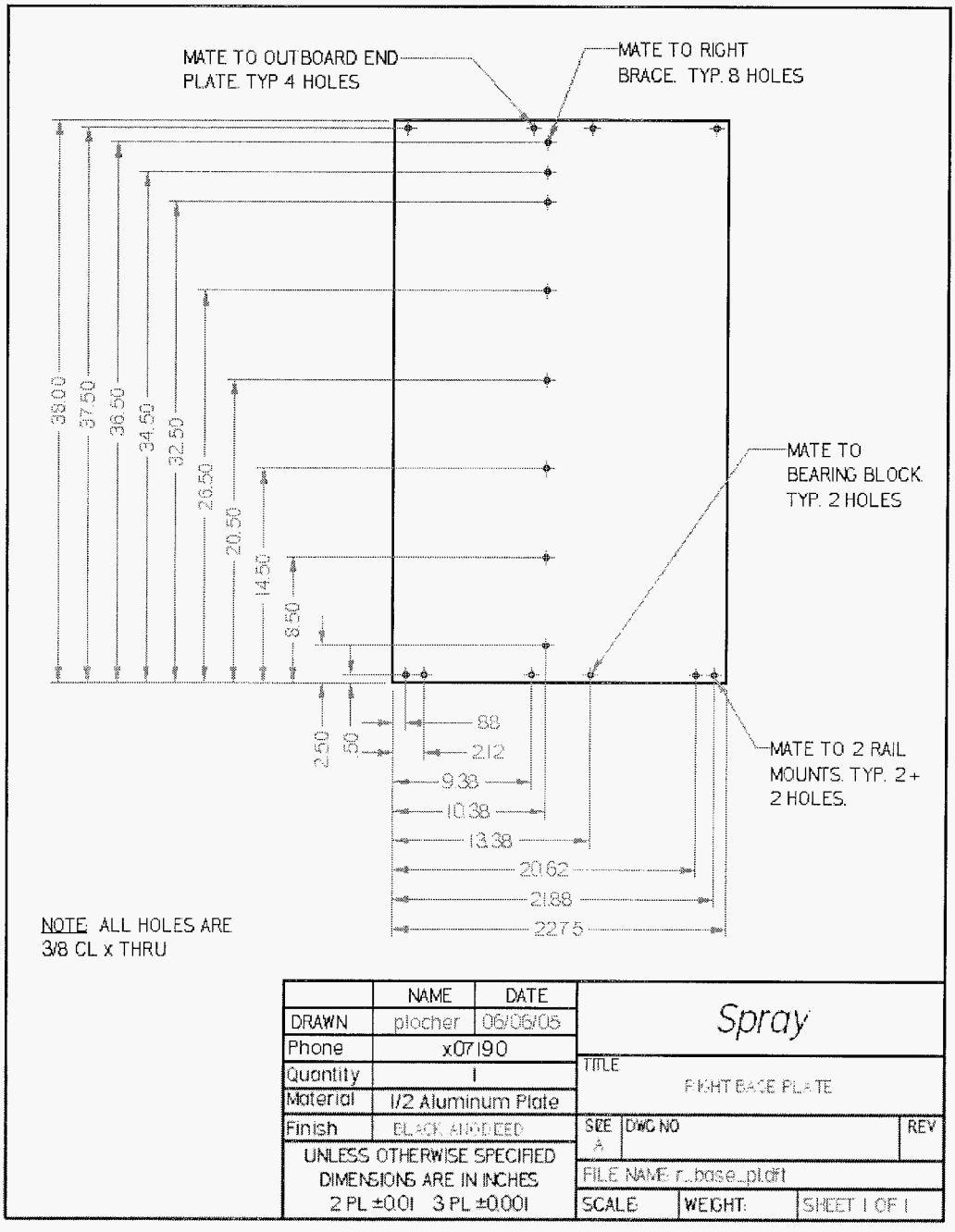

Figure 61. Right base plate

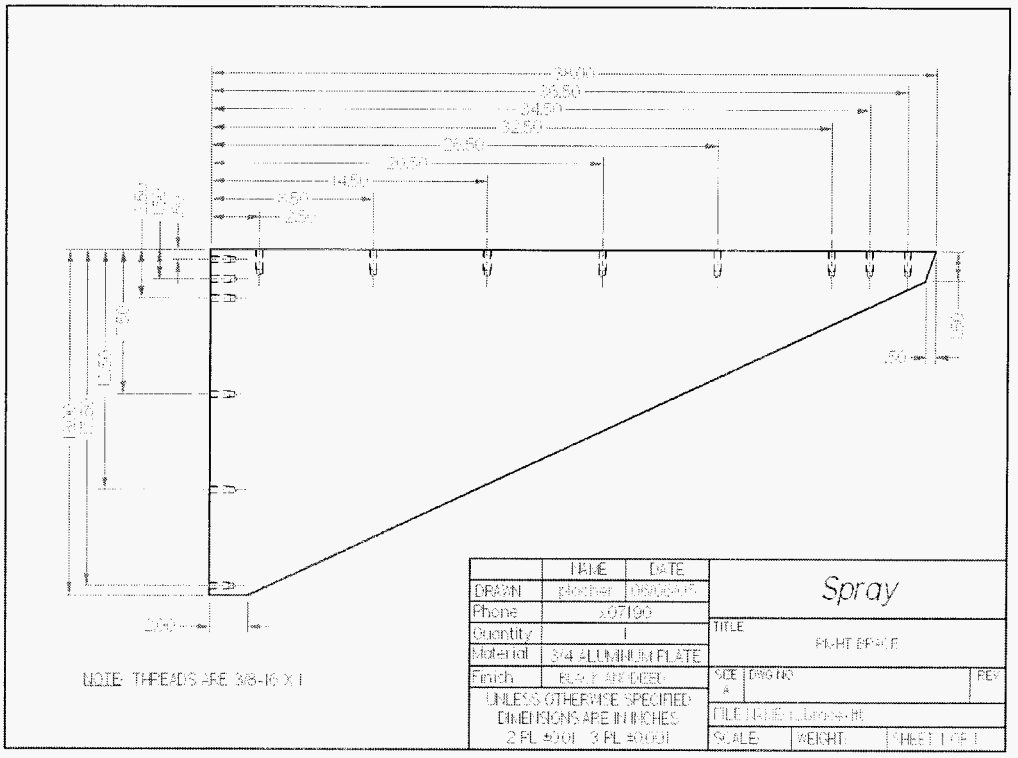

Figure 62. Right traverse brace

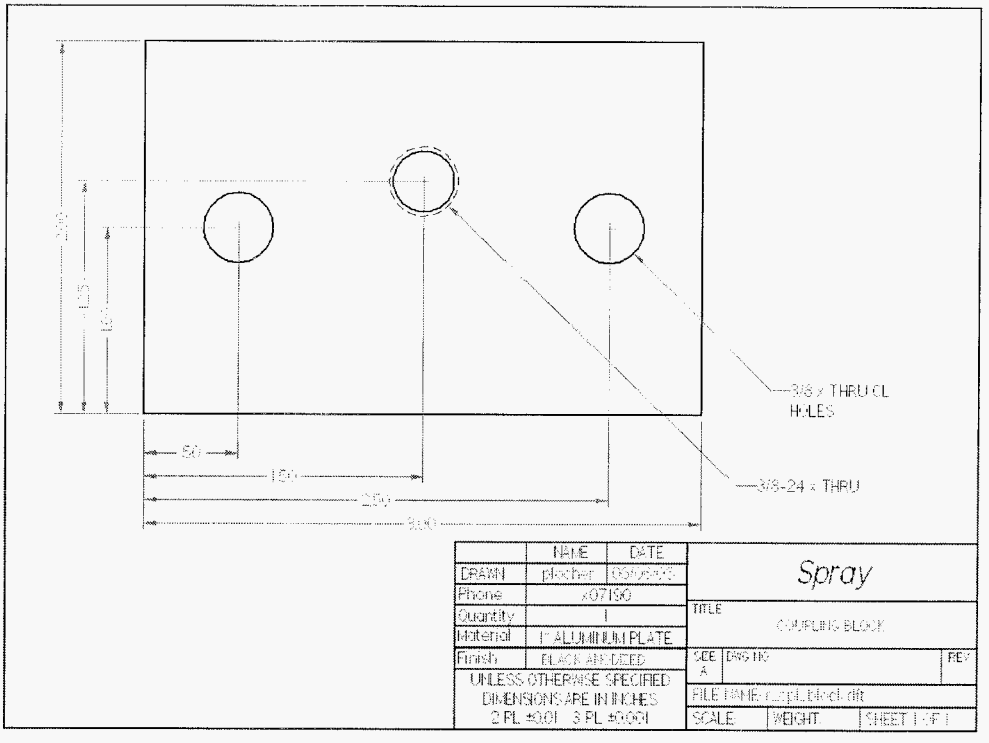

Figure 63. Load cell coupling block

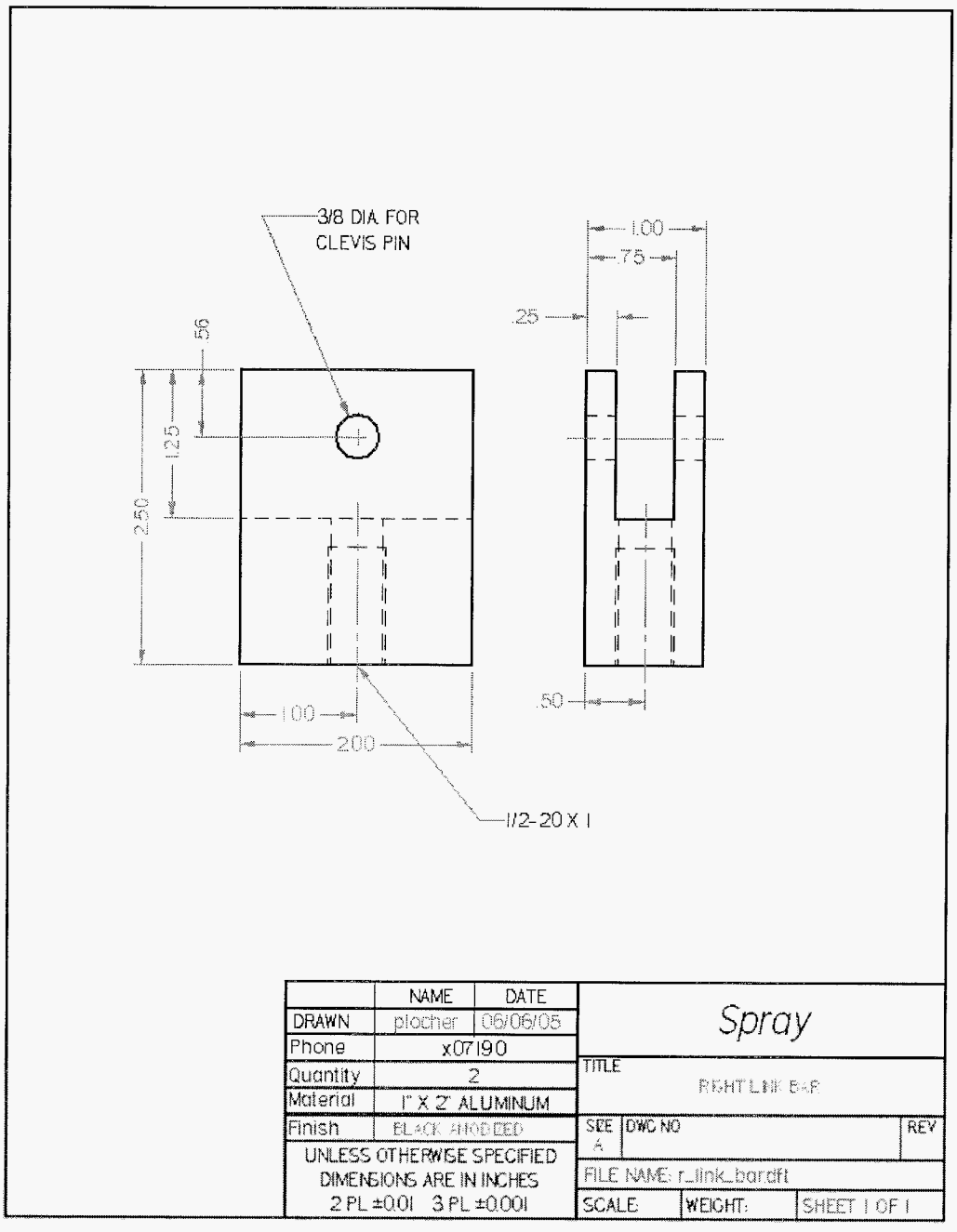

	NAME	DATE
DRAWN	plocher	06/06/05
Phone	x07190	
Quantity	2	
Material	1" X 2" ALUMINUM	
Finish	BLACK ANODIZED	
UNLESS OTHERWISE SPECIFIED DIMENSIONS ARE IN INCHES 2 PL ±0.01 3 PL ±0.001		

Spray

TITLE: RIGHT LINK BAR

SIZE A | DWG NO | REV

FILE NAME: r_link_bar.dft

SCALE: | WEIGHT: | SHEET 1 OF 1

Figure 64. Right link block for spring dampener

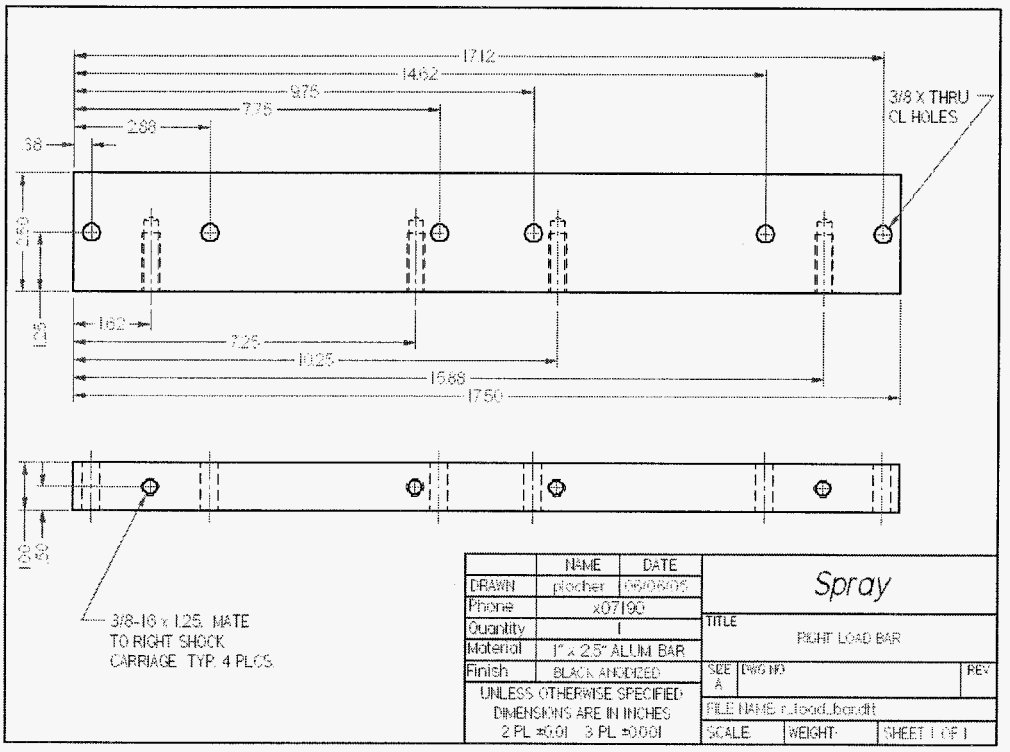

Figure 65. Right load bar

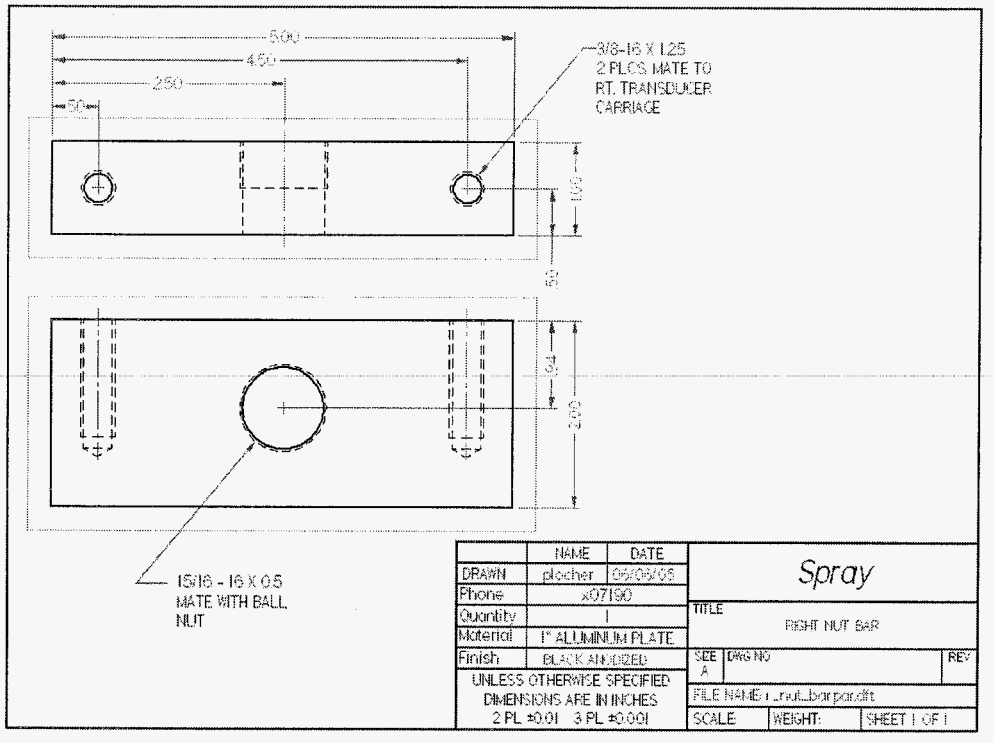

Figure 66. Right Nut bar

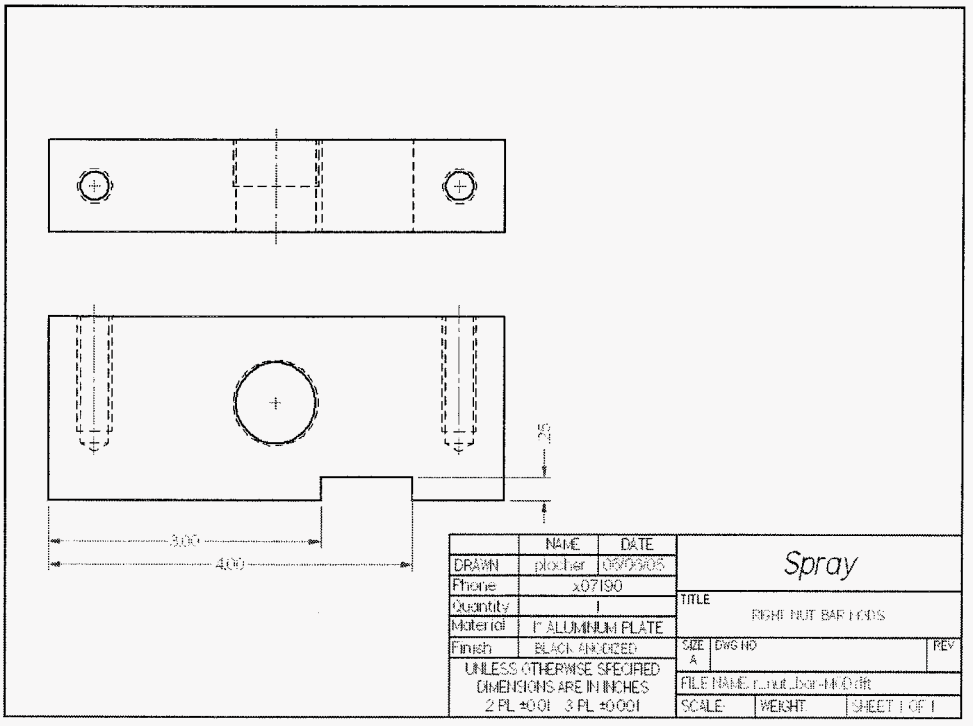

Figure 67. Right Nut bar with modifications

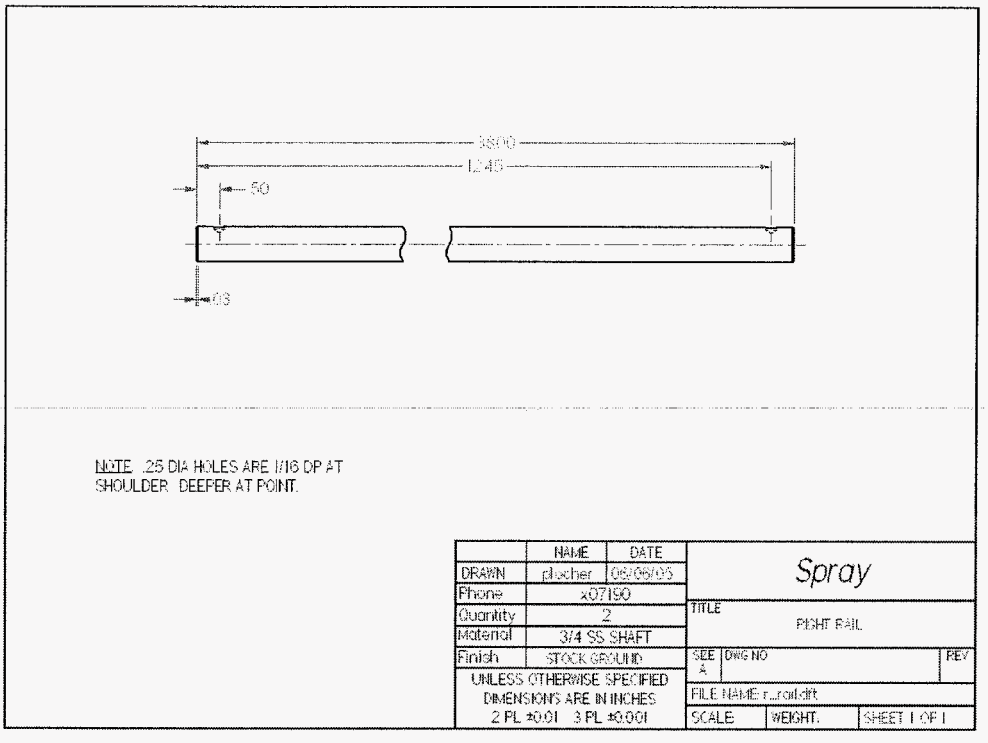

Figure 68. Right rail.

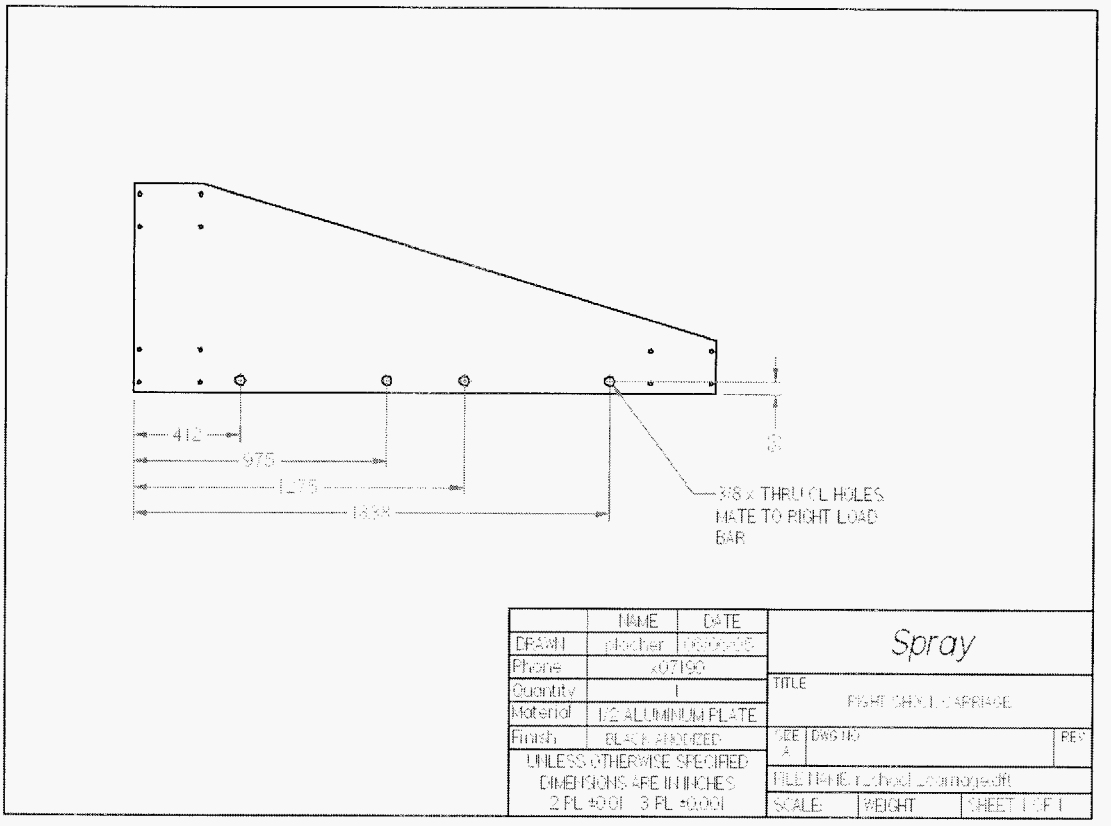

Figure 69. Right carriage where shocks mount

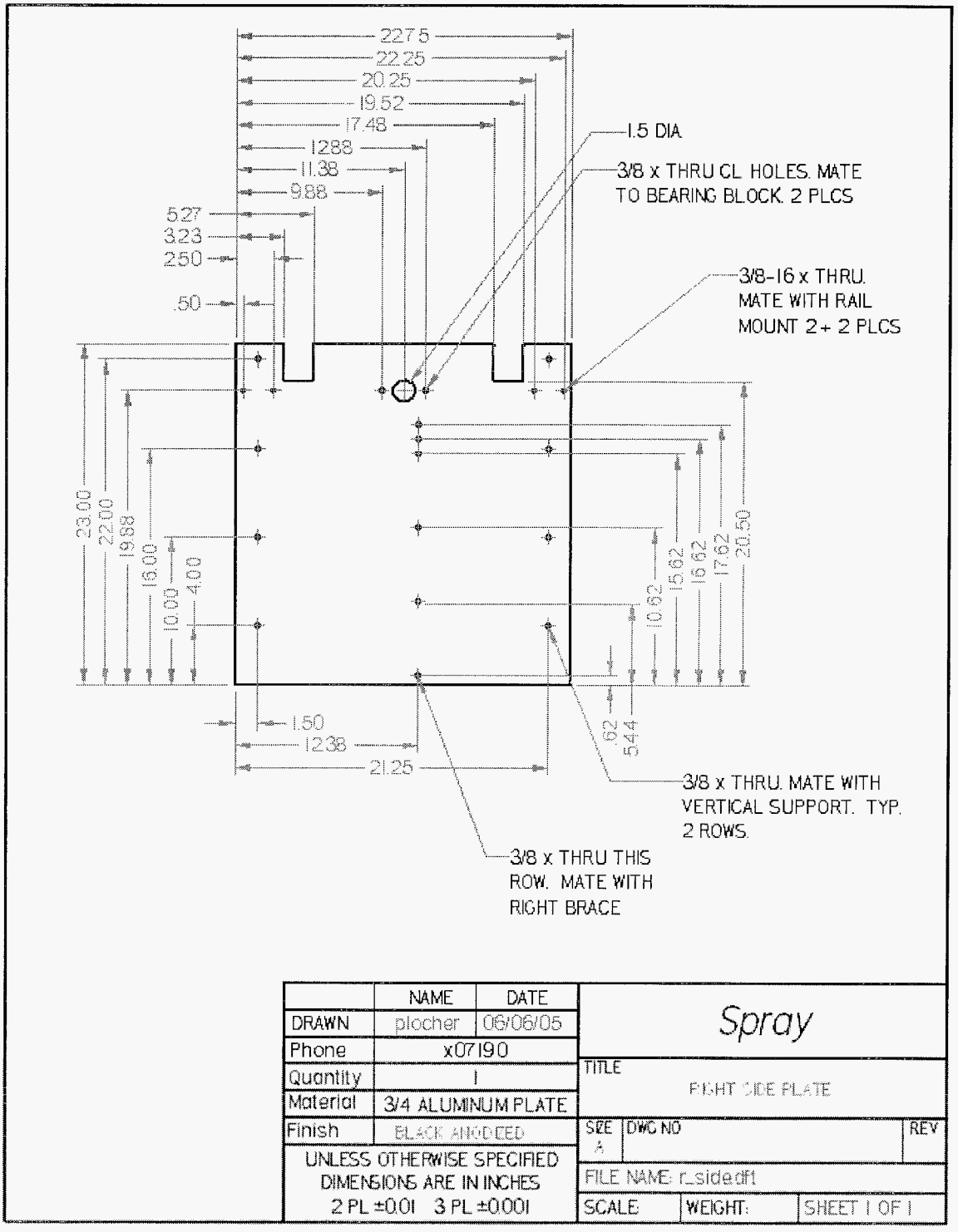

Figure 70. Right side mounting plate

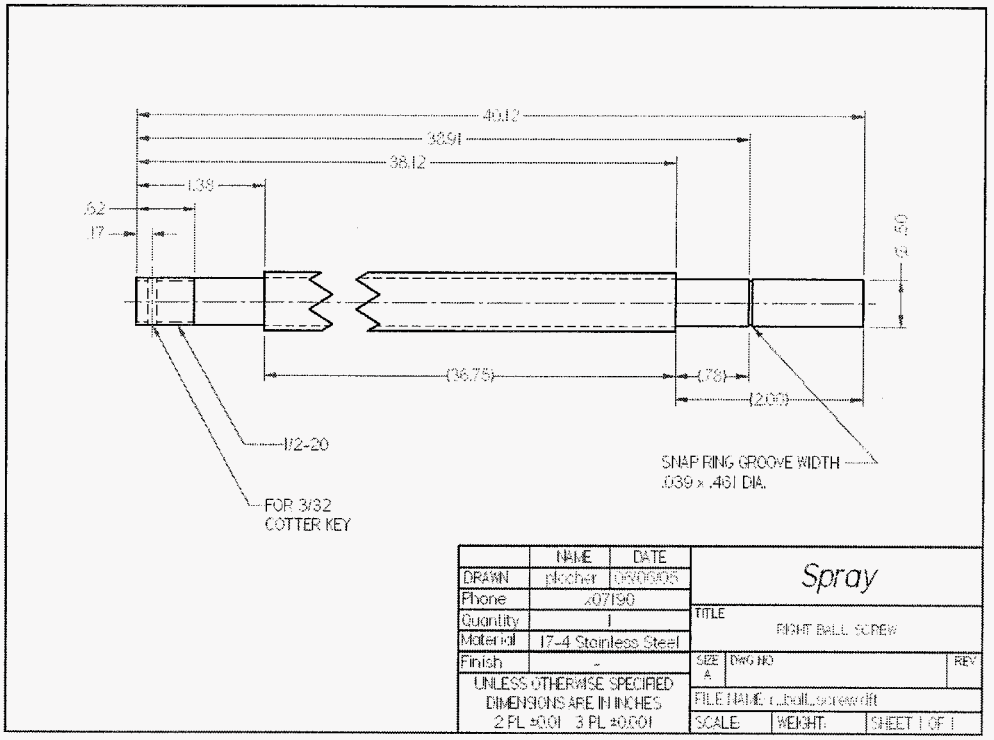

Figure 71. Ball screw for right side

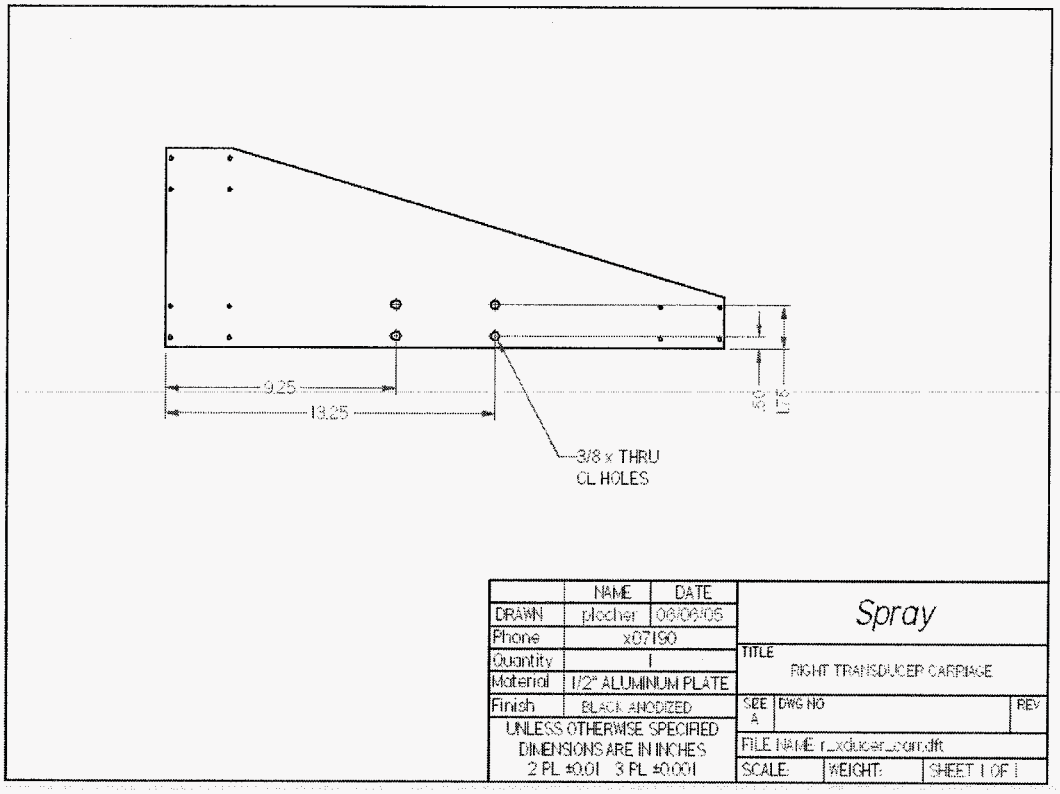

Figure 72. Transducer carriage

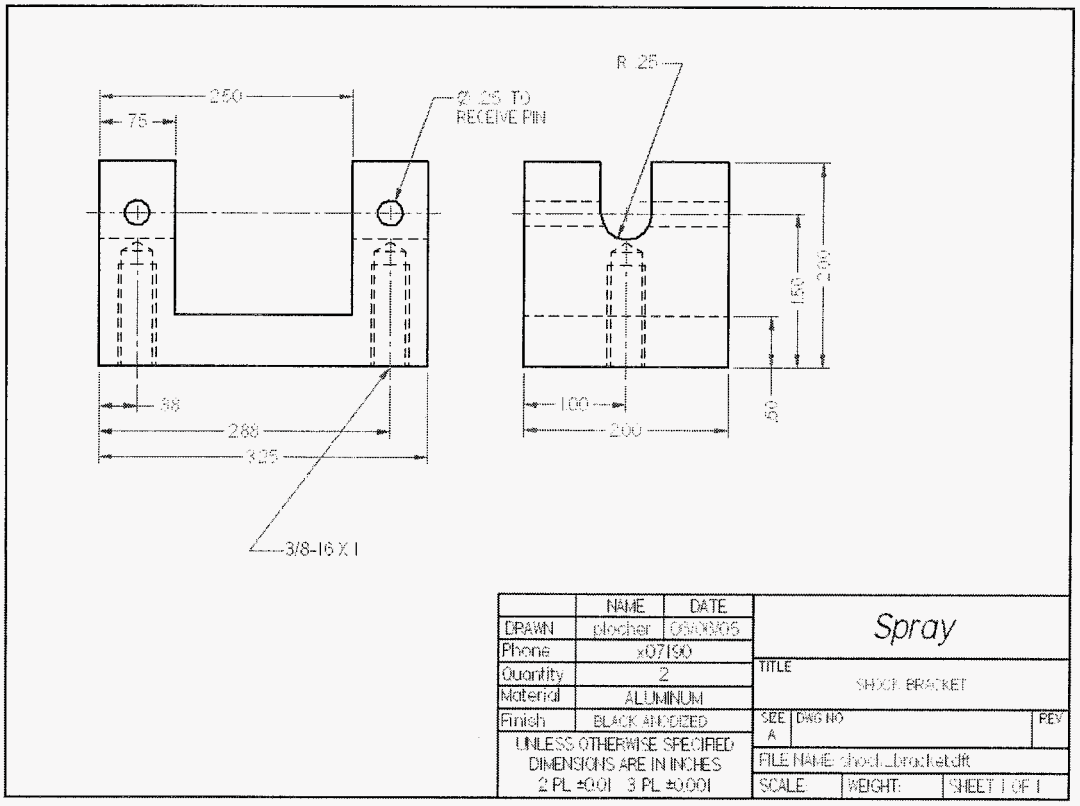

Figure 73. Bracket for mounting shocks

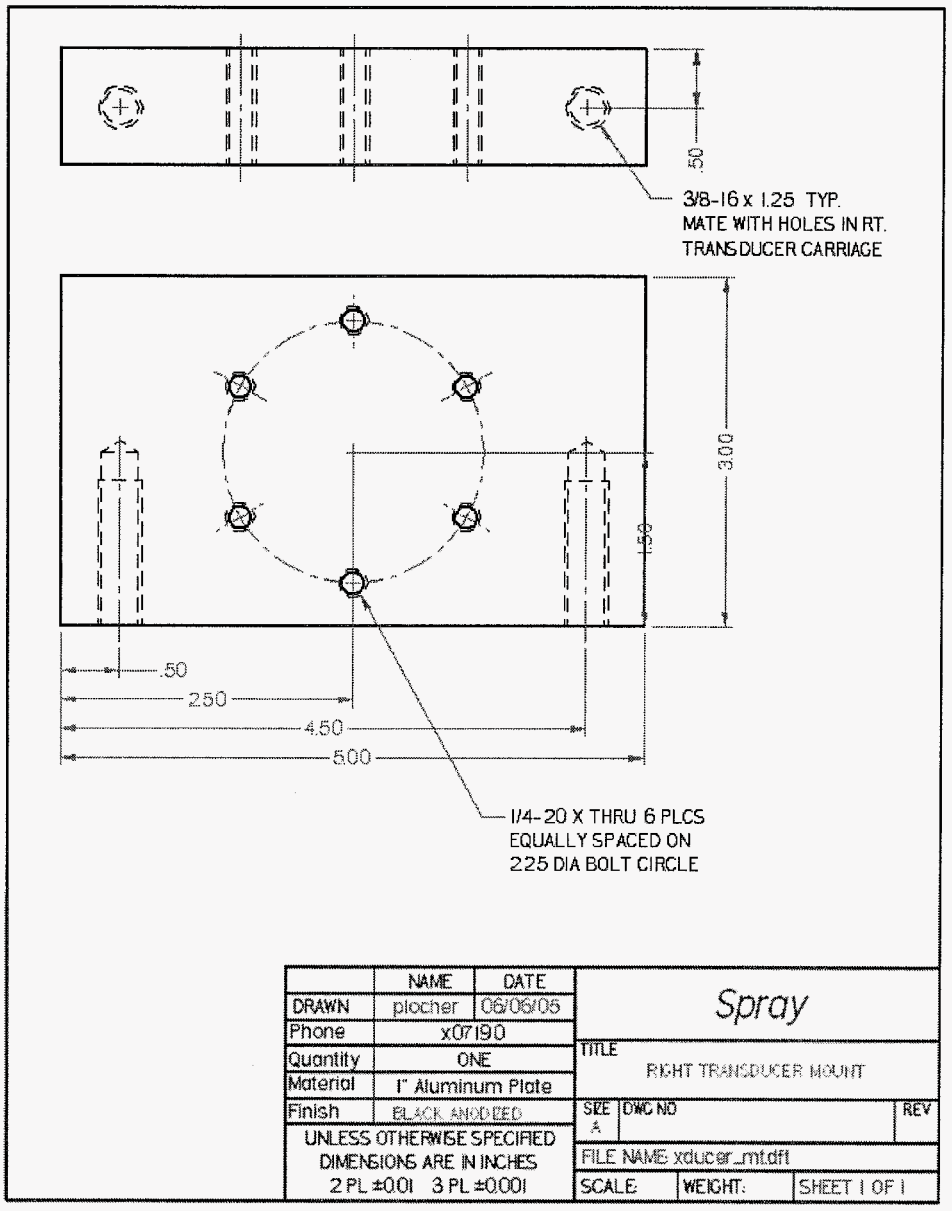

Figure 74. Transducer mount

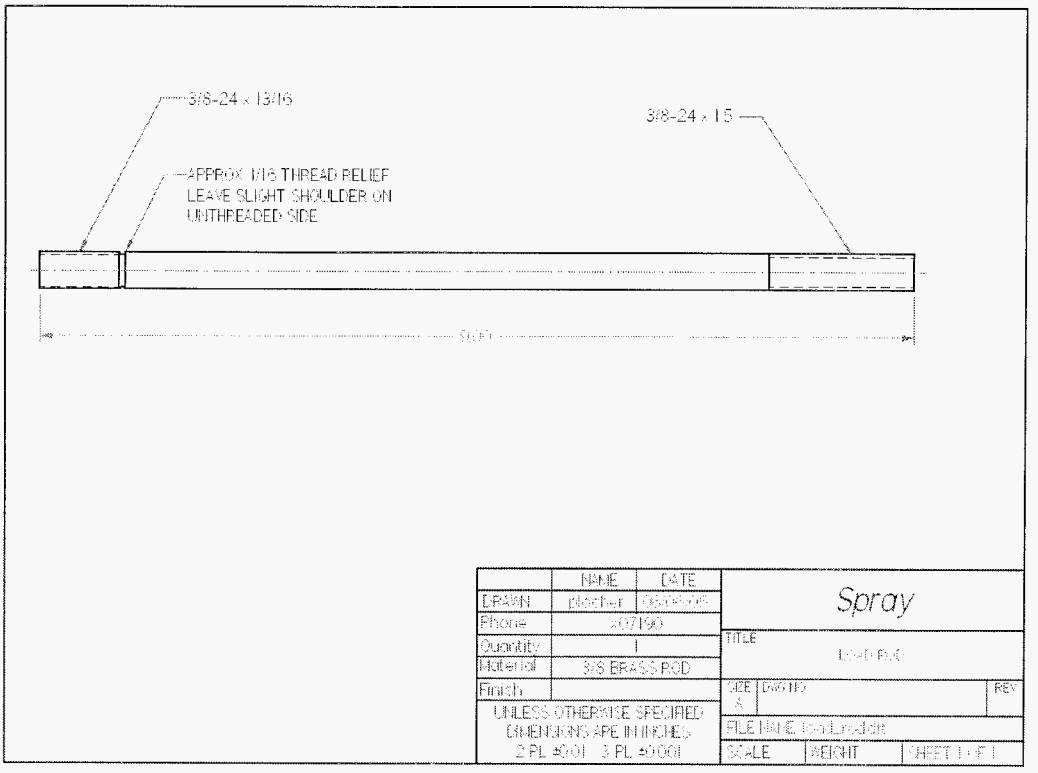

Figure 75. Load rod for the transducer

Jet Canister Supports

Included is the supporting frame for the jet canister.

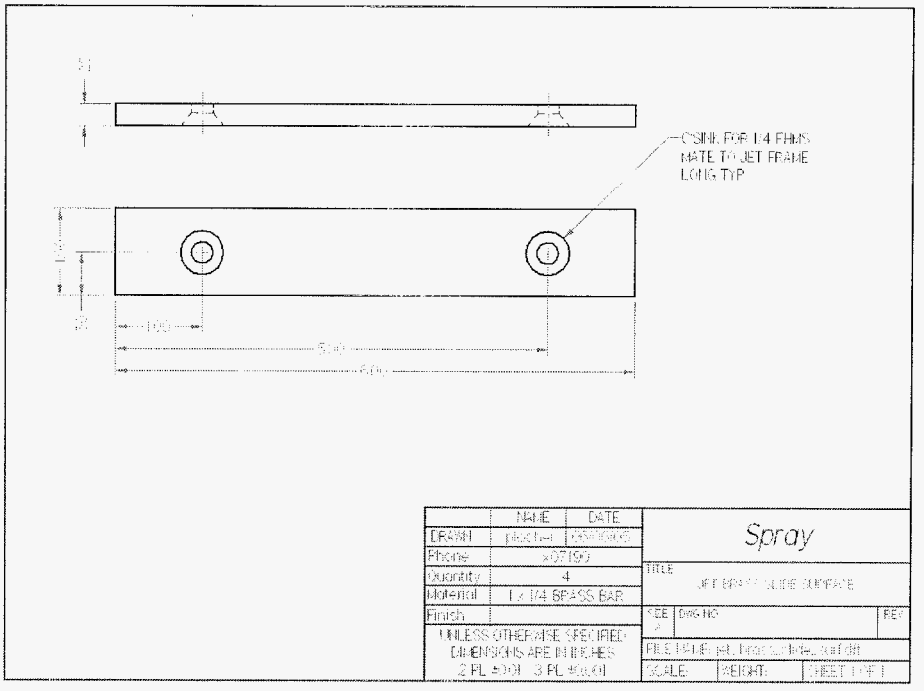

Figure 76. Brass surface for mounting canister

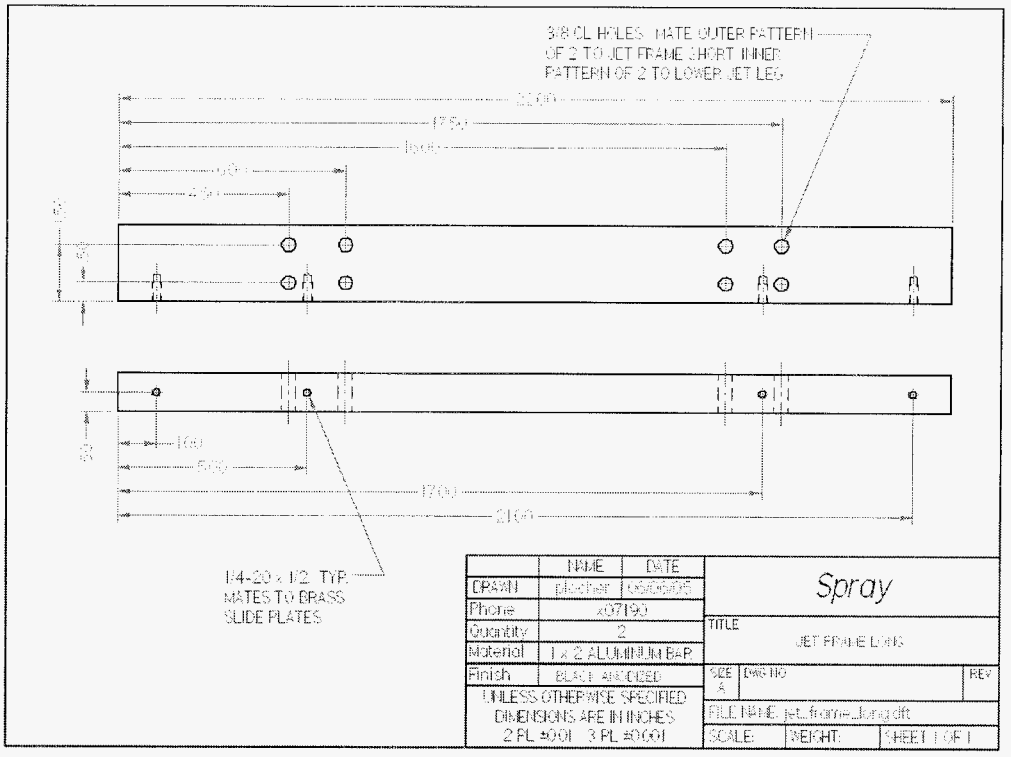

Figure 77. Canister frame support

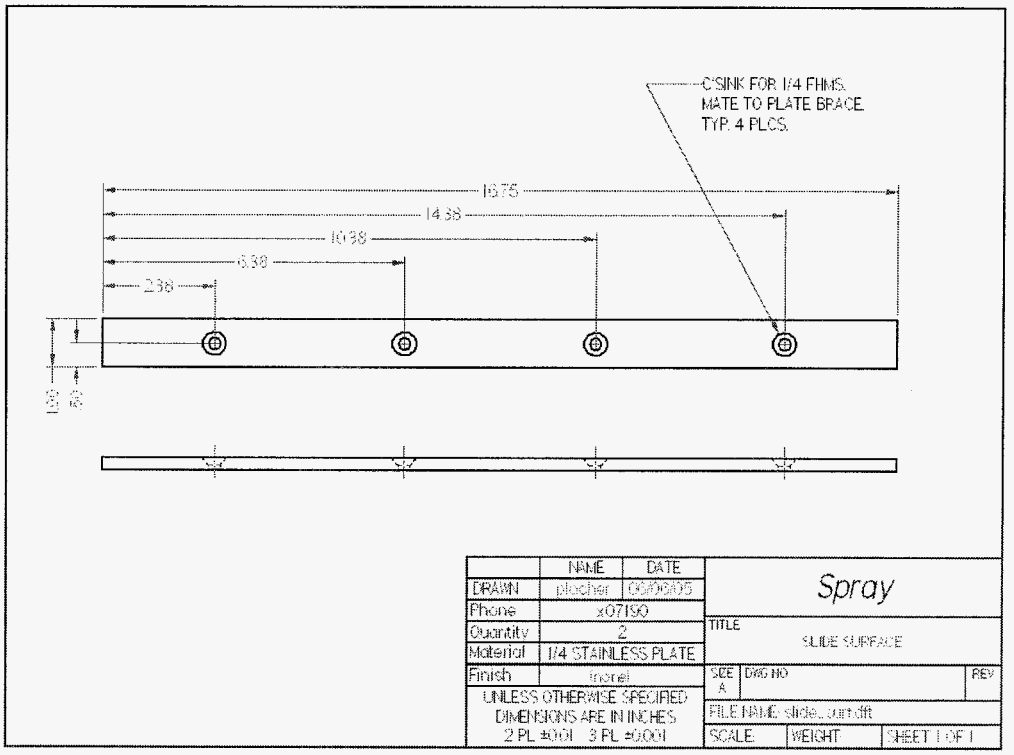

Figure 78. Slide surface

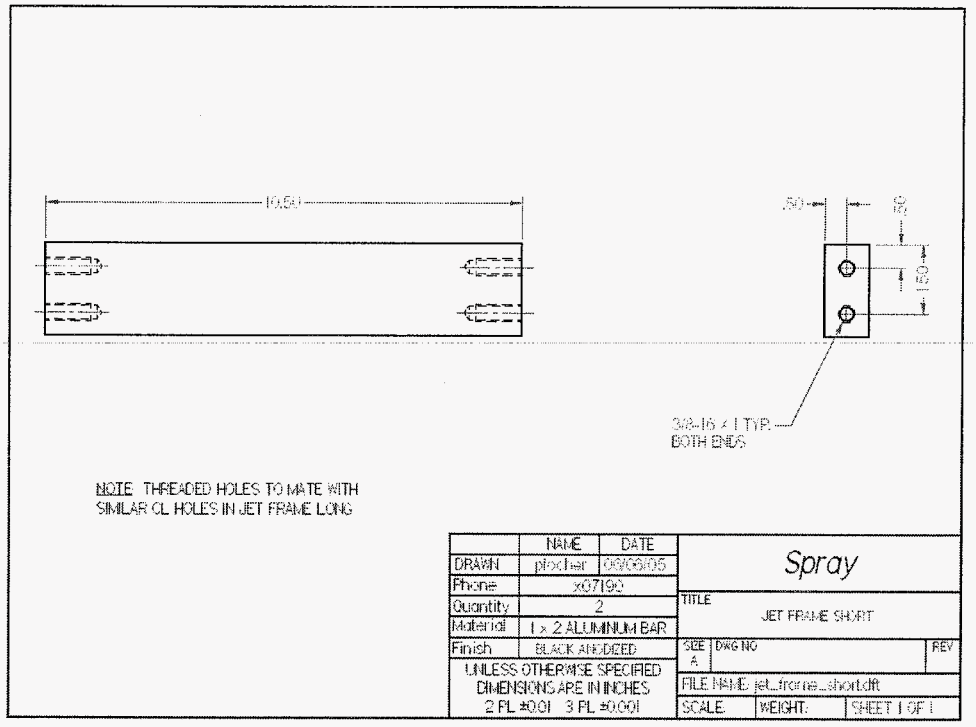

Figure 79. Canister frame short support

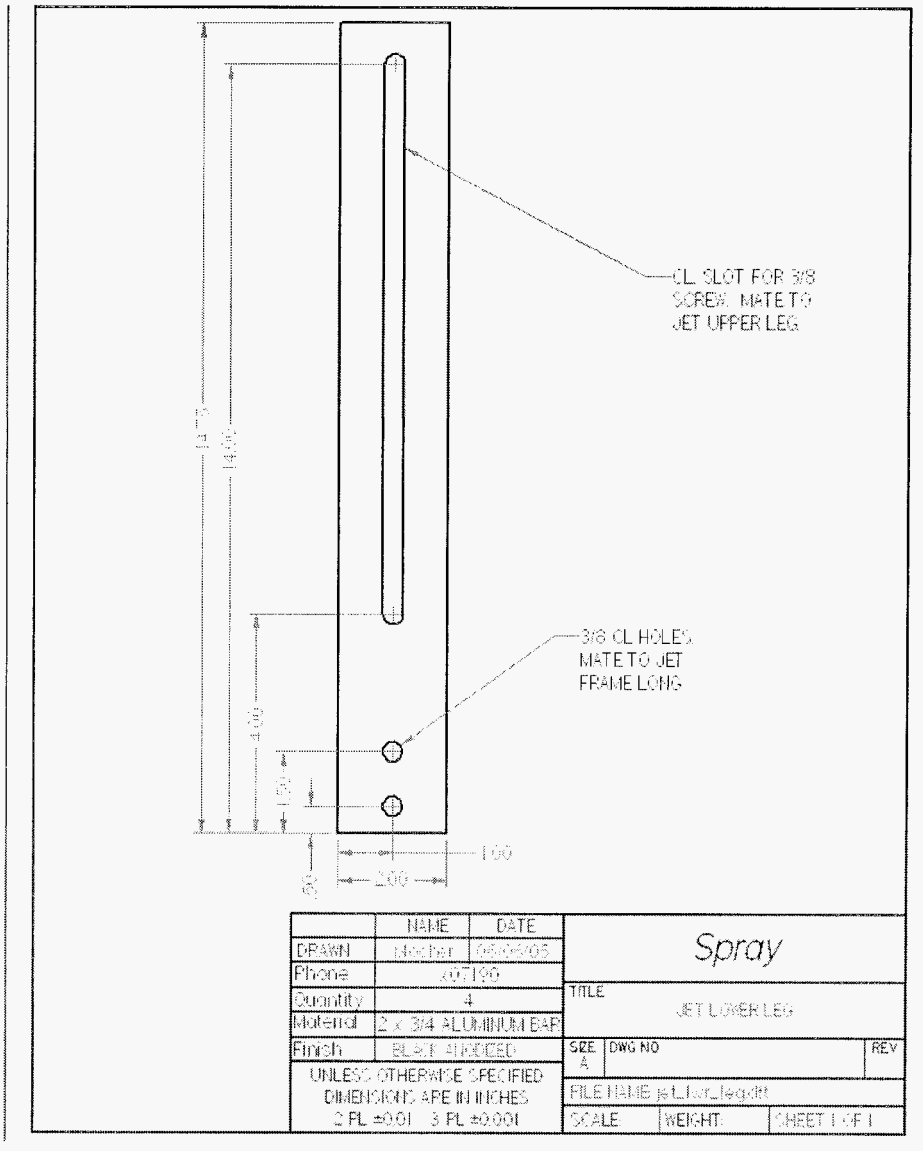

Figure 80. Canister vertical lower support

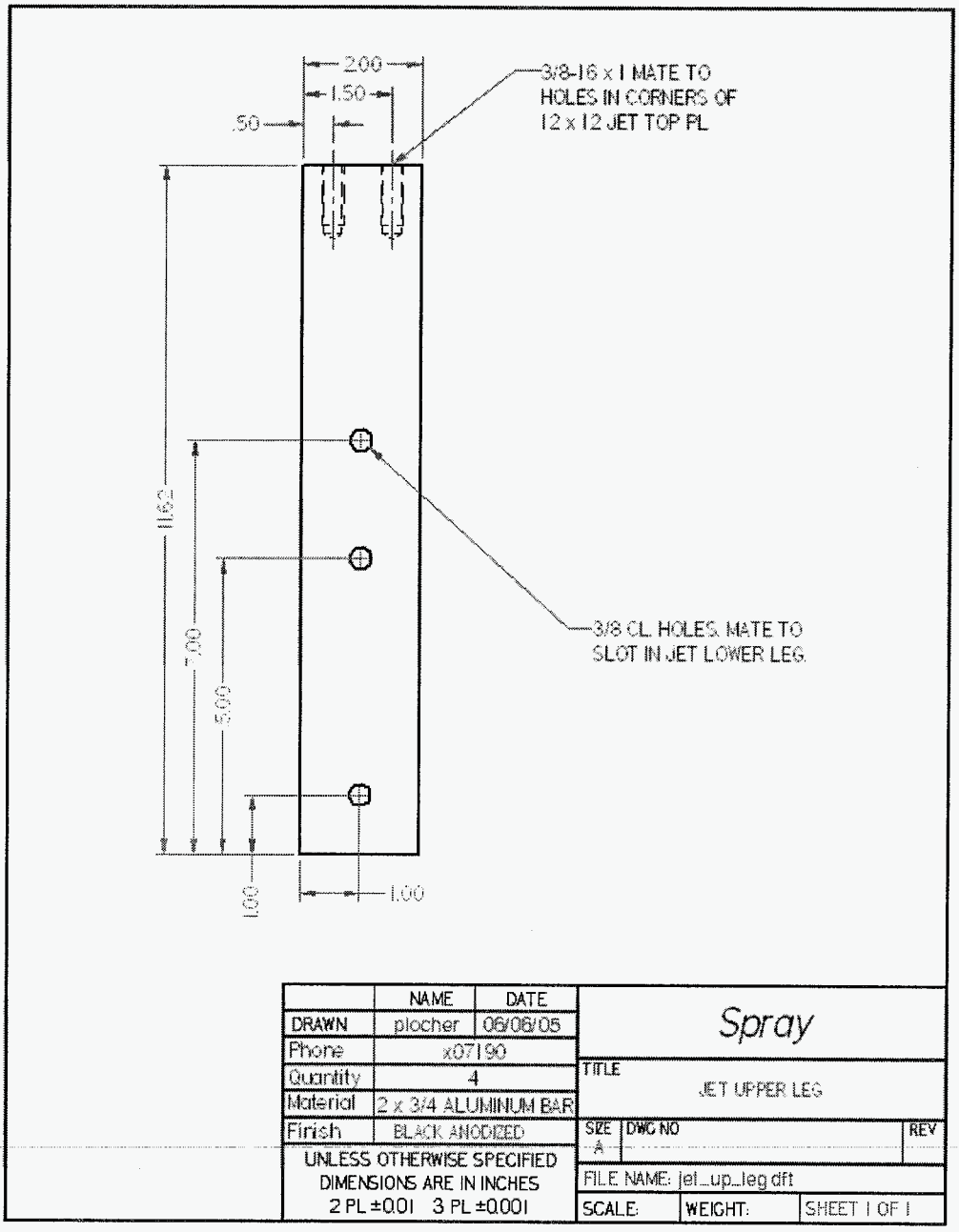

Figure 81. Canister vertical upper support

Canister and Gate

Included in the following sections are part drawings for the gate and water delivery system.

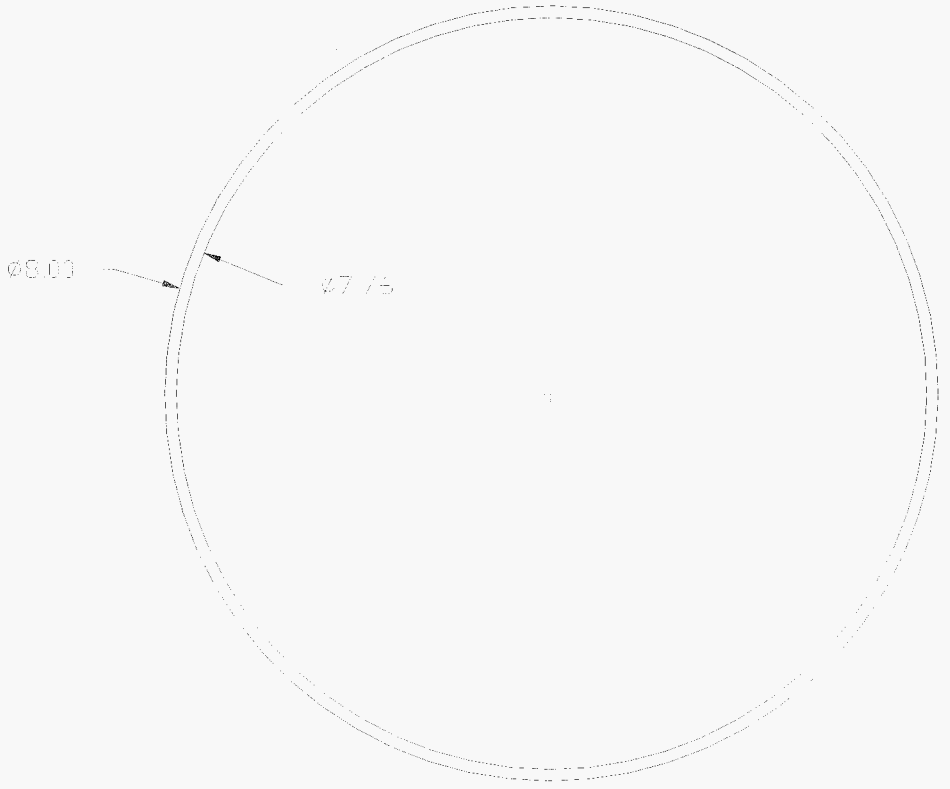

Figure 82. Stainless steel vacuum grade tube. Wall thickness = 0.12" Length = 24"

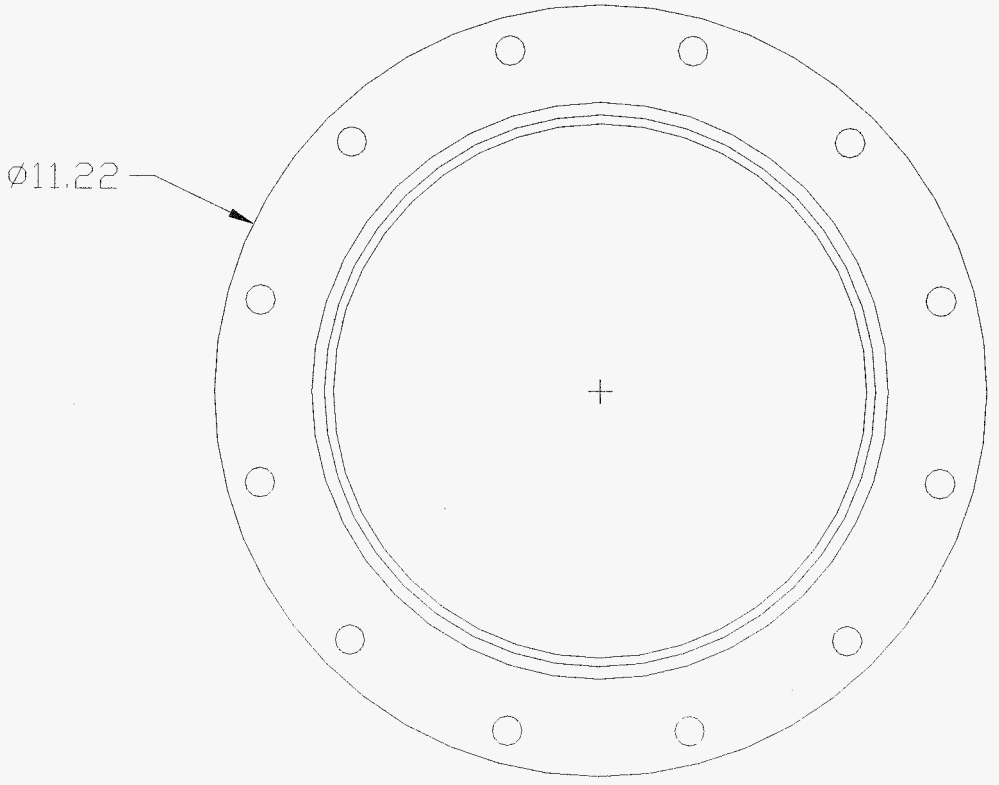

Figure 83. Flange fitting. Holes align with top or bottom cap (shown on next page) This part is welded to each end of the tube

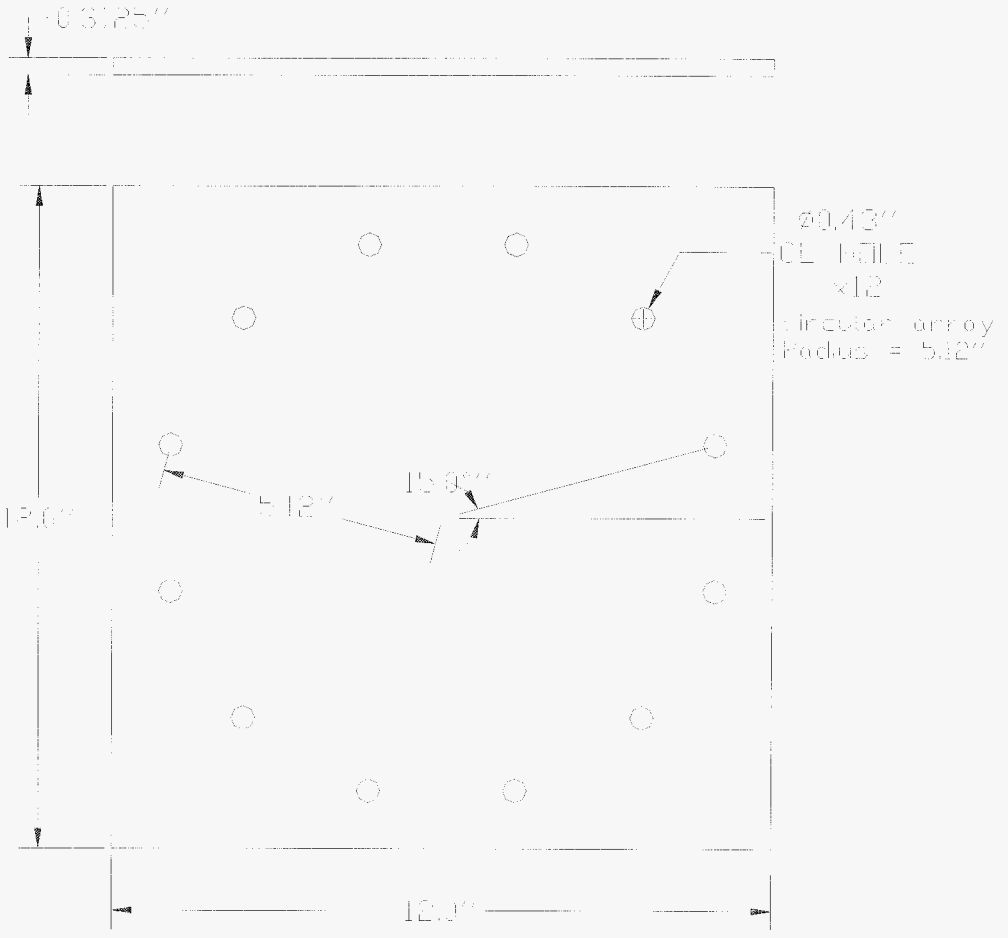

Figure 84. The top cap. Mounts to the flanges.

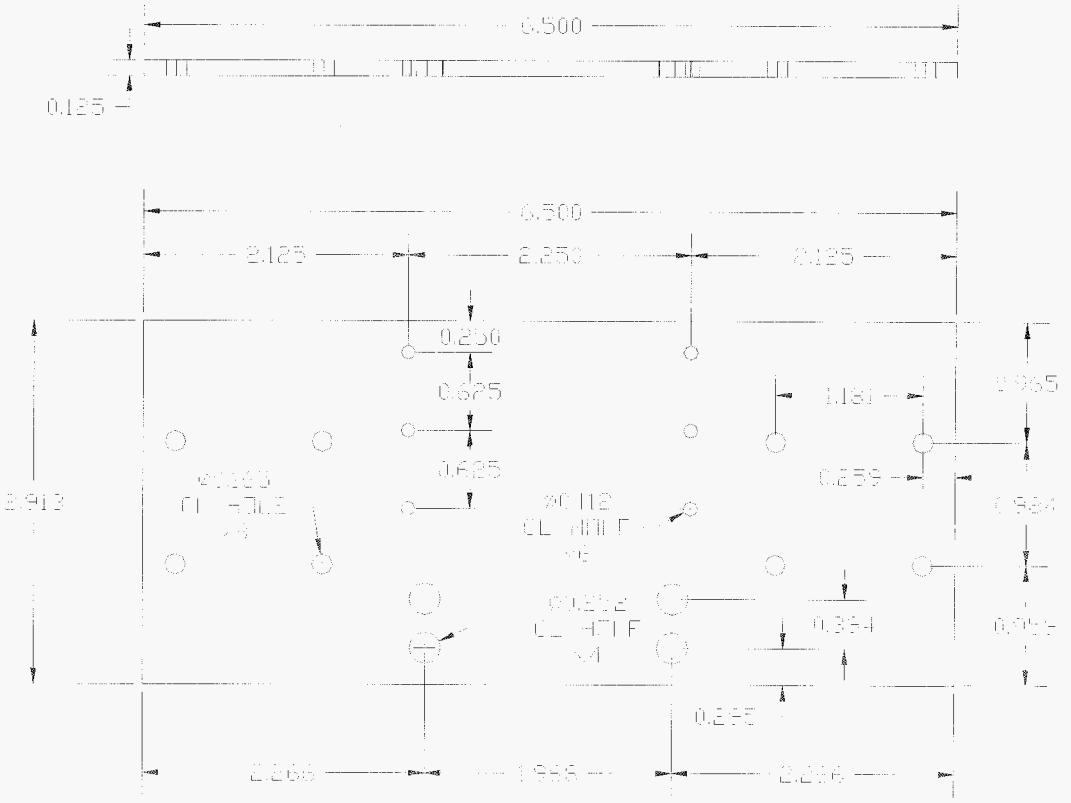

Figure 85. The guide plate for mounting the gate parts on the rails

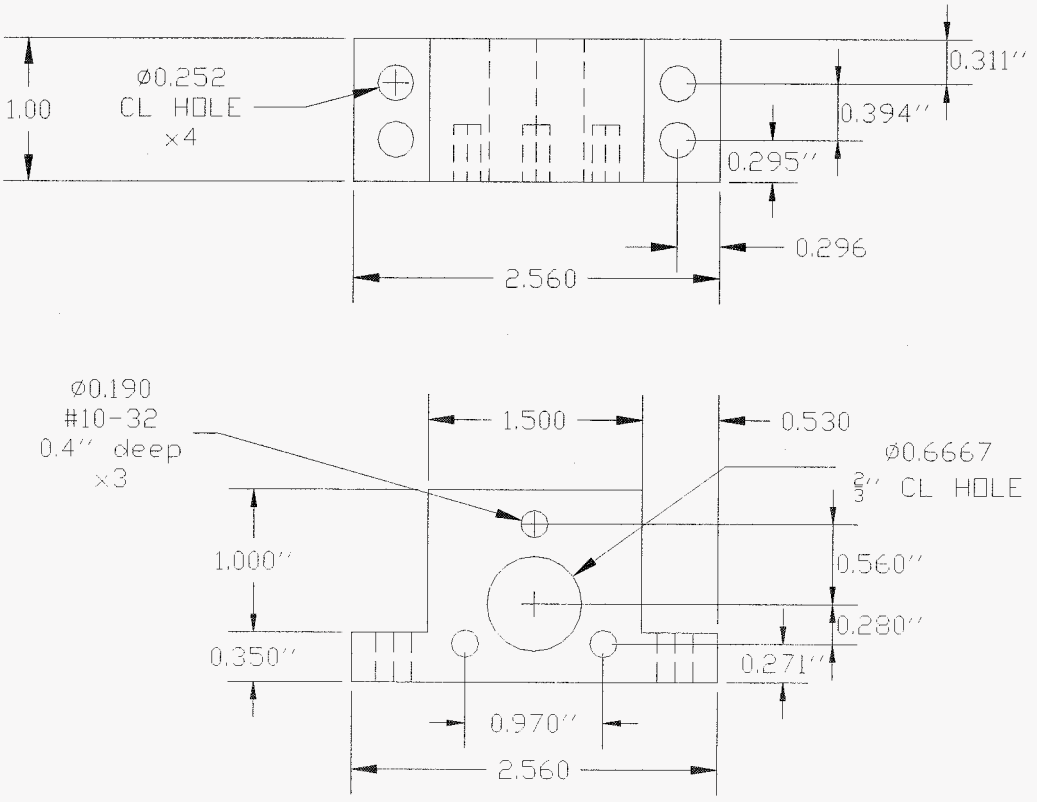

Figure 86. Lead block. Allows motion of the lead screw to be transferred to the gate.

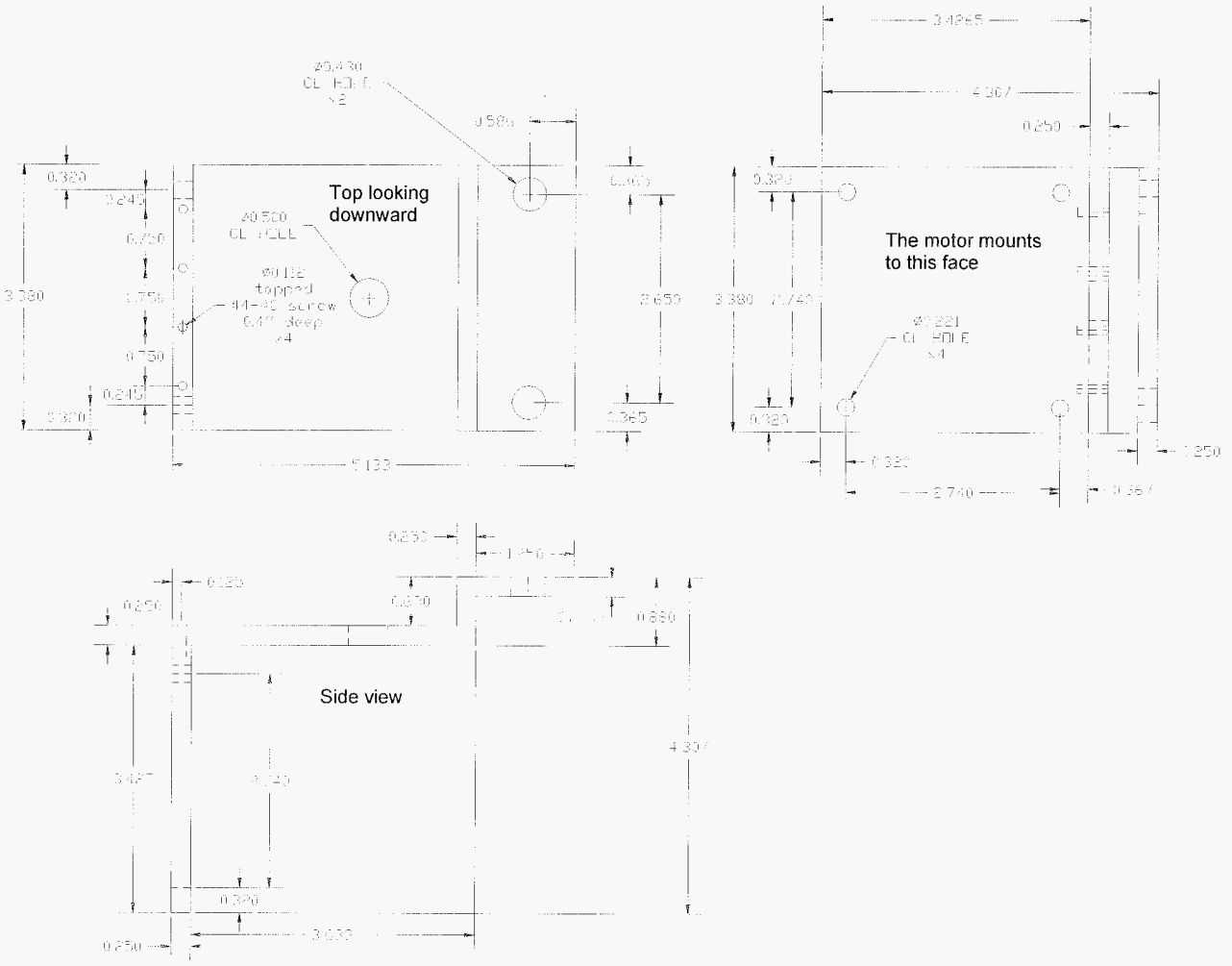

Figure 87. Motor mount (assembly) for attaching stepper motor to canister.

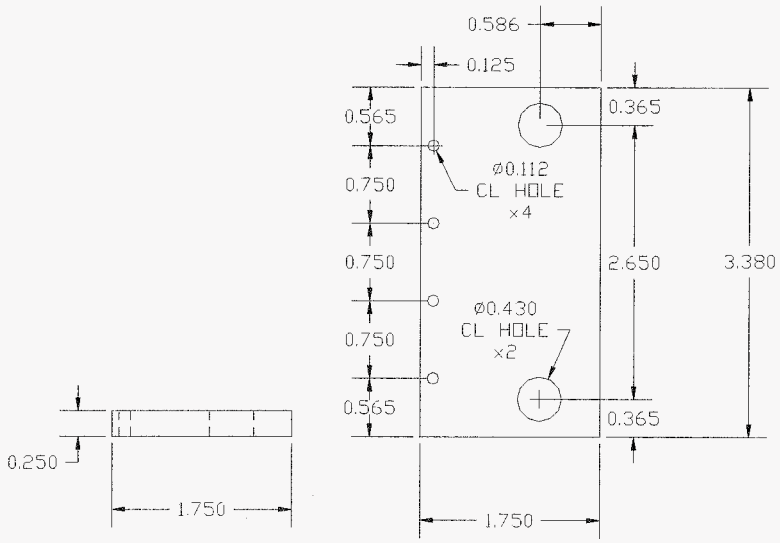

Figure 88. Stepper motor mount, part 1

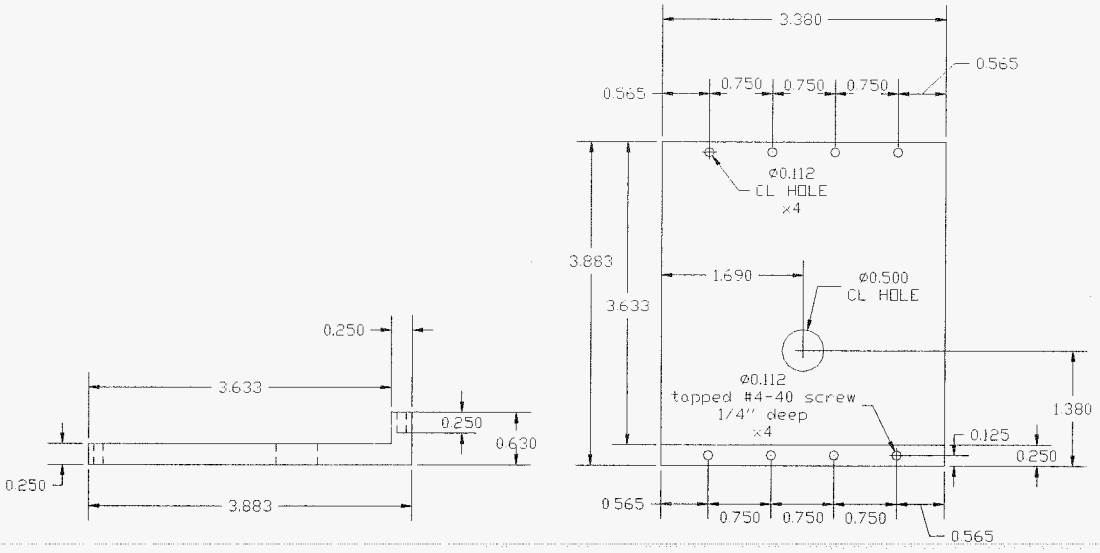

Figure 89. Stepper motor mount part 2

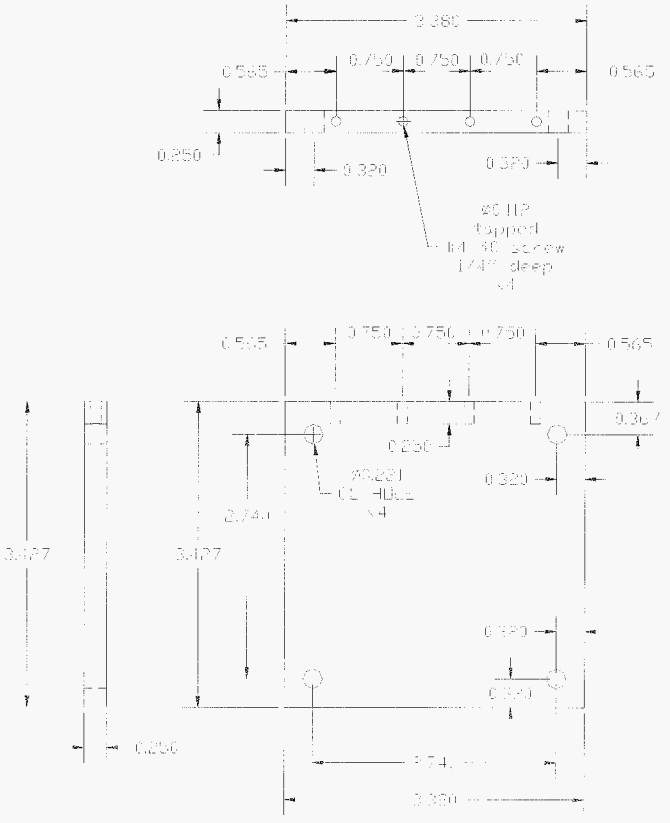

Figure 90. Stepper motor mount part 3

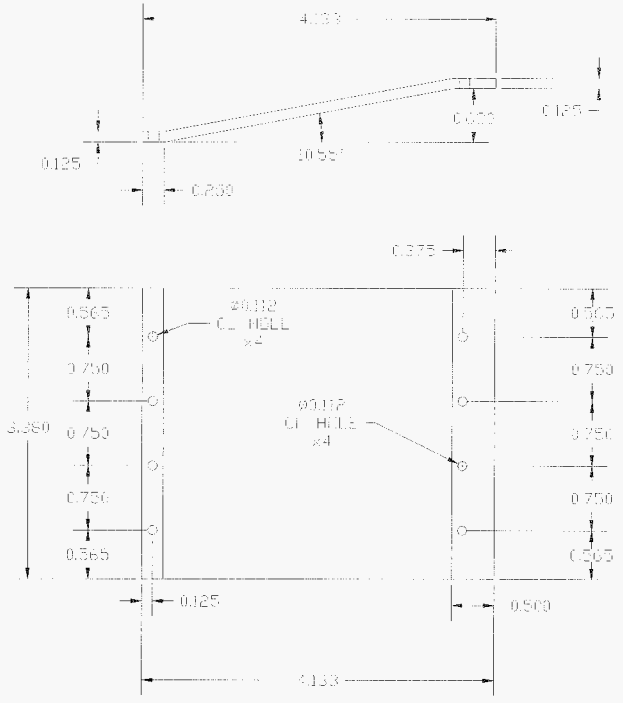

Figure 91. Bracket for attaching to motor

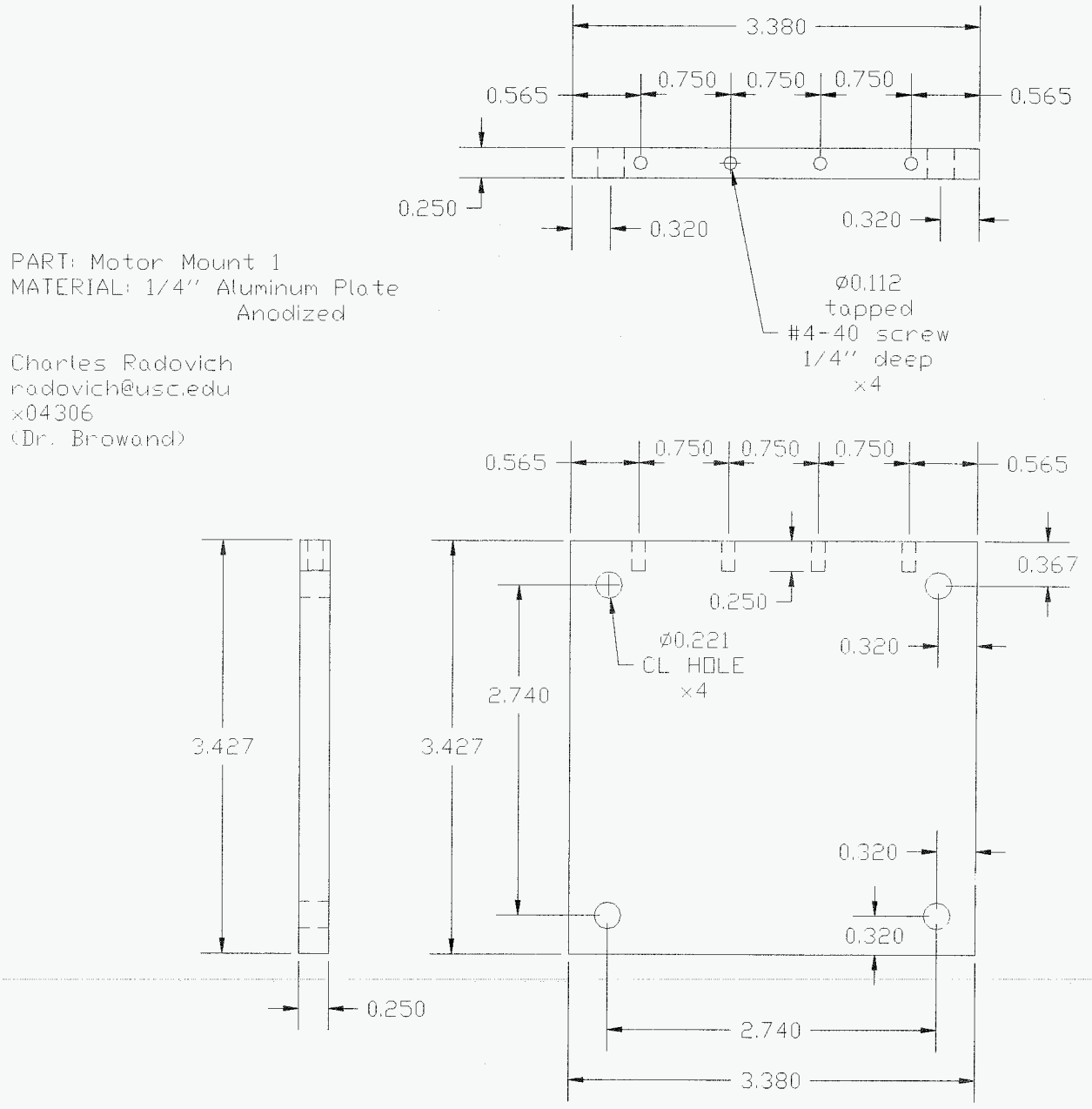

Figure 92. Plate for motor mount 1

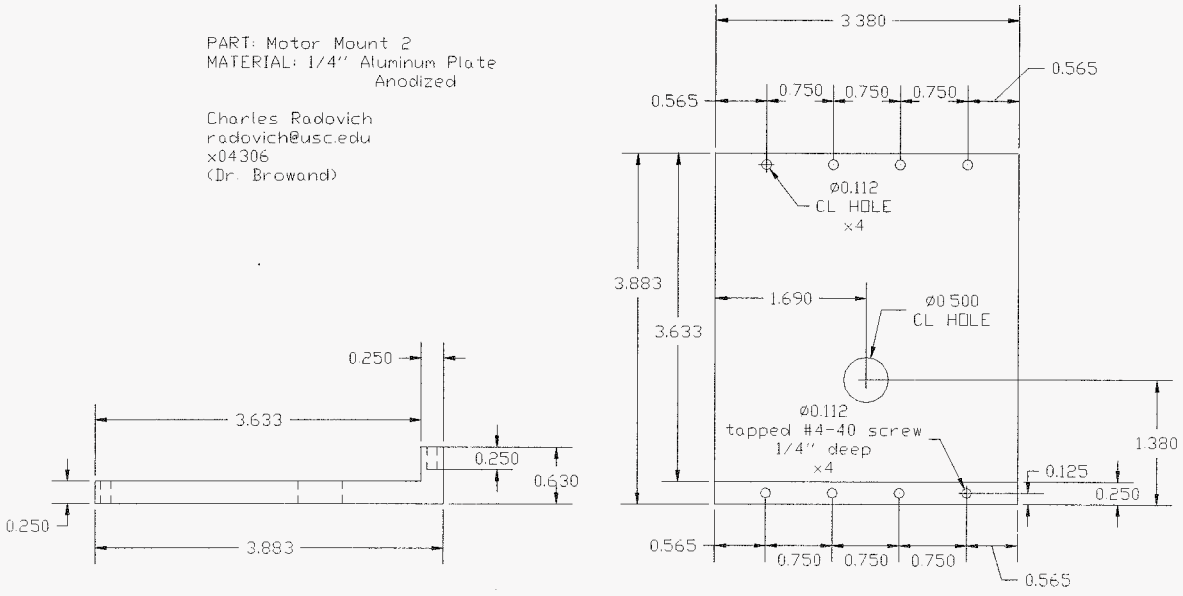

Figure 93. Plate for motor mount 2

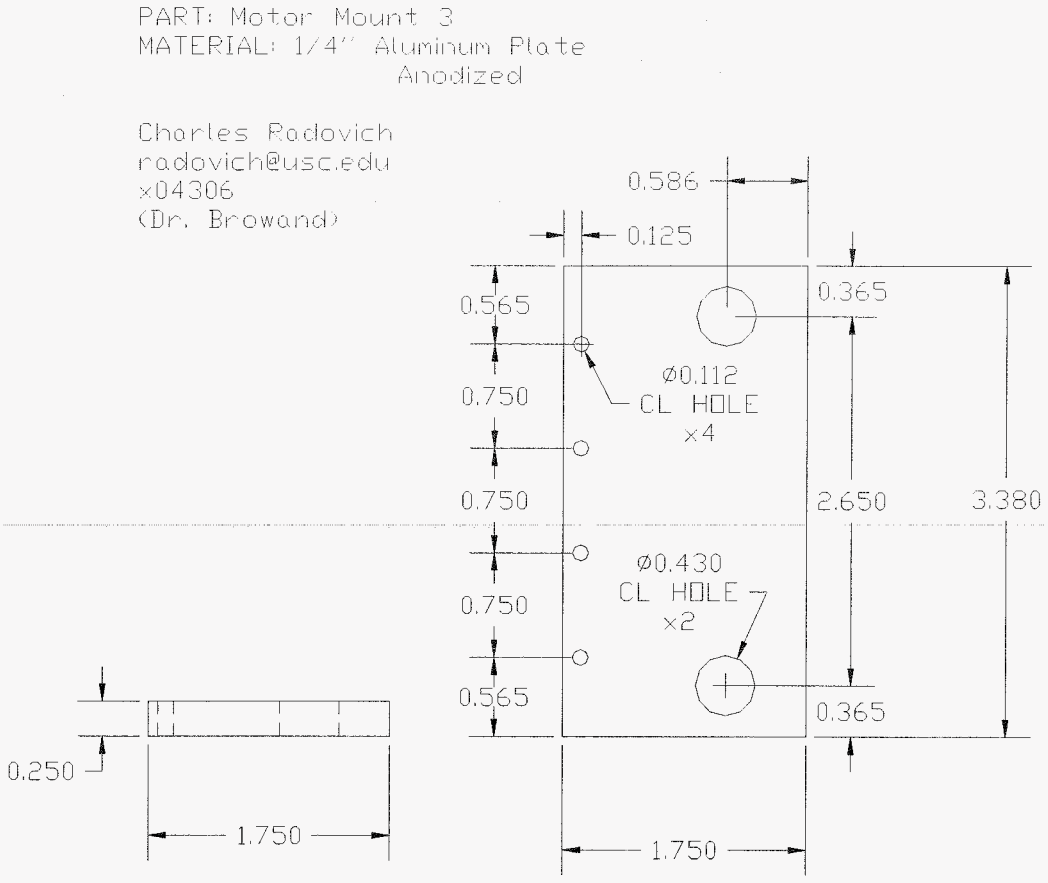

Figure 94. Plate for motor mount 3

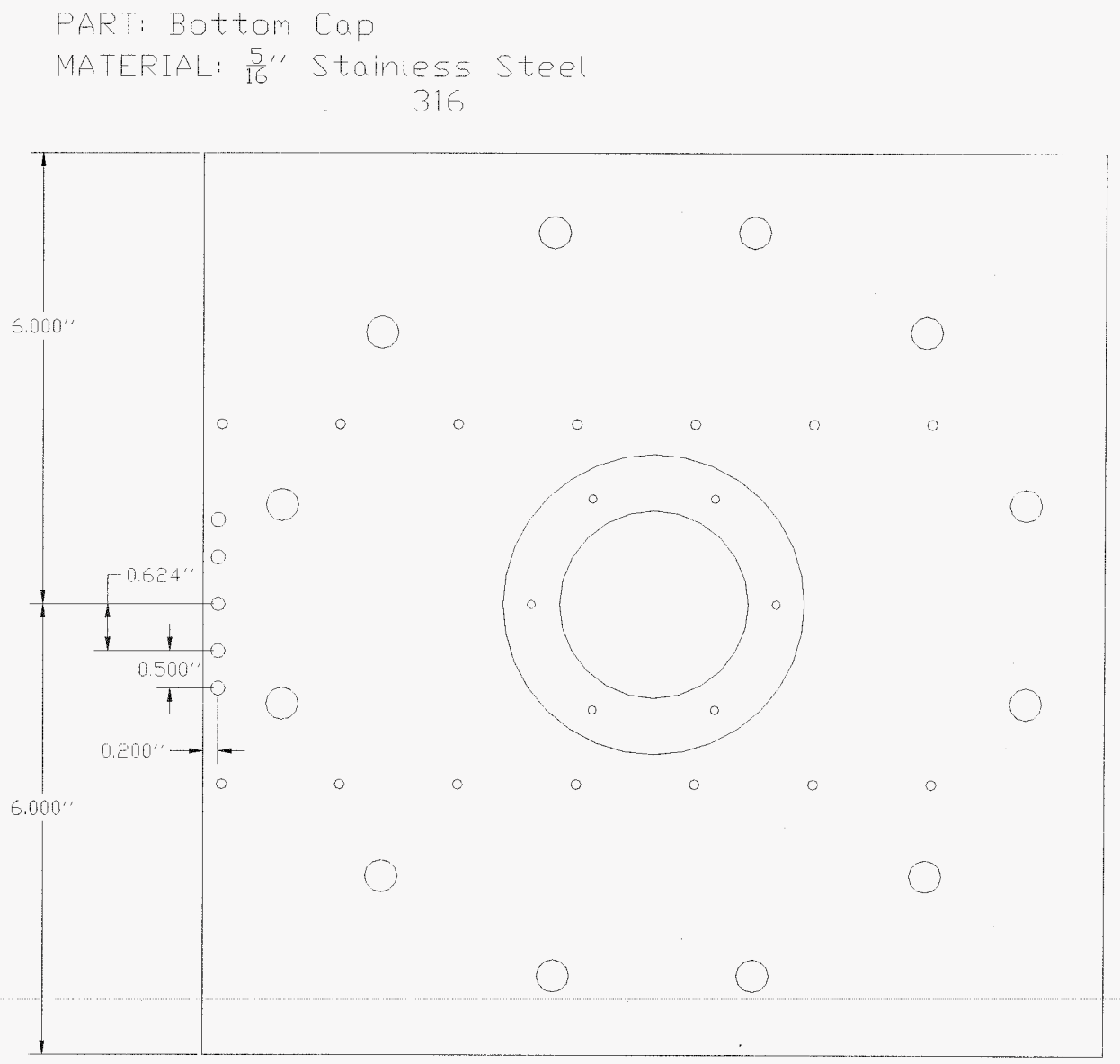

Figure 95. Bottom Cap. Stainless steel. Houses the nozzle.

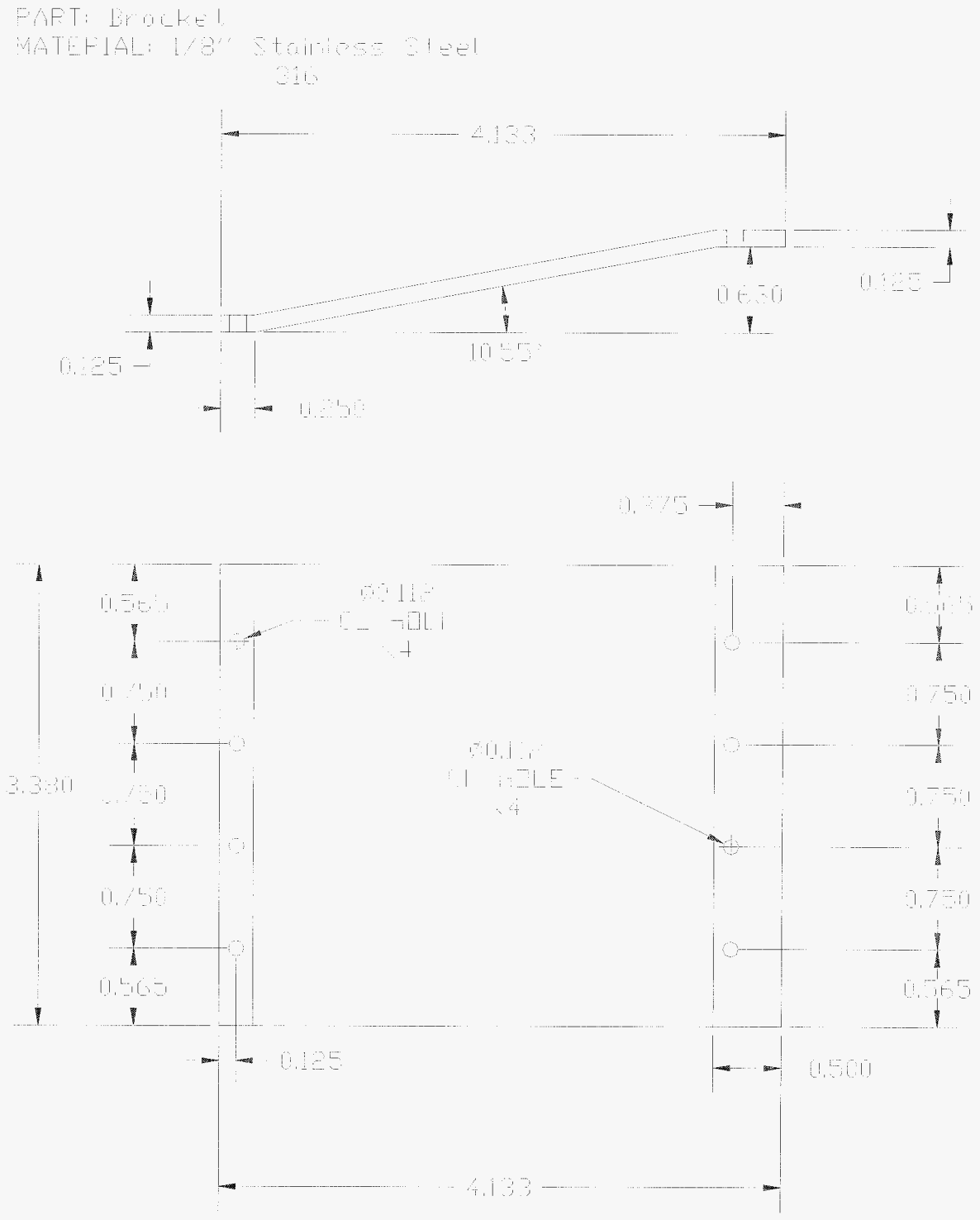

Figure 96. Stainless steel motor mounting bracket.

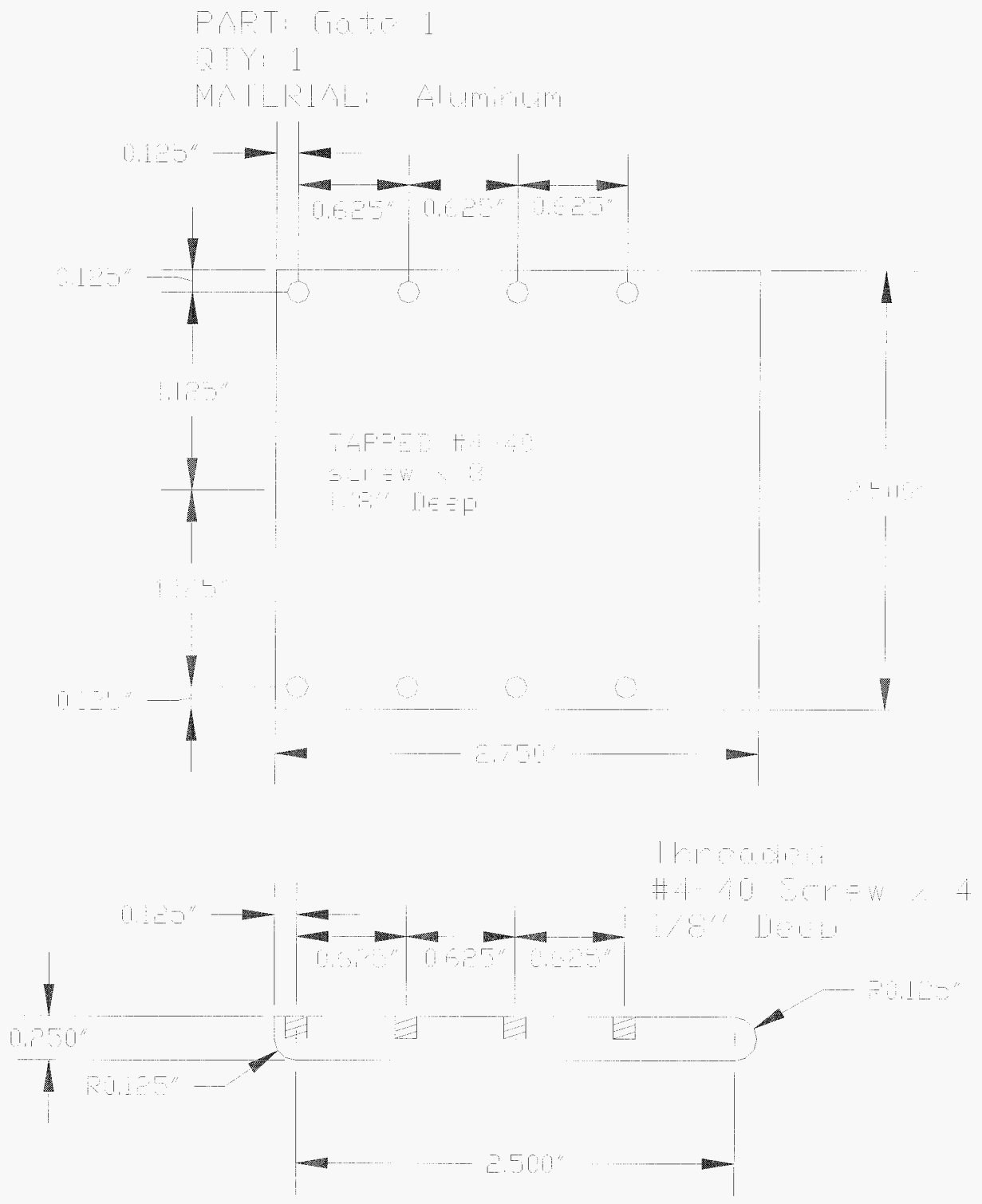

Figure 97. Sliding part of the gate with curved edge for Teflon sheet.

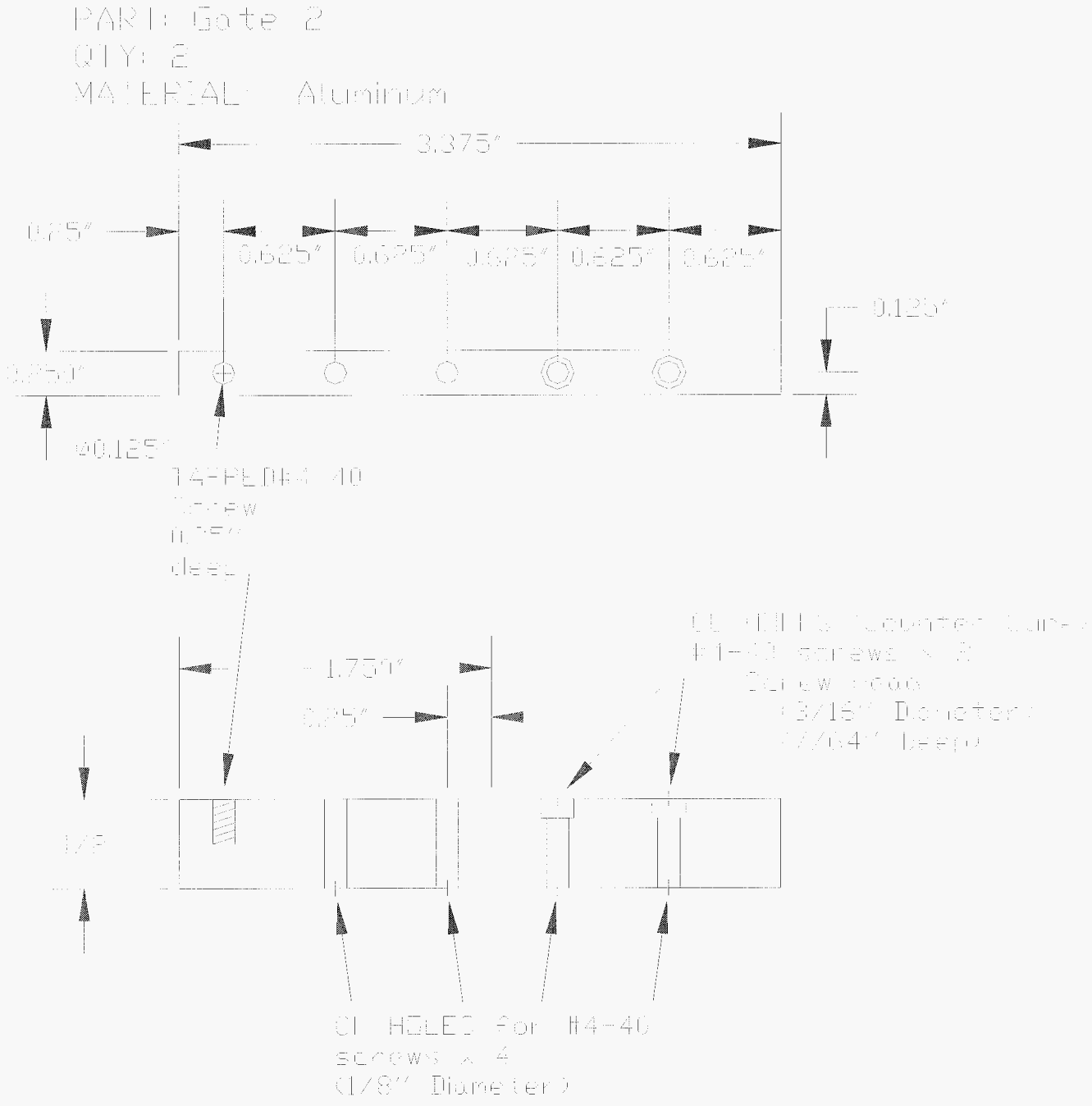

Figure 98. Mounting bracket for gate.

Nozzles

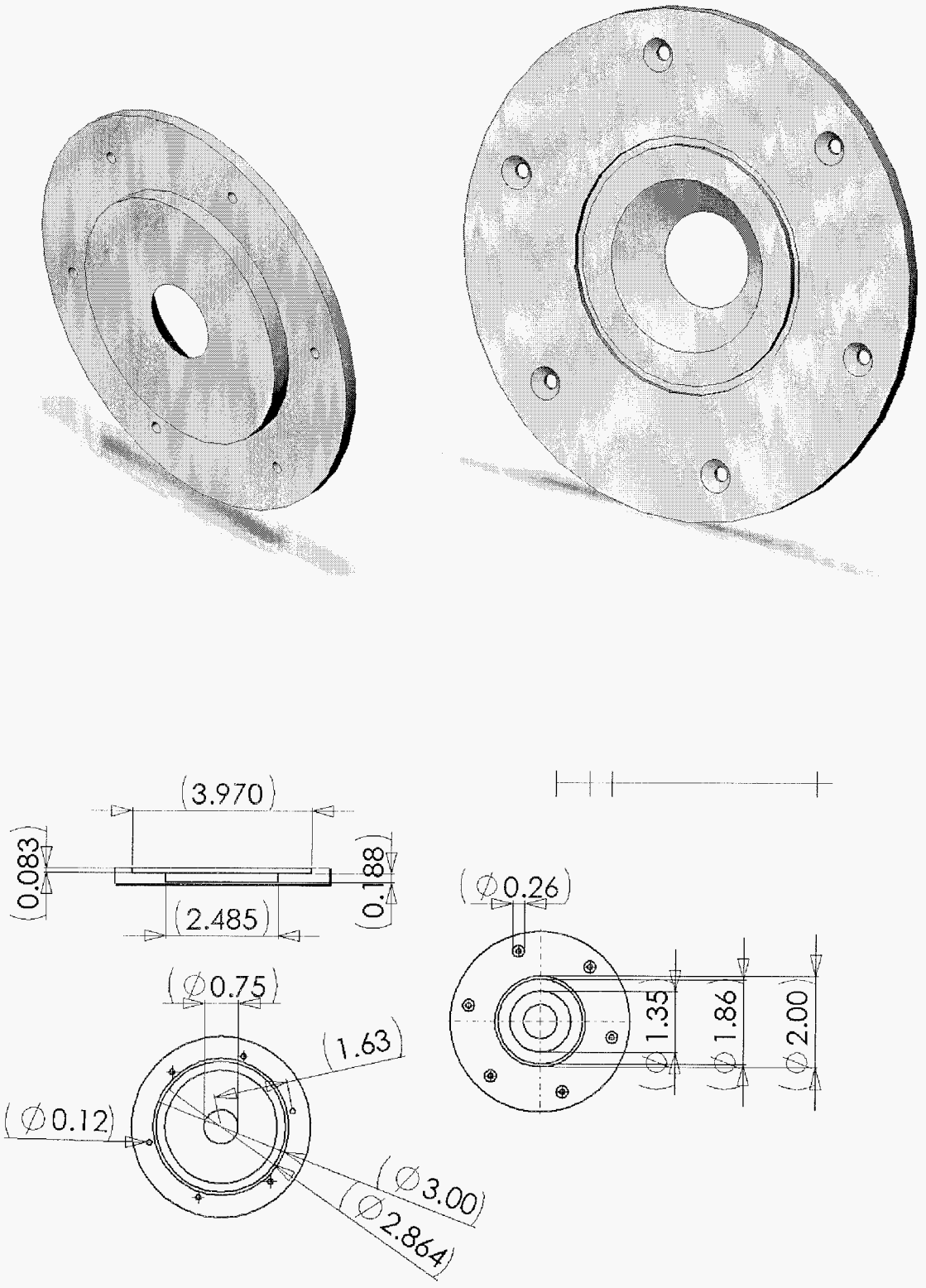

Figure 99. Example of circular nozzle

Motor, Chain, Sprocket

LEESON

DIMENSIONS

NEMA MOTORS

NEMA FRAMES, SCR RATED

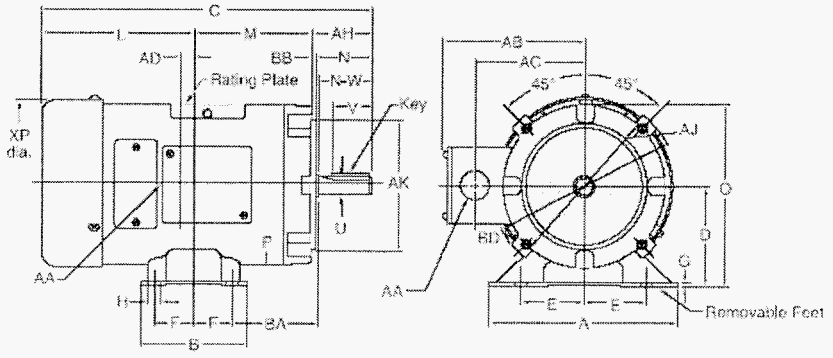

NEMA FRAMES (Inches)

NEMA Frame	Mounting Foot								Shaft			Mounting Face					General		
	2E	A	2F	B	BA	D	G	H	U	AH	V	AK	AJ	BD	TAP	BB	P	O	AA
42	3.5	4.75	1.69	2.45	2.06	2.625	.12	.38	.375	1.313	1.0	3.0	3.75	4.875	¼-20	.125	4.875	5.06	3.75
48	4.25	5.75	2.75	3.5	2.5	3.0	.12	.34	.50	1.69	1.375	3.0	3.75	5.00	¼-20	.125	5.59	5.81	.50
SS56	4.875	6.5	3.0	4.0	2.75	3.5	.12	.34	.625	2.06	1.41	4.5	5.875	6.50	⅜-16	.125	4.875	5.06	.50
S56	4.875	6.5	3.0	4.0	2.75	3.5	.12	.34	.625	2.06	1.41	4.5	5.875	6.50	⅜-16	.125	5.59	6.31	.50
56	4.875	6.5	3.0	4.0	2.75	3.5	.12	.34	.625	2.06	1.41	4.5	5.875	6.52	⅜-16	.125	6.52	7.75	.50
143T	5.5	6.5	4.0	6.5	2.25*	3.5	.12	.34	.875	2.125	1.41	4.5	5.875	6.52	⅜-16	.125	6.52	7.75	.75
145T	5.5	6.5	4.0	6.5	2.25*	3.5	.12	.34	.875	2.125	1.41	4.5	5.875	6.52	⅜-16	.125	6.52	7.75	.75
182/145TC	7.5	8.5	4.5	5.5	3.5	4.5	.13	.41	.875	2.125	1.41	4.5	5.875	6.52	⅜-16	.125	6.52	7.75	1.13

*143-5TC NEMA C Face BA dimension is 2.75".
For C dimension, see motor selection charts.

Figure 100. Drawing and Table from http://www.leeson.com

NEMA FRAME MOTORS • SCR RATED

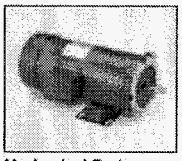

General Specifications:

High voltage permanent magnet DC motors are typically used with an SCR (thyristor) controller in applications requiring adjustable speed and constant torque throughout the speed range. They are also widely used in applications requiring dynamic braking or adjustable speed/ reversing capabilities.

Mechanical Features:

Low profile space-saving design. Unique brush holder design provides easy access to brushes and integral constant pressure brush/spring assembly for servicing. Large over-sized brushes assure longer brush life. Heavy-duty, stamped steel, bolt-on base (removable). NEMA C face mounting at no additional cost. Rugged die cast aluminum endshields with cast iron bearing inserts. Permanently lubricated sealed ball bearings. May be converted NEMA 48 base and/or C face using modification kits noted below.

Electrical Features:

Input power of 115 or 230 volts rectified AC when used with an appropriate SCR control. Linear speed/torque characteristics over entire speed range. High starting torque for heavy load applications. Capable of dynamic braking for faster stops. Reversible rotation with simple two-lead connection.

PWM RATED PM DC MOTORS

The DC motors listed above have been designed for use on unfiltered SCR (Thyristor) type rectified AC input. These motors may also be used with PWM (pulse width modulated) type DC adjustable speed drives at a higher HP rating.

TEFC • SCR RATED 90 & 180 VOLTS NEMA 56C • C FACE WITH REMOVABLE BASE[9]

HP	Full Load RPM	NEMA Frame	Catalog Number	App. Wgt. (lbs.)	Arm. Volts DC	Control Volts AC Input	F.L. Amps DC	"C" Dim. (Inches)
1/4	1750	S56C	098002	19	90	115	2.5	10.81
	1750	S56C	098003	22	180	230	1.4	11.31
1/3	1750	S56C	098004	23	90	115	3.5	11.31
	1750	S56C	098005	23	180	230	1.7	11.31
1/2	2500	S56C	098006	22	90	115	5.0	10.81
	2500	S56C	098007	22	180	230	2.5	10.81
	1750	S56C	098000	26	90	115	5.0	11.81
	1750	S56C	108014	29	90	115	5.0	12.81
	1750	S56C	098008	25	180	230	2.5	11.81
	1750	S56C	108015	30	180	230	2.5	12.81
3/4	2500	S56C	098009	26	90	115	7.6	11.81
	2500	S56C	108016	29	90	115	7.6	12.81
	2500	S56C	098010	25	180	230	3.8	11.81
	2500	S56C	108017	29	180	230	3.8	12.81
	1750	S56C	098032	36	90	115	7.3	13.81
	1750	S56C	108018	38	90	115	7.6	13.81
	1750	S56C	098069	36	180	230	3.8	13.81
	1750	S56C	108019	35	180	230	3.8	13.81
1	2500	S56C	108020	34	90	115	10.0	13.81
	2500	S56C	108021	36	180	230	5.0	13.81
	1750	S56C	108022	47	90	115	10.0	16.31
	1750	S56C	108023	39	180	230	5.0	14.81
1½	2500	S56C	108265	43	180	230	7.5	14.81
	1750	S56C	108092	53	180	230	7.6	16.88
	1750	S56/ 145TC	108262■	54	180	230	7.6	17.38
	1750	145TC	128000	70	180	230	7.5	18.34
2	2500	S56/ 145TC	108266■	51	180	230	8.6	16.88
	1750	145TC	128010	83	180	230	9.5	19.34
	1750	182/145TC	128001◀	84	180	230	9.5	19.34
3	1750	182/145TC	108502◀	88	180	230	14.0	21.75

TEFC • SCR RATED 90 & 180 VOLTS NEMA 56C • C FACE WITH REMOVABLE BASE[9]

HP	Full Load RPM	NEMA Frame	Catalog Number	App. Wgt. (lbs.)	Arm. Volts DC	Control Volts AC Input	F.L. Amps DC	"C" Dim. (Inches)
3	1750	182/145TC	108502◀	88	180	230	14.0	21.75

Figure 101. Information and schematics from http://www.leeson.com

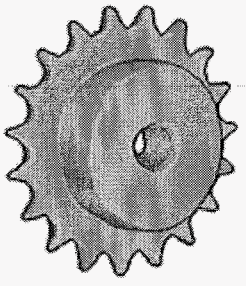

More About Steel Plain-Bore Roller Chain Sprockets

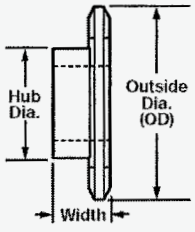

No. of Teeth	For #25 Chain (¼" Pitch)				For #35 Chain (⅜" Pitch)				For #40 Chain (½" Pitch)				For #50 Chain (⅝" Pitch)			
	OD	Width	Hub Dia.		OD	Width	Hub Dia.		OD	Width	Hub Dia.		OD	Width	Hub Dia.	
21	1.81"	⅝"	1⅜"	6793K14	2.71"	⅞"	2"	6793K129	3.62"	1"	2¾"	6793K153	4.52"	1"	3"	6793K176
30	2.53"	⅝"	1½"	6793K19	3.79"	⅞"	2"	6793K135	5.06"	1"	3¼"	6793K158	6.32"	1¼"	3¼"	6793K182

Figure 102. Chain Drawings and table from http://www.mcmaster.com

Roller Chain Tensioners

Automatic Spring Roller Chain Tensioners

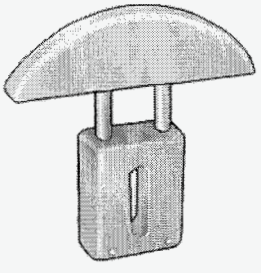

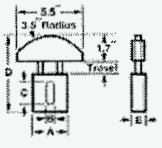

Built-in springs put constant tension on single-strand roller chain. They absorb and buffer momentary overloads, reduce vibration, and improve drive performance. Mount them vertically or horizontally and adjust with a single bolt (not included; use 3/8" bolt for 6233K33 and K34, 7/16" bolt for K35 and K36, and 1/2" bolt for K37 and K38).

The reciprocating steel shafts are attached to a self-lubricating UHMW polyethylene arc for smooth, quiet operation. Case is die cast aluminum; bearings are sintered bronze. Maximum operating temperature is 180° F.

For ANSI Chain No.	Tension, lbs.	Travel	(A)	(B)	(C)	(D)	Proj. (E)		Each
50	20-60	1.25"	2.95"	0.49"	2.36"	6.48"	1.18"	6233K35	64.80

Figure 103. Roller chain tensioner drawing and table from http://www.mcmaster.com

Model Number	Holding Torque 2 phases on (oz.in.) Unipolar	Holding Torque 2 phases on (oz.in.) Bipolar	Voltage per Phase (V/phase) Un-polar	Current per Phase (A/phase) Unipolar	Current per Phase (A/phase) Bipolar	Resistance per Phase (ohms/phase) Unipolar	Inductance per Phase (mH/phase) Unipolar	Nominal Rotor Inertia (oz.in.sec^2)	Shaft Diameter (in.)	Maximun Motor Length (in.)
34K112_-LW8	590	830	2.2	6.1	4.3	0.36	2.40	.02	.500	3.13

Stepper Motors

Note: LW8 = Lead Wire

For seventh digit, choose S or D: S = Single Shaft, D = Double Shaft

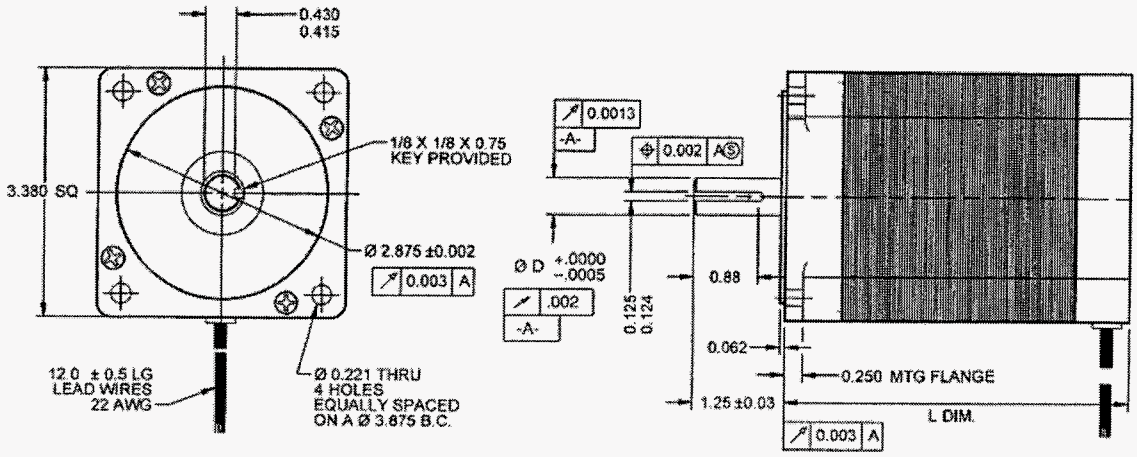

Connection	Lead Name	Lead Color	Terminal #
4 Lead Bipolar Series	A	Black (BLK)	1
	A	Orange (ORG)	3
	B	Red	2
	B	Yellow (YEL)	4
	None	WHT/BLK & WHT/ORG	6 & 5
	None	WHT/RED & WHT/YEL	8 & 7
4 Lead Bipolar Parallel	A	BLK & WHT/ORG	1 & 5
	A	ORG & WHT/BLK	3 & 6
	B	RED & WHT/YEL	2 & 7
	B	YEL & WHT/RED	4 & 8
6 Lead Unipolar	Phase 1	Black (BLK)	1
	Phase 3	Orange (ORG)	3
	Phase 2	Red	2
	Phase 4	Yellow (YEL)	4
	Common 1 & 3	WHT/BLK & WHT/ORG	6 & 5
	Common 2 & 4	WHT/RED & WHT/YEL	8 & 7
Ground		Green/Yellow	Motor Frame

Figure 104. Stepper motor drawing and table from http://www.anaheimautomation.com

Connector Blocks

BNC-2100 Series Connector Blocks (See Figure 3)

The BNC-2100 Series are shielded connector blocks with signal-labeled BNC connectors for easy connectivity of your analog input, analog output, digital I/O and counter/timer signals to your multifunction DAQ device, including analog output devices. The BNC-2110 and BNC-2120 work with all E Series and Basic multifunction DAQ devices. The BNC-2120 also provides a function generator, quadrature encoder, temperature reference, thermocouple connector, and LED so that you can test the functionality of your hardware. The BNC-2115 has 24 BNC inputs for connecting to the extended I/O channels of our 100-pin E Series DAQ devices.

BNC-2110 777643-01

Dimensions – 20.3 by 11.2 by 5.5 cm (8.0 by 4.4 by 2.2 in.)

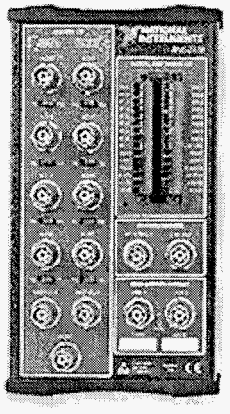

Figure 105. Connector block picture and information from http://www.anaheimautomation.com/

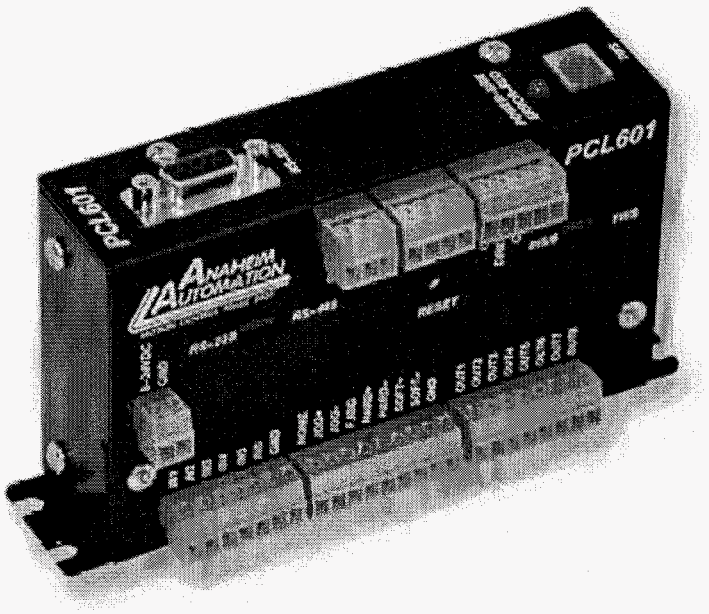
PCL601
ANAHEIM AUTOMATION
RESET

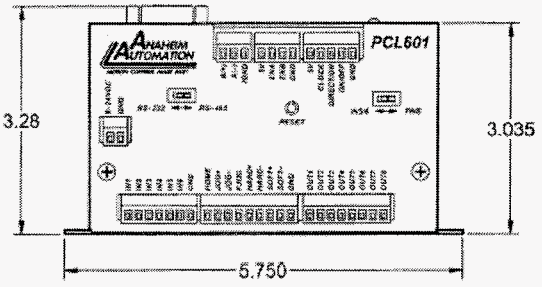
PCL601
ANAHEIM AUTOMATION
RESET
3.28
3.035
5.750

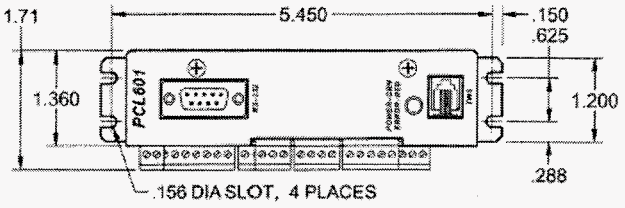
1.71
5.450
.150
.625
1.360
PCL601
1.200
.288
.156 DIA SLOT, 4 PLACES

Specifications

Power Requirements:	8-24VDC, 50/60Hz (0.5W Peak Power)
Nonvolatile Memory:	2KB of stored programming space
Baud Rate:	38,400 Baud, Fixed
Data Format:	Half duplex, 1 start bit, 8 data bits, no parity, 1 stop bit
Communication Protocol:	RS232 or RS485 selectable
Encoder Feedback:	Quadrature, CHA, CHB, 5VDC Signal Compatibility
Controller Outputs:	8 Programmable Outputs, Open Drain Type, 40V, 100mA, +5VDC Output, 50mA
Controller Inputs:	6 Programmable Inputs Logic 0: 0 - 0.8VDC Logic 1: 3.5 - 24VDC Analog Input: 0 - 5VDC
Pulse Output Range:	1 - 50KHz, 10µs Negative Going Pulse Width

Figure 106. Drawing and information from http://www.anaheimautomation.com

Yag Laser

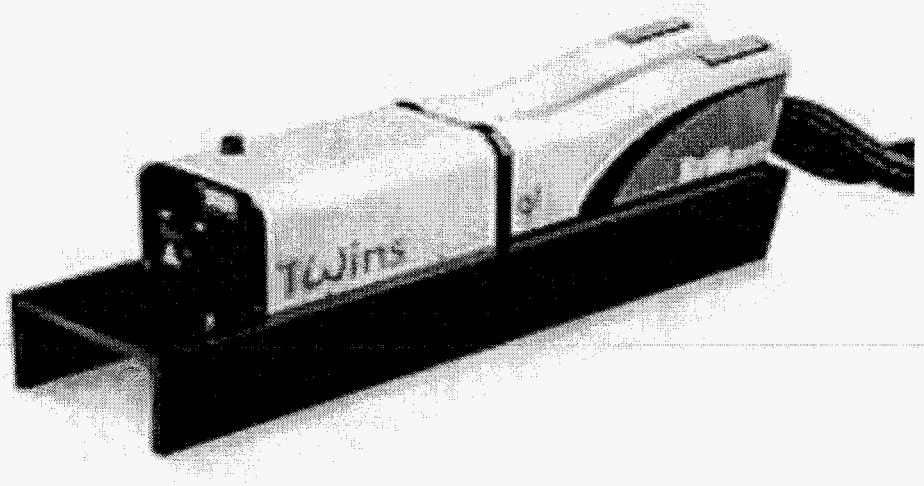

Specifications at 532 nm	TWINS
Pulse Rep. Rate (Hz)	10
Energy / pulse (mJ)	150
Pulse duration (ns)	4
Energy stability (%)	+/-5
Beam diameter (mm)	6
Pointing stability (microrad)	<50
Jitter, (+/- ns WRT Q-switch)	+/-0.5
Divergence (mrad)	<0.5

Figure 107. Laser information from http://www.quantel.fr/uk/presentation_euro.htm